



TECHNISCHE
UNIVERSITÄT
WIEN

DIPLOMARBEIT

Faltbare Tragstrukturen – Räumliche Scherengitter für mobile und wiederverwendbare Anwendungen in der Architektur

ausgeführt zum Zwecke der Erlangung des akademischen Grades eines Diplom-Ingenieurs unter der Leitung

Univ.Prof. Dipl.-Ing. Peter Bauer

E259-02 Forschungsbereich Tragwerksplanung und Ingenieurholzbau

eingereicht an der Technischen Universität Wien

Fakultät für Architektur und Raumplanung

von

Ljubov Ilieva B.Sc.

0725859

Wien, am

ZUSAMMENFASSUNG

Auf dem Gebiet der kinetischen Architektur zeichnen sich faltbare Konstruktionen durch ihre Fähigkeit aus, eine starke Veränderung der Form und Größe auf autonome Weise vollziehen zu können. In der Regel expandiert eine solche Struktur von einem komprimierten, geschlossenen Zustand in einen weit größeren, entfalteten oder geöffneten Zustand.

Solche Strukturen können aus faltbaren Gittern oder Platten, gespannten Membranen oder Zugseilen und Druckstreben bestehen. Auch Kombinationen der genannten Konstruktionen sind möglich. Der Fokus dieser Diplomarbeit liegt auf der Unterkategorie faltbarer, räumlicher Tragwerke, bestehend aus geraden Stäben welche gelenkig verbunden sind - sogenannte Scherengitter. Ihre Eigenschaften in Bezug auf die Faktoren Materialeffizienz, Ausdehnungs-Verhältnis, Zuverlässigkeit und Dauerhaftigkeit der Mechanik, lassen ein hohes Potential für den Einsatz im Bereich mobiler, wiederverwendbarer, temporärer oder beweglicher Konstruktionen vermuten. Bisher ist die Umsetzung solcher Konstruktionen in der Architektur jedoch begrenzt. Ein Grund dafür ist der hohe Anspruch in Bezug auf die Gestaltung einer kompatiblen Gittergeometrie, insbesondere bei komplexen räumlichen Konfigurationen und unter Berücksichtigung der Limitationen aufgrund von Transportgrößen. Mithilfe parametrischer Modelle entwickelt diese Diplomarbeit eine Entwurfsstrategie für weitgespannte, faltbare Scherengitter auf Oberflächen mit doppelter Krümmung, einschließlich interaktiver Überwachung des Faltvorgangs, sowie der mechanischen Beanspruchung und des Tragverhaltens.

Im ersten Teil dieser Arbeit werden die geometrischen Rahmenbedingungen der Faltbarkeit von Scherengittern sowie deren technische Umsetzung, zusammengefasst und erläutert. Diese Prinzipien werden an einer Reihe digitaler Modelle erprobt. Drei Gitterkonfigurationen werden ausgewählt und als Fallstudien herangezogen, wobei das Tragverhalten analysiert, die Querschnitte optimiert und der Faltvorgang simuliert wird. Die Ergebnisse werden im Detail besprochen. Das letzte Kapitel widmet sich einer Strategie für die Fertigung, die Montage und die Installation solcher Scherengitter. Ein rationalisierter Knotenverbinder wird entwickelt und ein integriertes Antriebssystem zur Steuerung des Faltvorgangs wird vorgeschlagen. Neben den digitalen Modellen werden mehrere funktionsfähige Prototypen gebaut und dokumentiert.

ABSTRACT

In the field of kinetic architecture, deployable structures are characterized by their capacity to execute large configuration changes in an autonomous way. Typically, the configuration transforms from a compact or closed retracted state to a much larger, opened deployed state.

Deployable structures can include expandable grids, foldable plates, tensioned membranes, strut-cable systems, or a combination of the above. This thesis focuses on the sub-category of double-layer scissor grids, consisting of straight bars, linked with articulated joints. Their performance in regard to material efficiency, volume expansion ratio, mechanical reliability, and durability indicates a high potential for use in the field of mobile, reusable, temporary, and transformable structures. However, their application in architecture has so far been limited. A reason for this can be found in the complexity of design, particularly when dealing with complex spatial configurations and limitations in transport size.

Utilizing parametric modeling environments, this thesis develops a strategy for designing wide-span deployable scissor grids on surfaces with double curvature with an interactive evaluation of deployment and structural performance. This strategy is applied to several case studies and the results are discussed.

The underlying geometric conditions for deployability and their technical implementation are summarized and illustrated in the first part of this thesis. These principles are illustrated in a number of digital models. A selection of three grid configurations is modeled in detail and presented as case studies, where the structural performance is reviewed and the deployment process is simulated and discussed in detail. The final chapter proposes a strategy for fabrication, assembly, and installation. A rationalized node connector is developed in detail and a structurally integrated drive system is proposed for controlling the deployment process. Apart from digital models, several functioning prototypes are built.



Die approbierte gedruckte Originalversion dieser Diplomarbeit ist an der TU Wien Bibliothek verfügbar
The approved original version of this thesis is available in print at TU Wien Bibliothek.

DEPLOYABLE STRUCTURES

Spatial scissor grids for mobile and reusable applications in architecture

CONTENTS

1.	INTRODUCTION	9
1.1.	Deployable Structures	9
1.2.	Aim and scope of research	13
1.3.	Thesis outline	13
2.	STATE OF THE ART	15
2.1.	Introduction	15
2.2.	Terminology	16
2.3.	Classification	16
2.3.1.	Translational units	17
2.3.2.	Polar units	18
2.3.3.	Scissor grid geometry and kinematics	19
2.3.4.	Angulated units	20
2.3.5.	Discussion	21
2.4.	Structures based on polar and translational units	21
2.5.	Discussion	26
3.	DESIGN METHODS	27
3.1.	Introduction	27
3.2.	Digital tools	27
3.2.1.	Grasshopper	27
3.2.2.	Particle spring systems	28
3.2.3.	Finite element method	28
3.3.	A design method based on circle packing	28
3.3.1.	Planar grids	29
3.3.2.	Spherical grids	30
3.3.3.	Other grids	31
3.4.	Modelling and Simulation	31
3.4.1.	Modeling prismatic modules by mesh face	31
3.4.2.	Modeling linkages as a UV network	32
3.4.3.	Deployment simulation with Kangaroo2	33
3.4.4.	Discussion	35

3.5.	Digital experiments	36
3.5.1.	Spherical domes	36
3.5.2.	Rotational and Translational surfaces	40
3.5.3.	Other surfaces	42
3.6.	Discussion	44
4.	RESULTS	45
4.1.	Introduction	45
4.2.	Structural analysis and deployment simulation	46
4.2.1.	Material	46
4.2.2.	Load Cases	46
4.2.3.	Optimization	47
4.2.4.	Documentation of results	47
4.3.	Cross-vault 20-12	48
4.3.1.	Base grid configuration	48
4.3.2.	Load cases	49
4.3.3.	Cross-section dimensions and optimization	50
4.3.4.	Deployment simulation	58
4.3.5.	Discussion	59
4.4.	Cross-vault 14-11	60
4.4.1.	Base grid geometry	60
4.4.2.	Load cases	61
4.4.3.	Cross-section dimensions and optimization	62
4.4.4.	Deployment simulation	70
4.4.5.	Discussion	71
4.5.	Barrel vault 12-10	72
4.5.1.	Base grid geometry	72
4.5.2.	Load cases	73
4.5.3.	Cross-section dimensions and optimization	74
4.5.4.	Deployment simulation	82
4.5.5.	Discussion	83
4.6.	Discussion	84

5.	DETAIL DESIGN AND PROTOTYPING	85
5.1.	Introduction	85
5.2.	Proof of concept	86
5.3.	Node connectors and vertical bracing rods	94
5.3.1.	Bracing node prototype	94
5.3.2.	Design challenges	96
5.3.3.	Assembly using rationalized node connectors	97
5.4.	Node connector - Design A	98
5.4.1.	Vertical bracing members with a linear drive	104
5.5.	Node connector - Design B	106
5.5.1.	Vertical bracing members with telescopic actuator	106
5.6.	Visualization	112
6.	CONCLUSION	115
7.	BIBLIOGRAPHY	117
8.	FIGURES	119
9.	TABLES	125

1. INTRODUCTION

1.1. Deployable Structures

In the field of kinetic or transformable architecture, deployable structures are characterized by their capability to execute large configuration changes in an autonomous way. Typically, the configuration transforms from a compact or closed retracted state to a much larger, opened, or deployed state (Jensen, 2004). Deployable structures are usually employed due to requirements such as ease of storage and transportation, as well as rapid dispatch and installation. The deployment process and underlying mechanism should be reliable and perform without damage and in a safe manner (Pellegrino, 2001).

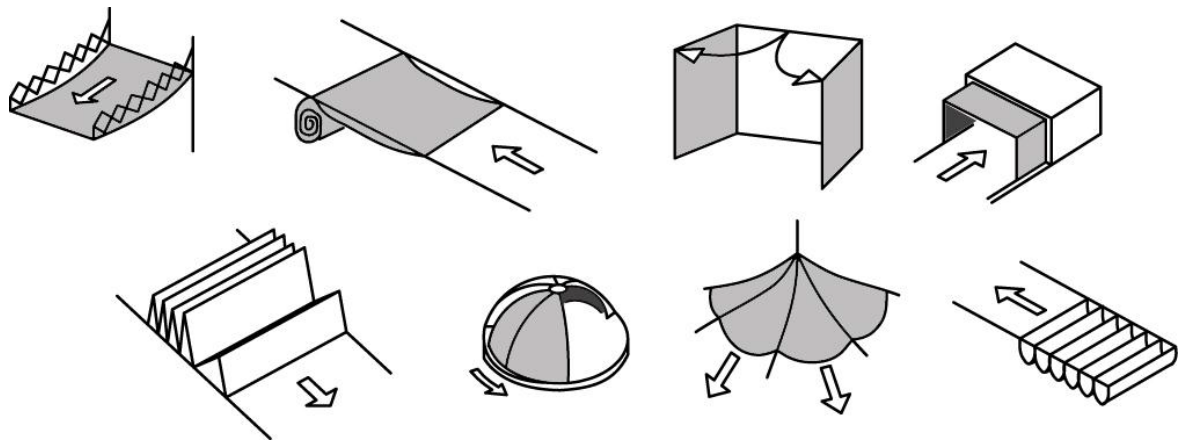


Figure 1: Examples of deployable structures (Zuk & Clark, 1970)

The principle of transformable structures has been applied widely throughout history. Examples of this range from everyday objects such as the folding chair or the umbrella to architectural applications for temporary building structures, such as the velum of the Roman Coliseum, or nomadic tents, like the Mongolian yurt (De Temmerman, 2007).

In the context of academic research, the subject is relatively young. A surge of scientific interest during the 1950s and 60s was set in motion by the early era of space exploration. Due to the storage limitations of launch vehicles, deployable structures are widely used in space technology until today. At present, the two main application areas of deployable structures are Aerospace and Architecture (Jensen, 2004).

Applications in architecture range from fixed-location retractable roofs to temporary buildings for recreational use to mobile units for remote locations or emergency situations. To establish a framework for this thesis, deployable structures for temporary and reusable building applications will be evaluated closer.

In literature, such applications are described under the term mobile shelter systems. For this type of building construction, there is a vast range and diversity of forms and structural solutions. They are designed to provide a weather-protected enclosure for a wide range of activities. Enclosure requirements are generally very simple, with the majority needing only a weather-protecting membrane supported by some form of erectable structure. In all applications, both the envelope and the structure need to be capable of being easily moved in the course of normal use, which very often requires the building system to be assembled at high speed or on unprepared sites (Gengnagel & Burford, 2006).

In the context of mobile shelter systems, deployable structures offer benefits regarding ease and speed of erection. When designed as a lightweight construction with a reliable deployment mechanism they can mitigate transport size limitations and carry a high potential for reusability in architecture.

A classification of deployable structures by Hanaor and Levy (2001), referenced frequently in literature, makes a two-way distinction between morphological and kinematic characteristics (Fig. 2). Morphological subgroups are lattice and continuous structures, while kinematic subgroups range from rigid links to deformable systems.

It is noted that structural systems and building forms applicable to deployable structures differ from their conventional, non-transformable, and immobile counterparts only in their kinetic behavior. The mechanism which is necessary for deployment must not compromise the stability and rigidity of the final form. This factor is associated with a higher degree of mechanical and structural complexity, which generally entails higher design and production costs. Focusing on the factors of mobility and reusability as well as a structure's applicability to a wide range of geometric forms and site conditions can be a method to compensate for the increase in investment.

For this master thesis, the focus of research will lie in the area of lattice structures with rigid links (marked red in Fig. 2). Double-layer grids will be studied in detail. Such expandable lattice structures apply the principle of a scissor hinge for deployment – consisting of rigid bars, linked with articulated joints, they have the ability to fold into a compact bundle when

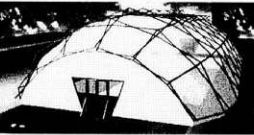
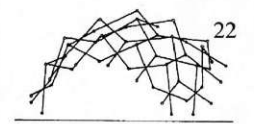

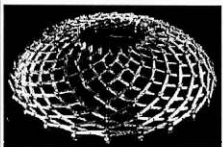
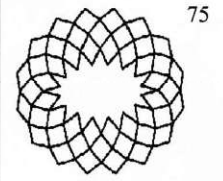
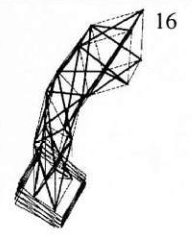

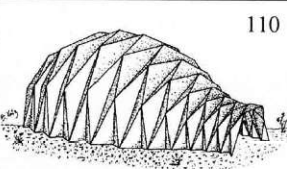
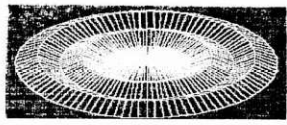
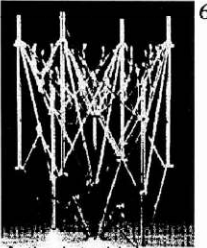

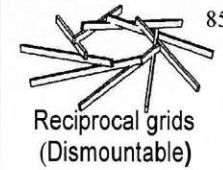
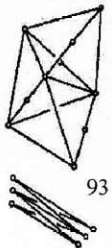
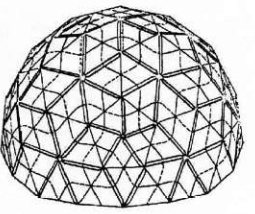

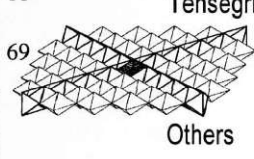
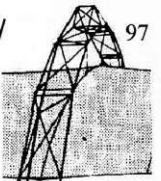
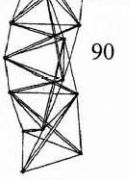

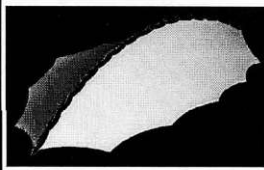


		Morphology			
		Lattice			Continuous
Kinematics	Rigid links	DLG	SLG	Spine	Plates
		Pantographic (scissors)			Folded Plates
		 19  22  55	 74  75	 16  98	 110  5
		Bars			Curved surface
		 60	 83  85	 93  101	
Deformable	Strut-cable systems		Tensioned membrane		
	 68  69  97	 90	 120  88	 124 	
			Fabric	Pneumatic	

Figure 2: Classification of structural systems for deployable structures by their morphological and kinetic characteristics As in Hanaor & Levy (2001).

following geometric constraints in designing them. Because of their high degree of material efficiency, volume-expansion ratio, and reliability of deployment (Tab. 1), scissor structures offer great suitability in the field of mobile architecture.

CRITERION	EVALUATION
Architectural flexibility	Flexible modular design is readily applicable. Large areas can be covered with relatively small modules connected on site.
Component uniformity	High component uniformity can be maintained, although doubly curved surfaces may require some variation in unit cell dimension
Compactness	The structure folds to a compact bunch of bars. Compatible folding of the membrane covering needs to be considered
Structural efficiency	Structural efficiency is medium to low, depending on the surface geometry, constituent units and bracing.
Maintenance	Repeated deployment may cause significant wear and tear to the membrane and to connections.
Site preparation	Generally, self-supporting configurations can be designed, requiring minimal foundation and site preparation.
Connections/assembly	Degree of deployability is relatively high. Site connections involve connection of deployable modules and addition of racing elements.
Reliability	Medium mechanical complexity. Articulated joints and hinges are relatively simple. Human assistance in deployment is usually required.
Auxiliary equipment	No auxiliary equipment is required other than relatively light lifting equipment to assist in deployment and folding.

Table 1: Evaluation of double-layer scissor grids as in Hanaor&Levy 2001.

Many impressive architectural applications for these mechanisms have been proposed, but due to their geometric and mechanical complexity few have been constructed at full-scale (Asefi & Kronenburg, 2006). These are usually retractable roofs or canopies with a fixed location, in form of flat, spherical, cylindrical, or radial grids. In the field of mobile architecture, the limitations regarding transport size represent a further challenge to versatility in form and dimension, when dealing with more complex configurations. Parametric design tools and computational models for interactive simulation and structural analysis are valuable tools when managing above mentioned restrictions.

1.2. Aim and scope of research

A reason for the limited use of deployable scissor grids for mobile and temporary architectural applications may be found in the complexity of design and construction in compatibility with deployment constraints and transport restrictions, regarding size and weight. Parametric modeling environments, which are widely used in architectural design today, offer powerful tools to handle this degree of complexity efficiently.

This master thesis aims to develop a strategy for designing wide-span deployable scissor grids on surfaces with double curvature with an interactive evaluation of transport size when retracted and structural performance when deployed.

With this intent a form-finding method is developed, to produce geometrically compatible deployable scissor grids with various shapes and grid configurations. An evaluation is then performed by simulating the deployment process with the live physics engine Kangaroo2, while the structural analysis, using a finite element model in Karamba3d, is determining the member dimensions. This setup is applied to several case studies. It further facilitates the fabrication and assembly of multiple functioning prototypes by means of 3d printing and CNC milling.

Insights gained from the design and assembly of the physical prototypes then inform the design of the mechanical components facilitating deployment, such as hinges and node connectors. Explicit attention is paid to rationalization regarding the fabrication and assembly of these building parts. In addition, a structurally integrated drive system is proposed for controlling the deployment process.

1.3. Thesis outline

With these intentions in mind, the next chapter provides a detailed review of different typologies and configurations for deployable scissor grids. After explaining common terminology and classification, the geometric constraints and construction methods are illustrated. Prominent researchers in the field are presented, along with their proposals for deployable scissor grids.

Chapter 3 presents digital tools for construction, simulation, and structural analysis, then gives an overview of established design methods for geometrically compatible spatial scissor grids, along with their implementation within a parametric design environment. These methods are then applied to several grid configurations to provide insight into the variety of suitable shapes and their kinematic behavior, by simulation of their deployment process. As a result of these digital experiments, a form-finding method for designing geometrically compatible deployable scissor grids on a variety of surfaces is developed.

In Chapter 4, two typologies of wide-span deployable grids are generated using the aforementioned form-finding method. Using these typologies three configurations are modeled in detail to be used as case studies for structural analysis and optimization. These detailed digital models, fulfilling structural and kinematic requirements, are then subjected to a simulation of the deployment process, providing information on the deployment behavior, volume expansion ratio, and transport size of a given structure.

Following the design, simulation, and analysis of digital models, the principles are tested on physical prototypes, documented in chapter 5. Informed by the process of prototype production, this chapter focuses on strategies for the fabrication, assembly, and installation of such scissor grids. A rationalized node connector is designed in detail and a structurally integrated drive system for controlled deployment is proposed.

2. STATE OF THE ART

2.1. Introduction

The following chapter gives a brief overview of the terminology commonly used in literature, followed by a detailed review of existing systems for deployable scissor structures and their underlying principles.

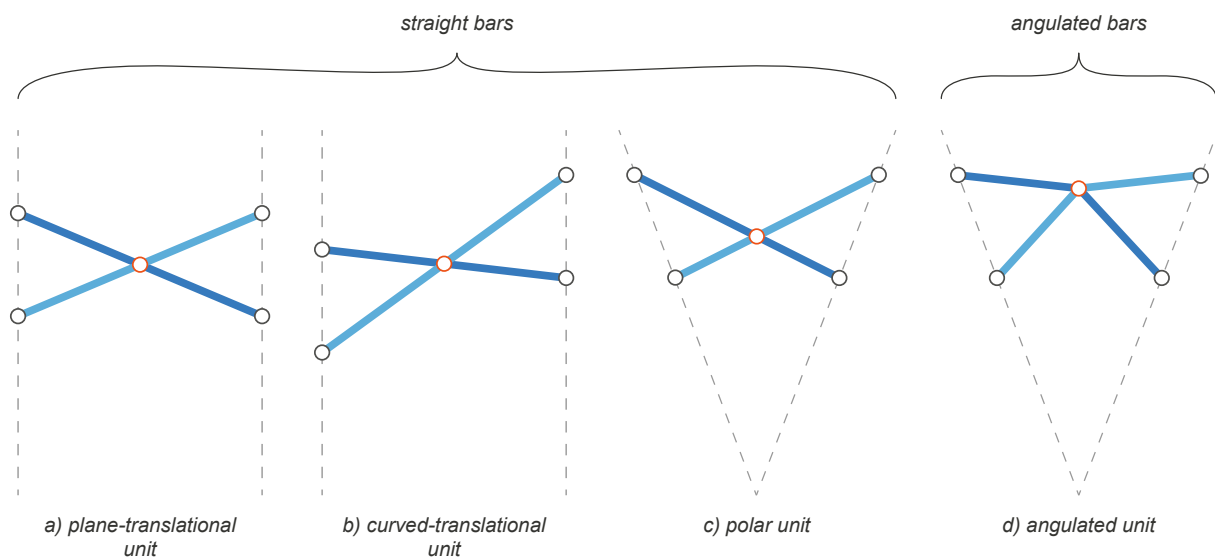


Figure 3: Most common types of scissor units consisting of straight or angulated bars.

Within the realm of expandable grids, there can be distinguished between structures consisting of either straight or angulated bars (Fig. 3). The former displays a higher volume-expansion ratio, which is why they are more frequently mentioned in the context of mobile applications and will be studied in greater detail on the following pages. Deployable structures consisting of straight bars can be configured to form translational or polar units. Different configurations along with the geometric constraints for deployment are reviewed and illustrated in detail. Before continuing to parametric design methods in the next chapter, some prominent proposals for large-scale deployable scissor structures are presented.

2.2. Terminology

A deployable scissor grid can be considered a kinematic linkage of multiple scissor units, also known as scissor-like elements or SLEs. A scissor unit (Fig. 4 a) consists of a pair of bars, connected at an intermediate hinge-point by a revolute joint, allowing a relative rotation of the bars around an axis normal to the unit plane (i.e. the plane containing the scissor bars). The distances between this intermediate hinge point and the endpoints of the bars are the semi-lengths of a scissor unit, while the imaginary lines connecting the upper and lower endpoints of the bars will be the unit lines (De Temmerman, 2007). The length measured between the upper and lower endpoints defines the structural thickness of a unit.

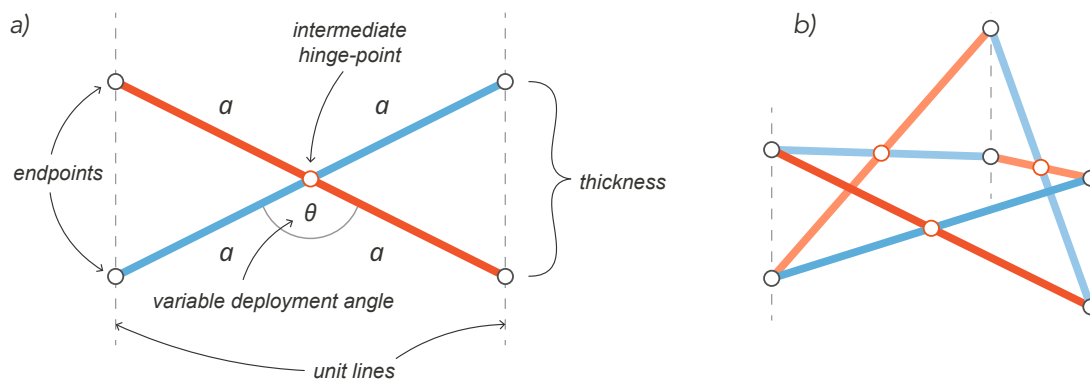


Figure 4: a) Composition of a scissor unit illustrated on a regular plane-translational unit. b) Triangular module, consisting of a linkage of three plane-translational units arranged to form a closed loop.

When interconnecting multiple units at their endpoints, scissor linkages are formed. Linkages arranged to form a triangular or quadrangular closed loop are called prismatic scissor modules (Fig. 4 b) and can be tessellated on a variety of different surfaces to form scissor grids (Roovers & De Temmerman, 2017).

2.3. Classification

To classify different types, literature makes a distinction between straight and angulated scissor units, based on the shape of the bars. Further differentiation of structures consisting of straight bars, identifies two sub-groups depending on the properties of the unit lines. Both the shape of the bars and the conditions of unit lines have a direct impact on the deployment behavior of a structure. The proportion of semi-lengths to each other further gives insight into the curvature of the linkage.

2.3.1. Translational units

The imagined lines connecting a scissor unit's upper and lower endpoints are called unit lines. With translational units, these lines are parallel and remain so during deployment. The most elementary configuration for a scissor unit occurs when designing flat grids with constant thickness. This is called a plane-translational unit (Fig. 5) and is formed by bars of equal length, hinged at their midpoint, thereby forming two identical isosceles triangles. Translational units can also be applied when designing grids on a wide variety of curved surfaces. Curved-translational units (Fig. 6) are formed by interconnecting bars of different lengths at their respective midpoints, forming a pair of congruent triangles. By varying the deployment

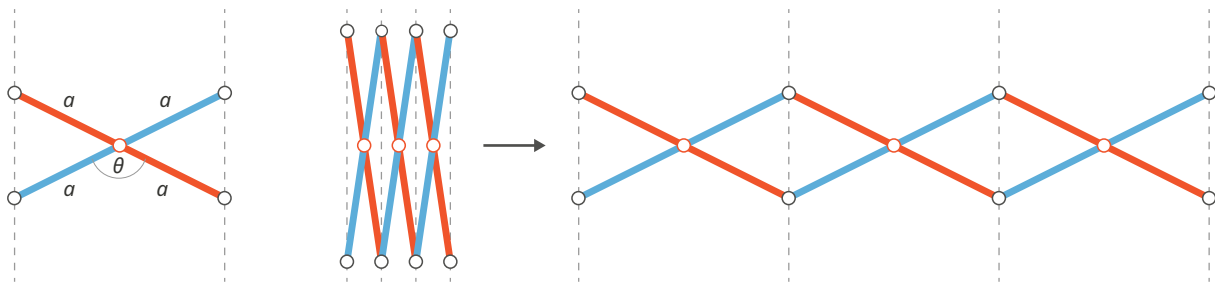


Figure 5: Linkage of three regular plane-translational units, shown in two stages of deployment.

angle θ , included between the two bars, the structure is transformed from a compact bundle to its final deployed state in a linear movement. In the case of translational grids, the direction of this linear movement remains constant during the deployment process, which makes the transformation between the two stages completely stress-free. Figures 6 show a linkage of curved-translational units in two stages of deployment.

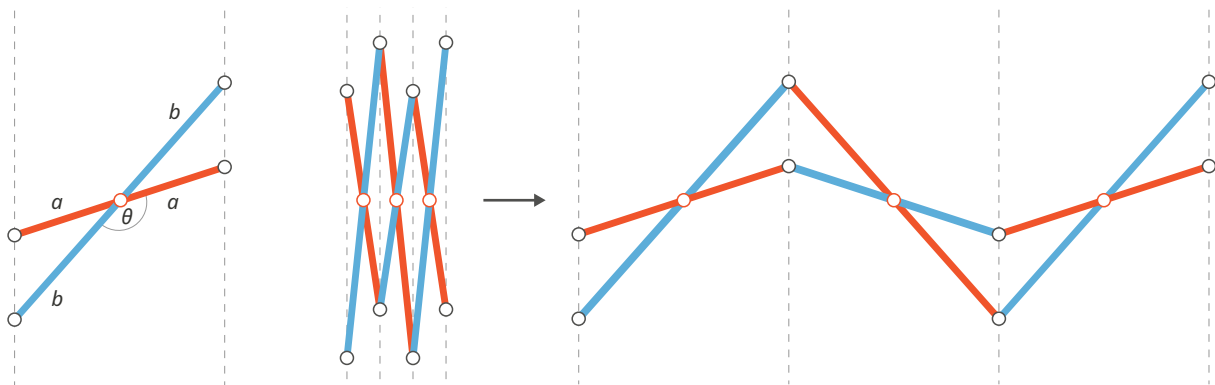


Figure 6: Linkage of three regular curved-translational units, shown in two stages of deployment.

2.3.2. Polar units

When the unit lines of a scissor unit are not parallel but intersect at a common point, they are called polar units. Polar units can be used to cover surfaces of constant curvature (e.g. spherical domes). The most common form displays constant thickness and is constructed by interconnecting to bars of equal length while moving the intermediate hinge-point away from the center (Fig. 7b). The resulting unit lines intersect at an angle γ , which varies during the linear deployment process. It is necessary for geometric compatibility during deployment, that all units have the intersection point in common (Roovers & De Temmerman, 2014). Figure 7 shows a linkage of polar units in two stages of deployment. By varying the deployment angle θ , included between the two bars, the structure is transformed from a compact bundle to its final deployed state. Similar to translational units the deployment process is linear. In contrast to translational units a grid composed of polar units can implement curvature with bars of the same length. However, only surfaces with single curvature and a high degree of symmetry can be covered this way (Roovers & De Temmerman, 2017).

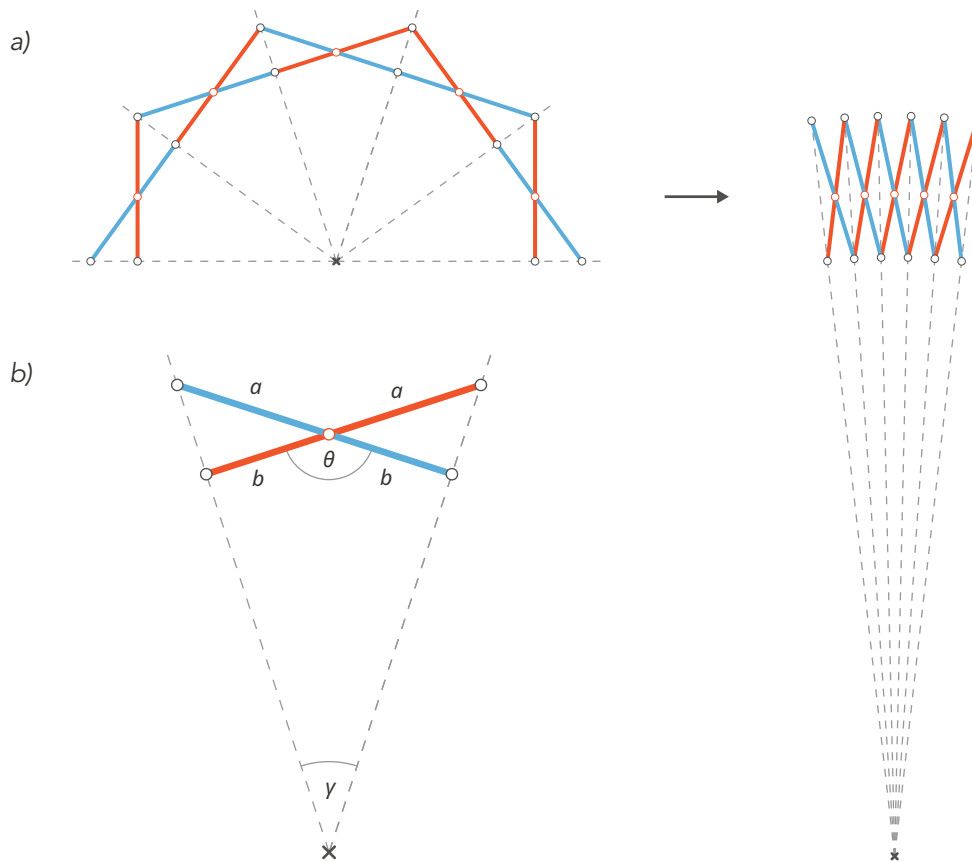


Figure 7: a) A linkage of polar units forming an arc is shown in two stages of deployment. b) Composition of a regular polar unit.

2.3.3. Scissor grid geometry and kinematics

Double-layer scissor grids (DLG) as described by Hanoar and Levy (2001) are constructed with units, which are positioned perpendicular on a base surface following a triangular or quadrangular tessellation pattern, forming prismatic modules (Fig. 4 b). This results in prismatic scissor modules, where the upper and lower endpoints describe two distinct grids. DLGs (Fig. 8 b) allow the largest variation in shape and possess better structural properties than single-layer grids (SLG) where the units are positioned in plane with the base surface (Fig. 8 a).

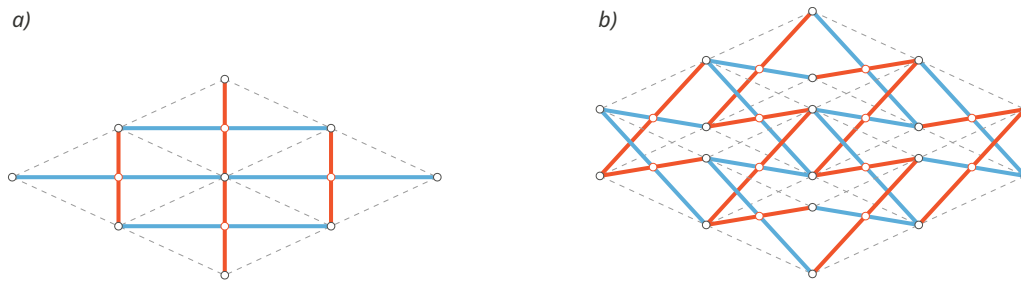


Figure 8: Illustration of a) single-layer and b) double-layer grid configuration.

For these grids to be deployable they have to follow certain geometrical constraints. Most crucial for designing scissor grids with straight bars is the deployability constraint described by Escrig (1985), stating the sum of the semi-lengths of a scissor unit has to equal the sum of the semi-lengths of the adjoining unit. It is expressed in the following Formula:

$$k'_1 + l'_1 = k_1 + l_1$$

This is to ensure that a linkage of multiple units can be contacted into its most compact state where all bars are aligned and theoretically reduced to a single line as illustrated in Figure 9.

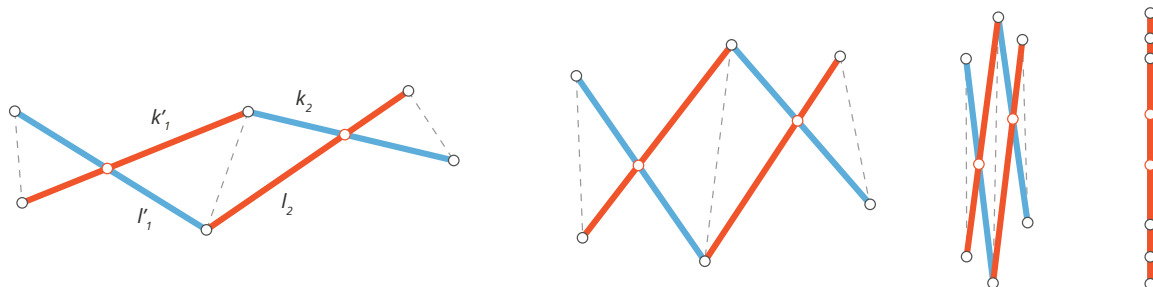


Figure 9: Illustration of Escrig's deployability constraint shown on two adjoining irregular scissor units in four stages of deployment.

When implementing scissor grids on regular surfaces displaying constant curvature and a high degree of symmetry, compliance with the deployability constraint is fairly straightforward. With the increasing complexity of a desired shape, for instance, when using freeform surfaces as base geometry, managing deployability constraints can become challenging. A novel approach to handle a higher degree of complexity efficiently, utilizing parametric computational models will be presented in Chapter 3.

2.3.4. Angulated units

Angulated units consist of two identical bars where the semi-lengths are kinked at an angle β . This way the endpoints and the intermediate hinge point are no longer aligned. Similar to polar units the unit lines also intersect, enclosing an angle γ . However, in the case of the angulated unit, the polar intersection angle remains constant during deployment, as the units deploy radially toward their perimeter (Fig. 10). For this to occur, the bar geometry has to fulfill the condition $\alpha = \gamma/2$ (Jensen, 2004). Angulated units are frequently referred to as Hoberman units, named after their inventor Chuck Hoberman. In form of the Hoberman sphere, it is widely popularized as a children's toy. Angulated units can cover a wide variety of shapes, including surfaces with double curvature.

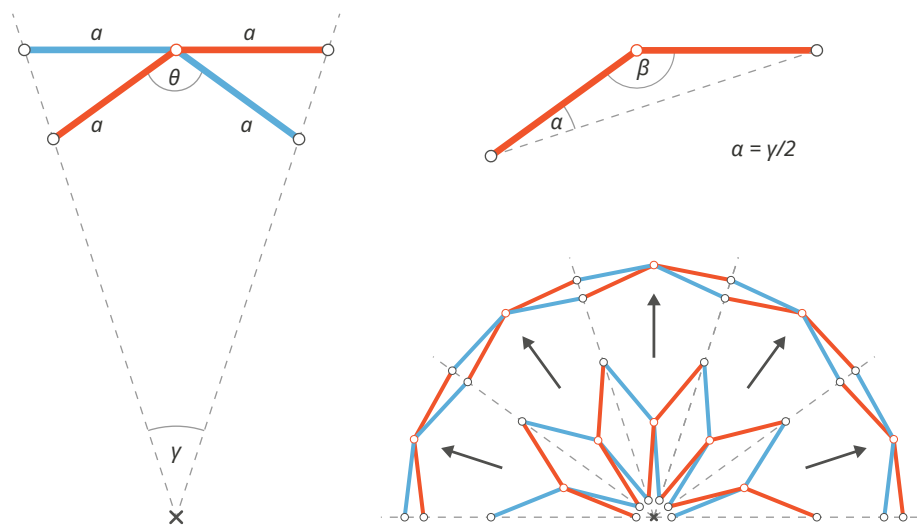


Figure 10: Angulated unit and geometric compatibility. Illustration of radial deployment.

As illustrated in Figure 10 the radial deployment results in a more compact composition when retracted towards the circular or spherical perimeter, which indicates why these structures are particularly well suited for retractable roofs, as proposed by Hoberman with the Iris Dome (Fig. 11), but not so much for transportation.

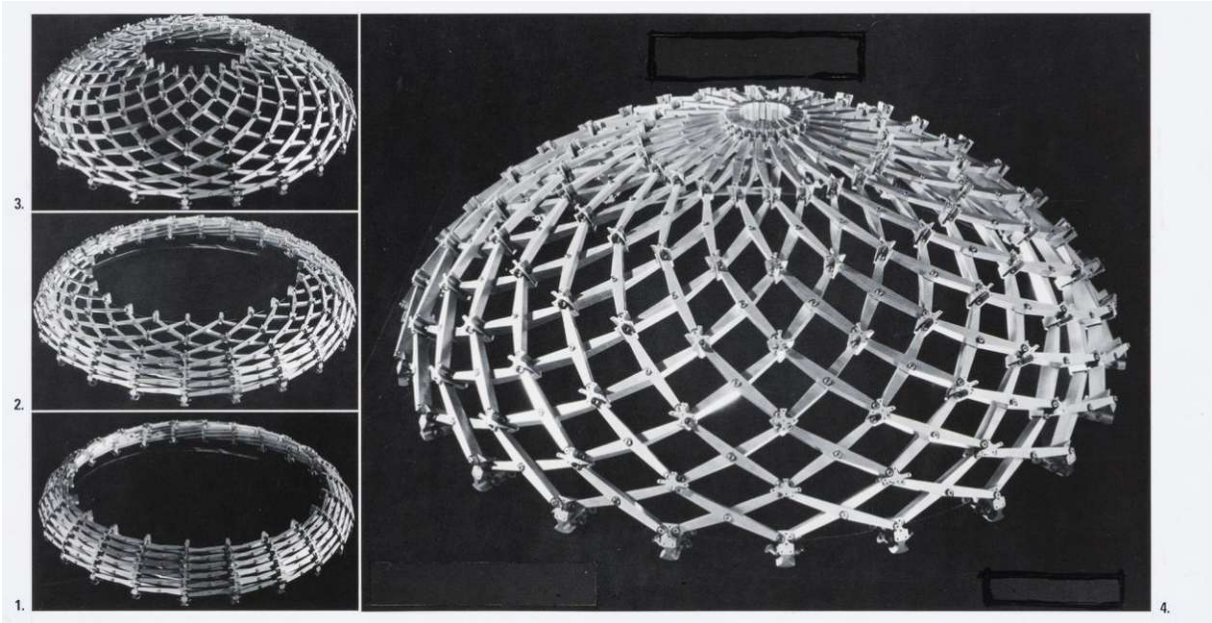


Figure 11: Iris Dome, working scale model (Hoberman Associates, 1993)

2.3.5. Discussion

Because of the fact, that grids consisting of straight bars can be folded into a more compact contracted state than their angulated counterparts and the implications that follow for storage and transportation, they are particularly well-suited and more commonly used for mobile applications. As the focus lies on mobile applications, structures consisting of straight bars with linear deployment behavior will be studied in greater detail within the framework of this master thesis.

2.4. Structures based on polar and translational units

Scientific research into deployable structures surged during the early era of space exploration. Due to the storage limitations of launch vehicles, they are widely used in aerospace technology until today. During the second half of the twentieth century, there has been a vivid interest in the field from architects like Buckminster Fuller, Frei Otto or Chuck Hoberman, who applied such principles in some of their most iconic architectural works during the 1960s and -70s (Ródenas-López, et al., 2020).

When researching deployable bar structures composed of double-layer grids, in particular, Spanish architect Emilio Pérez Piñero is commonly cited as a pioneer when it comes to their application to temporary buildings. In 1961 he was the first to patent a prototype for a

deployable dome spanning 32 meters, called the Mobile Theatre. His design consisted of rigid bars and tensioned wires, which act as bracing elements in the structure (De Temmerman, 2007). In 1965 he was commissioned to design a mobile exhibition pavilion. Made up of multiple modules with the measurements of 12x9 meters it covers a total area of 8000 m², making it the largest deployable structure of its day (Fig. 12). It was designed and built in Madrid, transported to San Sebastian where it was opened for the 25th anniversary of the end of the civil war. After the exhibition ended it was dismantled and transported to Barcelona as a permanent installation (Escrig, 2013). Piñero was a very productive researcher in the field, proposing various further designs for deployable structures and registering further patents until he died at a young age in 1972.

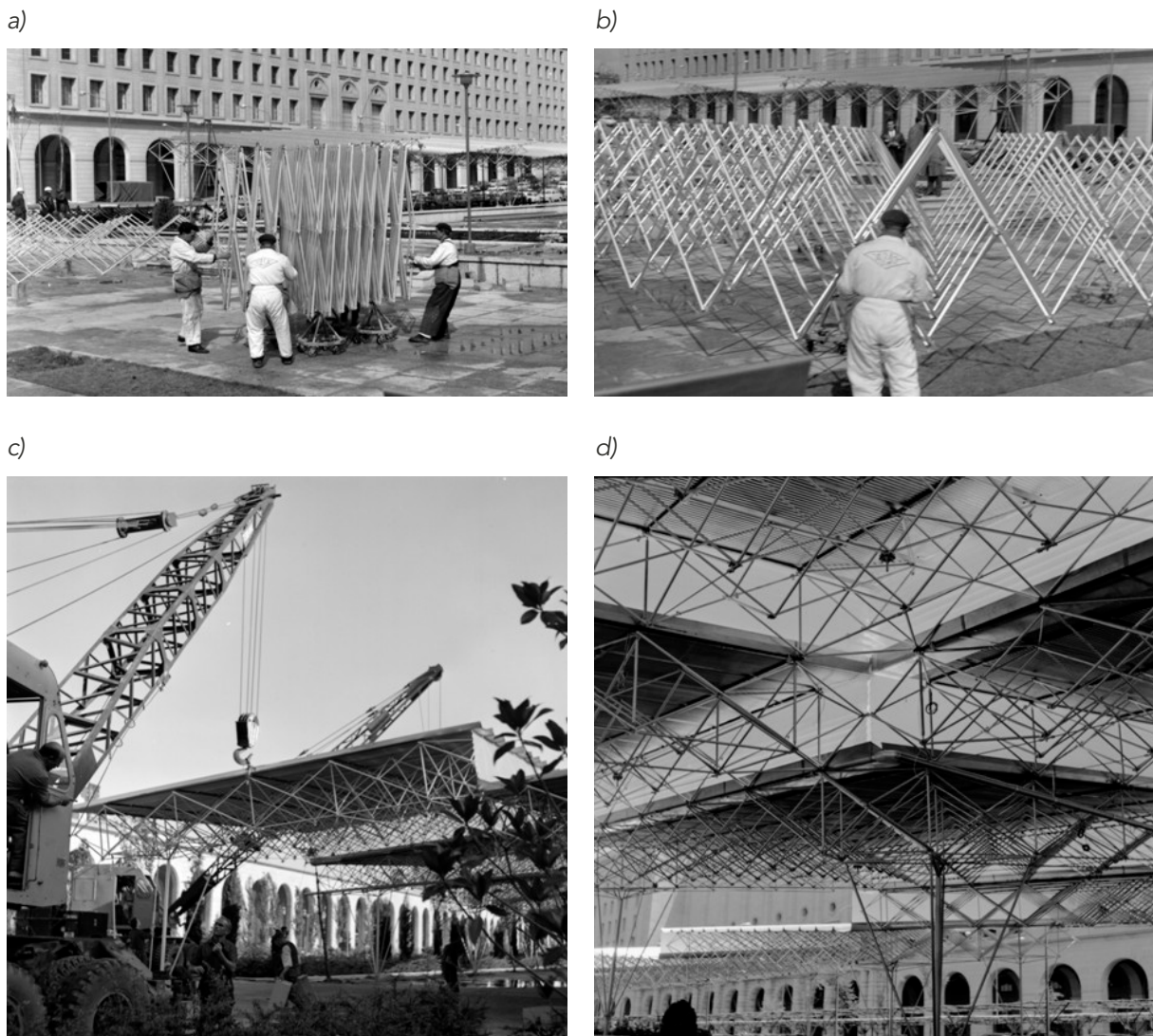


Figure 12: a) and b) Deployment process of multiple planar scissor grids build for a mobile exhibition pavilion. c) Lifting and interconnecting the individual grids to form a structure covering a total area of 8000 square meters. d) Fully deployed and installed roof structure (Escrig, 2013).

Felix Escrig, also a Spanish architect, became one of the most prolific researchers in the field of double-layer scissor grids during the 1980s and 90s. Building on Piñeros' work, he has published extensive works on the construction of planar grids with triangular and quadrangular modules and the implementation of curvature by moving the intermediate hinge away from the midpoint of the bars. In 1984 he described the deployability constraint for maximum compactness (Section 2.3.3). In collaboration with J. Pérez-Valcárel, he published further research on spherical triangular and quadrangular grids and their kinematics (Escrig & Pérez-Valcárel, 1993). Examples of their models are shown in Figure 13.

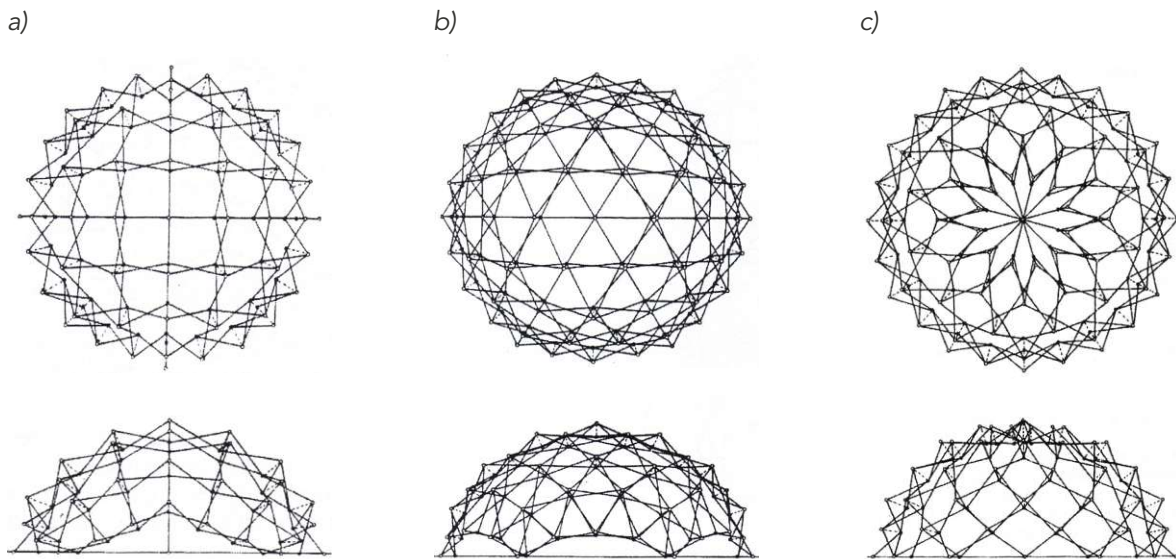


Figure 13: Top view and side elevation of an a) two-way spherical grid b) three-way spherical grid and c) lamella dome composed of polar units (Escrig & Pérez-Valcárel, 1993).

Besides publishing some fundamental research on the topic of deployable scissor structures Escric and Pérez-Valcárel also collaborated on the building of a cover for the municipal swimming pool of San Pablo Sports Centre in Seville 1996 (Fig. 14). This is a particularly interesting example in the context of this thesis as it represents one of the few realized large scale, mobile and reusable double layer scissor grids, in frequent use outside of military and aerospace applications. The design consists of two identical spherical domes, subdivided by a uniform rhomboid pattern, constructed as a grid of identical polar scissor units. Each dome covers an area of 30x30 m, with a rise of 7 m at the highest point. Another remarkable feature of the design is the execution of straight outer edges, on a rectangular base area. This allows several of the domes to be connected, opening the possibility of a growing array (Sanchez, et al., 1996) The cover was in use only during the cold season, and due to limited surrounding space had to be stored at an off-site location during the rest of the year.

Consequently, the structure had to be transported twice a year with a week's time for installation or dismantling respectively (Fig. 15 a and b). The material used for rods and joints was aluminum with a thin membrane cover attached (Fig. 16). Due to the uniform grid geometry, the deployment process was friction-free making it a foldable mechanism. Therefore, the structure had to be stabilized with additional bracing elements when deployed and in use.



Figure 14: Cover for the municipal swimming pool of San Pablo Sports Centre in Seville.



Figure 15: a) Fully contracted structure. b) Deployment process. c) Interior view when fully installed.

When a scissor grid configuration behaves like a foldable mechanism, the structure will remain completely stress-free during deployment. Their kinematic counterparts are called bi-stable grids, which are stress-free only when fully contracted or deployed, but go through geometric incompatibilities in the intermediate process of transformation (Roovers & De Temmerman, 2017).

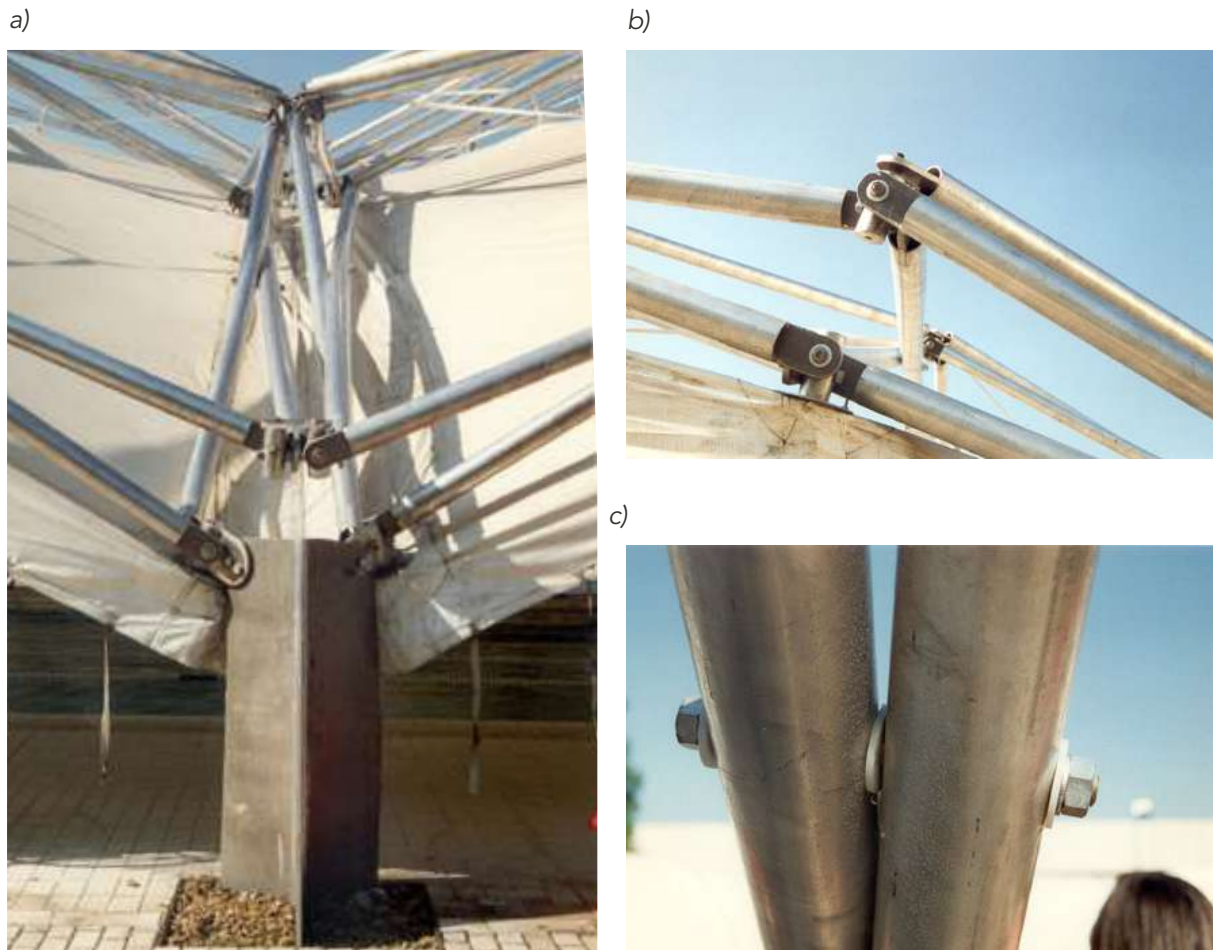


Figure 16: a) Anchoring detail. b) Linkage detail. c) Hingepoint detail.

T. R. Ziegler was the first to publish research on utilizing this property of bi-stable grids as a self-locking mechanism to eliminate the need for extra stabilization with wires or plates. C. J. Gantes (2001) has further studied bi-stable deployable structures, their nonlinear structural behavior, and material requirements by simulation of the deployment process.

Travis Langbecker (2000) at the University of Queensland School of Engineering conducted a geometric and kinematic analysis on scissor grids consisting of translational units with positive and negative gaussian curvature (Fig. 17). The effect of varying member sizes, depth-to-span ratio, rise-to-span ratio, grid density, and geometric imperfections were examined. By

using uniform translational units with a constant structural thickness throughout the entire structure these configurations always display a stress-free deployment process.

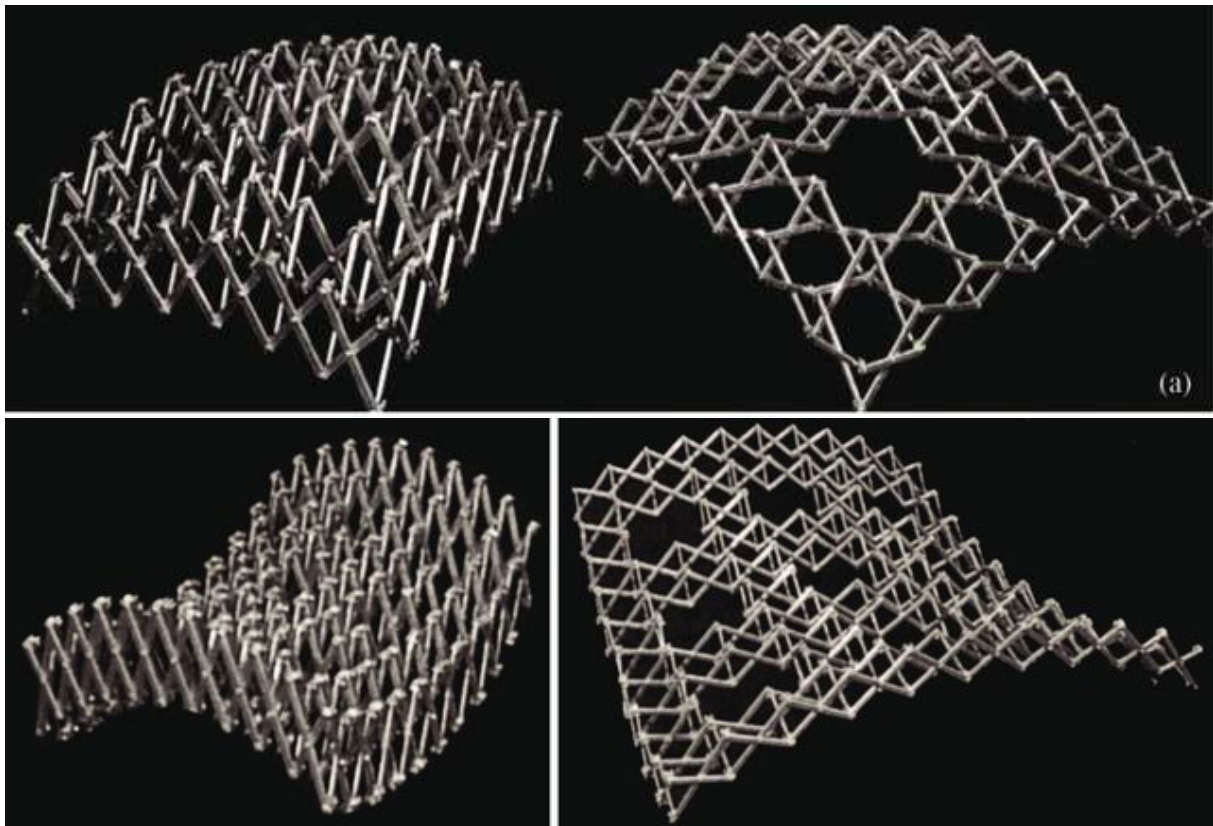


Figure 17: Translational scissor grids with positive and negative gaussian curvature in two deployment stages (Langbecker & Albermani, 2000)

2.5. Discussion

The review of literature shows, that various combinations of scissor units can result in a multitude of deployable grids, when abiding to certain constraints for geometric compatibility. While it is relatively easy to design scissor grids on flat or single curvature surfaces with a high degree of symmetry, the process becomes more complex when designing spatial grids with double or freeform curvature. This can present a challenge when desiring more versatility in shape and function. Scissor grids that are composed of translational units offer an exception. They can be applied to a wide variety of shapes, while the design issues are reduced to a set of two-dimensional problems (Roovers & Temmerman, 2017).

3. DESIGN METHODS

3.1. Introduction

The previous chapter has illustrated, how the process of designing deployable scissor structures becomes challenging when pursuing more complex configurations than flat, spherical, or cylindrical grids. Parametric modeling environments, which are widely used in architectural design today, offer methods to handle this degree of complexity efficiently.

The following chapter briefly presents the digital tools, employed for the design, simulation, and analysis of deployable scissor grids. Further on, it gives an overview of methods for designing geometrically compatible grids within a parametric modelling environment utilizing these tools. These methods are then applied to several grid configurations to provide insight into the variety of suitable shapes and their kinematic behavior.

3.2. Digital tools

3.2.1. Grasshopper

Grasshopper is a node-based editor, included in the 3D modelling software Rhino3D. Because of a visual interface, node-based editors give users with little experience in textual programming, accessible means to create generative algorithms and complex 3D models. Such programming interfaces are particularly useful for parametric design, where a model can interactively be modified through the use of variables and functions and is used in a variety of fields, including architecture and engineering.

In Grasshopper, the user creates programs by placing and interconnecting different nodes, the so-called components, that represent functions or data. This can be done in a variety of ways to quickly create complex designs with interactive control and real-time visualization. The basic setup offered in Grasshopper is already extensive, in addition to this, there exist various plug-ins, to further expand its capabilities e.g. tools for physical simulation, structural analysis, and optimization. It also allows the user to implement his own components by programming in C# or Python.

3.2.2. Particle spring systems

Particle spring systems are used to simulate the behavior of physical objects that are composed of interconnected particles. These systems are often used in 3D modeling to create realistic simulations of objects that exhibit complex, flexible behaviors. In a particle spring system, each particle represents a point in space and is connected to other particles by springs. The properties of the springs, such as their stiffness and rest length, determine how the particles behave when they are moved or subjected to external forces.

Kangaroo2 is a physics engine, developed by Daniel Piker, that can be used to simulate particle spring systems and is implemented as a plugin for Grasshopper. It is frequently used as a form-finding tool, similar to analog methods like hanging models and soap films utilized by architects like Heinz Isler or Frei Otto.

3.2.3. Finite element method

The finite element method is a numerical technique used to solve partial differential equations that describe physical systems. It is commonly used in engineering to analyze and optimize complex structural systems. In the FE method, a continuous system is divided into a set of discrete elements (finite elements), each of which is described by a set of algebraic equations. These equations are assembled into a larger system determining the behavior of the system.

Karamba 3D is a structural engineering software based on the FE method. It is implemented as a plugin for Grasshopper. By specifying the geometry and the material properties of a structure, as well as any loads or boundary conditions that will act on the system, the solver will then calculate the forces and deformations of the elements, allowing analysis and optimization of the model.

3.3. A design method based on circle packing

A novel approach to designing geometrically compatible deployable scissor grids, utilizing Grasshopper and Kangaroo2 is proposed by Roovers & De Temmerman (2015). The method they describe for designing DLGs in compliance with the deployability constraint (Section 2.3.3) is based on circle packing and can be used to discretize a wide range of base surfaces into a compatible mesh geometry, which will form the base grid of a deployable scissor structure.

3.3.1. Planar grids

To ensure, that a linkage of multiple units can be contracted into its most compact state, where all bars are aligned and theoretically reduced to a single line, the sum of the semi-lengths of a scissor unit has to equal the sum of the semi-lengths of the adjoining unit. It is expressed in the following Formula:

$$k'_1 + l'_1 = k_2 + l_2$$

In the case of planar grids, composed of plane-translational units where generally all the semi-lengths are equal, this equation is reduced to

$$k'_1 = l'_1 = k_2 = l_2$$

As the bars of such scissor grids form a chain of isosceles triangles, it is possible to translate any configuration of planar circle packing into a double-layer grid of translational scissor units (Fig. 18), where each pair of tangential circles contain a scissor unit, with the intermediate hinge is located at the point where the circles touch while the unit lines perpendicularly pass through their respective centers (Roovers & De Temmerman, 2015).

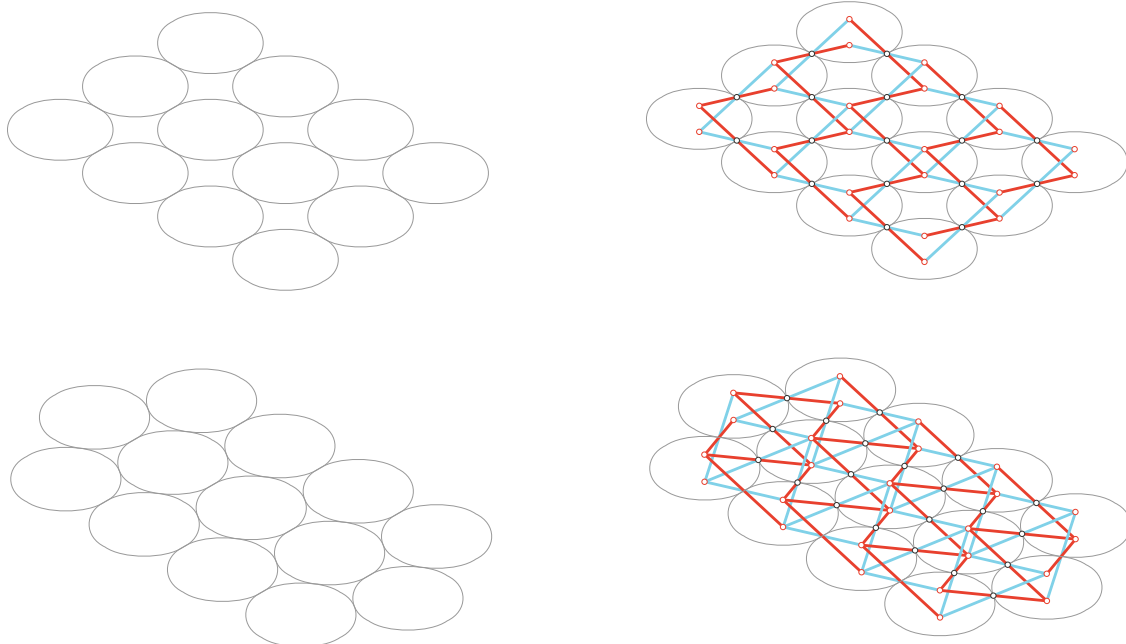


Figure 18: Square and hexagonal circle packing and the resulting 2-way and 3-way grid, as in Roovers & De Temmerman (2015)

3.3.2. Spherical grids

Spherical surfaces can also be populated by dense circle packings, which can then be transformed into deployable scissor grids. As in the case of planar grids, each pair of tangent circles corresponds to a scissor unit and again, this results in a configuration where the intermediate hinge points are located where the circles touch, while the unit lines pass through the respective centers (Fig. 19). Since this is a curved surface this grid will be constructed with polar, angulated or curved-translational units. In the case of polar and angulated units the unit lines are perpendicular to the centers of the circles and intersect at the center of the sphere. In case of curved-translational units the unit lines are parallel (Roovers & De Temmerman, 2015).

To create a deployable scissor grid on a spherical surface, the initial mesh is designed to hold a dense pattern of circle packing. The scissor units are then placed within this mesh. The design flexibility for this process lies in the creation of the initial mesh, which can be based on an arbitrary point cloud, a planar mesh projected onto a sphere, or a geodesic grid.

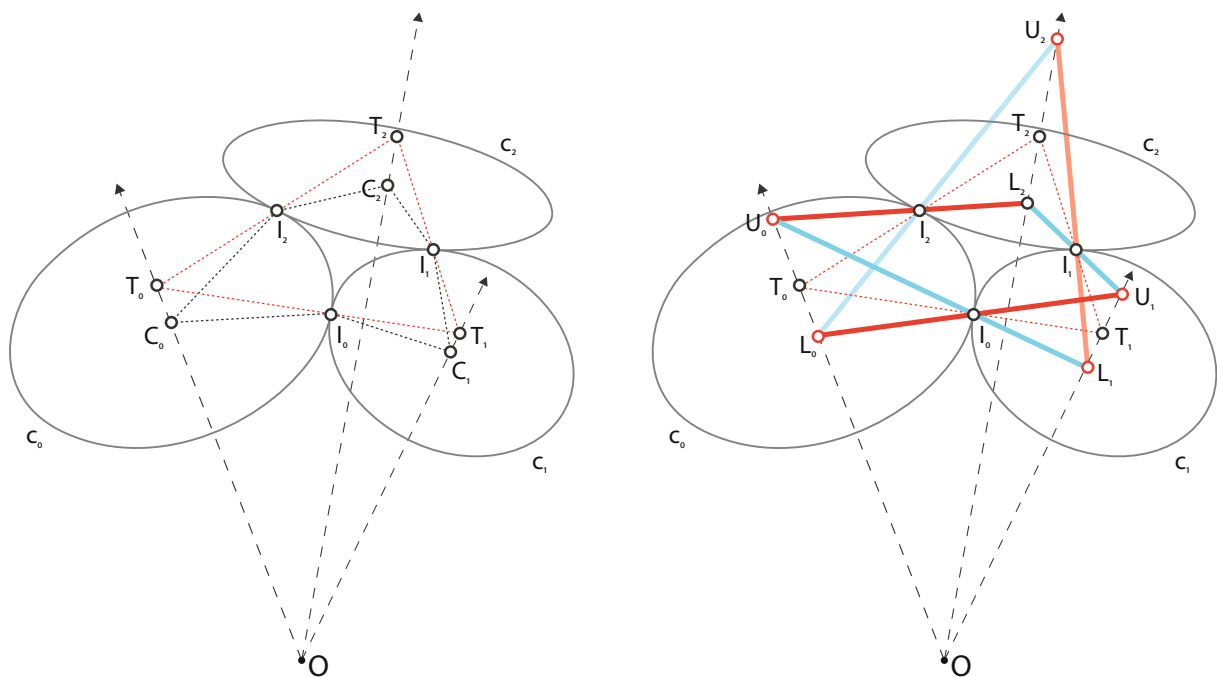


Figure 19: Populating three tangent circles by polar units. As in Roovers & De Temmerman (2015)

3.3.3. Other grids

Circle packings can also be placed on surfaces other than a sphere, such as surfaces of revolution or freeform surfaces. However, it is only possible to form three mutually tangent circles on a sphere or a flat surface. Therefore, it is not possible to create double-layer grids with triangular cells on other types of surfaces. Additionally, a resulting quadrangular grid on surfaces with double curvature can only be populated with angulated or translational units.

3.4. Modelling and Simulation

The previous section showed how, by packing tangential circles on a given base surface, this surface can be discretized into a mesh where the vertices will be the circles' center points. The base mesh can then be populated by scissor units, resulting in a double-layer scissor grid compatible with the deployability constraint.

3.4.1. Modeling prismatic modules by mesh face

Once a given base surface has been discretized into a mesh (i.e. by circle packing), vertices have to be sorted. After sorting, these points will be offset in the direction of the unit lines, at a distance determining the structural thickness, thereby becoming the second layer of endpoints in a deployable scissor grid. This is illustrated in Figure 20.

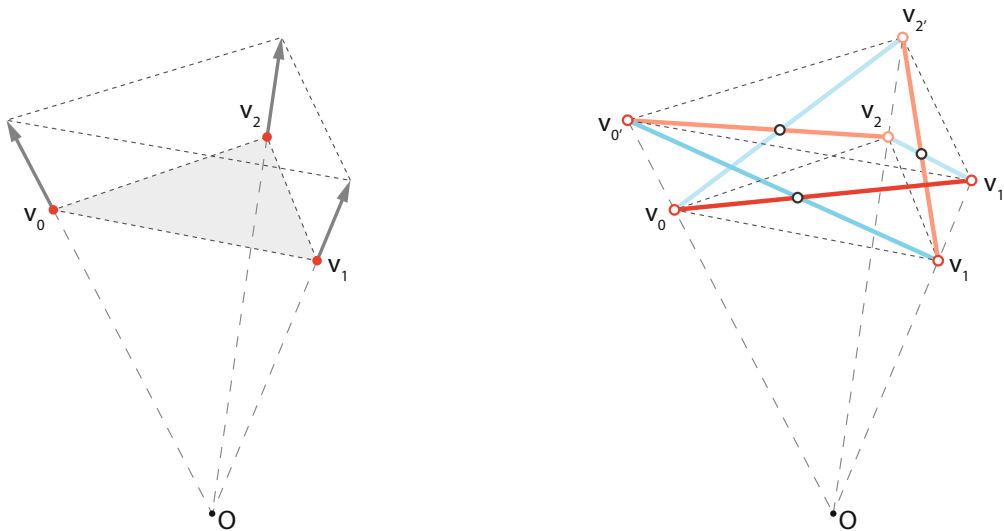


Figure 20: Generating prismatic scissor modules by mesh face. Vertices and offset vectors are sorted, offset, and connected to form endpoints of the scissor units.

One method is sorting the vertices by mesh face, performing the offset, shifting the indices on the upper layer, and connecting them to form scissor modules. This is illustrated in Figure 20. In the end, duplicate lines have to be deleted and the remaining lines have to be sorted in pairs belonging to each unit, forming the input for a simulation of the deployment with Kangaroo2. This is a quick method; the Grasshopper script remains fairly slender (Fig. 21).

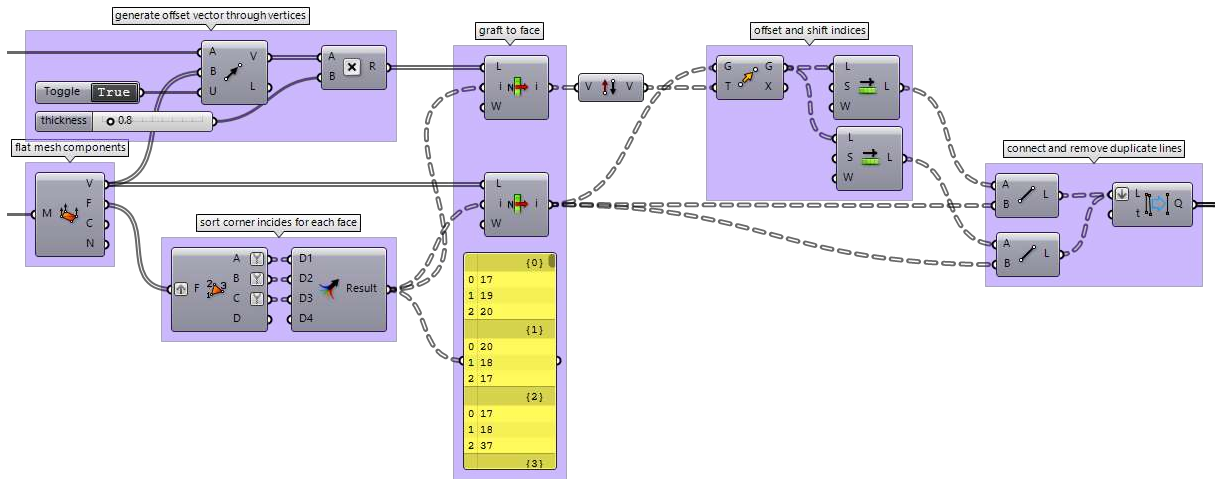


Figure 21: Grasshopper definition for generating prismatic scissor modules by mesh face.

3.4.2. Modeling linkages as a UV network

The method described in the previous section is suitable for a quick proof of concept regarding the deployability and maximum compactness of a scissor grid. For detailed modeling of scissor bars, hinges, and nodes it is not the best approach. An alternative strategy is modeling the grid as a network of linkages in u and v directions.

When generating the scissor modules by mesh face, the operation runs in direction of vertex numbering - counterclockwise. To generate a detailed structural model fulfilling the mechanical properties of a scissor grid, the bars of a scissor unit have to be offset in the direction of their vector cross-product, to accommodate the dimensions of its building members. In the case of module generation by mesh face, these cross-vectors will also run counterclockwise (Fig. 22), which leads to an undesirable data structure for modeling a detailed structural system of cross-sections, hinges, and node connectors for later structural analysis, fabrication, and assembly.

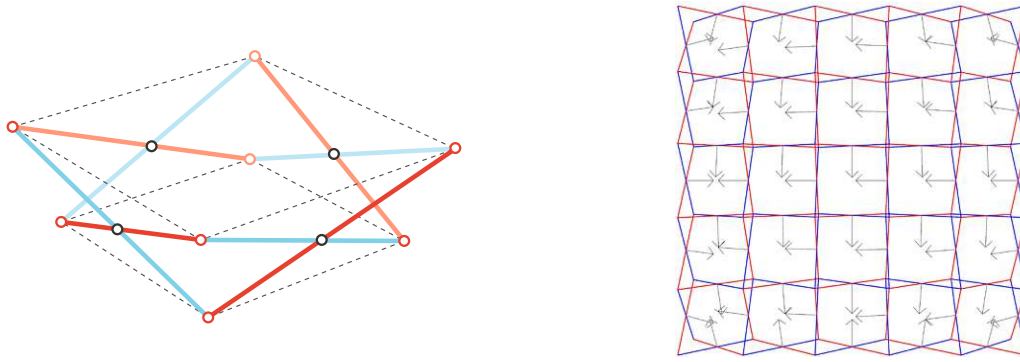


Figure 22: Modelling prismatic scissor modules on quadrangular mesh faces. Vertices are sorted counterclockwise; the orientation of the offset vectors flips.

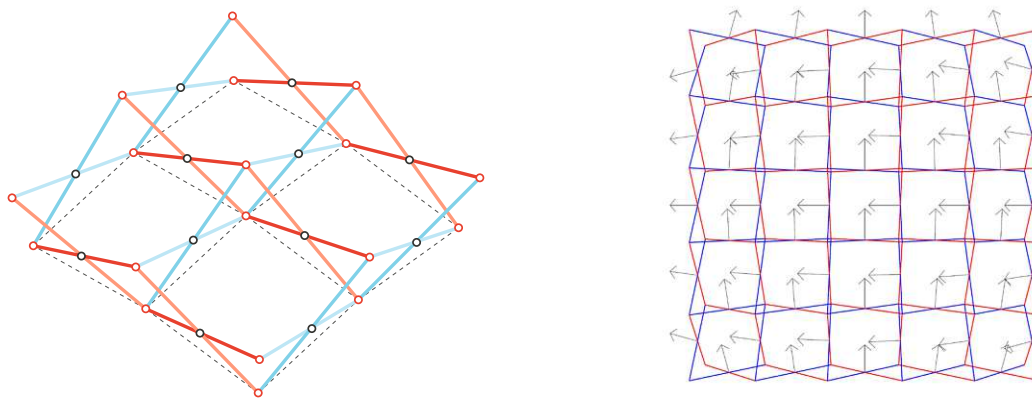


Figure 23: Modelling scissor linkages along a UV network. Offset vectors are oriented in a uniform direction.

A suitable solution to eliminate this problem is to sort the mesh vertices as a network of points in u and v direction and not by mesh face. This way all cross-vectors are oriented correctly (Fig. 23).

3.4.3. Deployment simulation with Kangaroo2

Besides using Kangaroo2 for form-finding and mesh optimization when designing geometrically compatible double-layer grids later on, it will also be utilized for a simulation of the deployment process. This simulation is useful to monitor foldability and compactness. In combination with a fully detailed structural model, determining the necessary member dimensions it provides information on transport size, which informs the designer if a base geometry needs to be adjusted to fit storage or dispatch size.

The variable which is used to operate the deployment will be the angle θ , which is enclosed between two semi-lengths of a scissor unit. This angle is measured when the structure is completely deployed and remapped to a parameter c for compactness. Where $c=0$ represents full deployment, while $c=1$ transforms the angle θ between the scissor bars to 180° when the two bars of a scissor unit are completely aligned – theoretically reducing the unit to a single line (Fig. 25). Only grids that fulfill the deployability constraint, i.e. grids designed by circle packing can be contracted completely.

Additional constraints for the simulation are: Fixing the length of the semi-lengths resulting from dividing a pair of bars at their intermediate hinge point, and keeping them antiparallel to each other – thereby keeping the bars of a scissor unit straight and the position of the hinge point from changing during the simulation (Fig. 24).

When using the output lines from the deployment simulation to offset and model the cross-sections, hinges, and nodes, it can provide information on how far the structure can be contracted before the individual members collide - giving insight into volume expansion ratio and transport size.

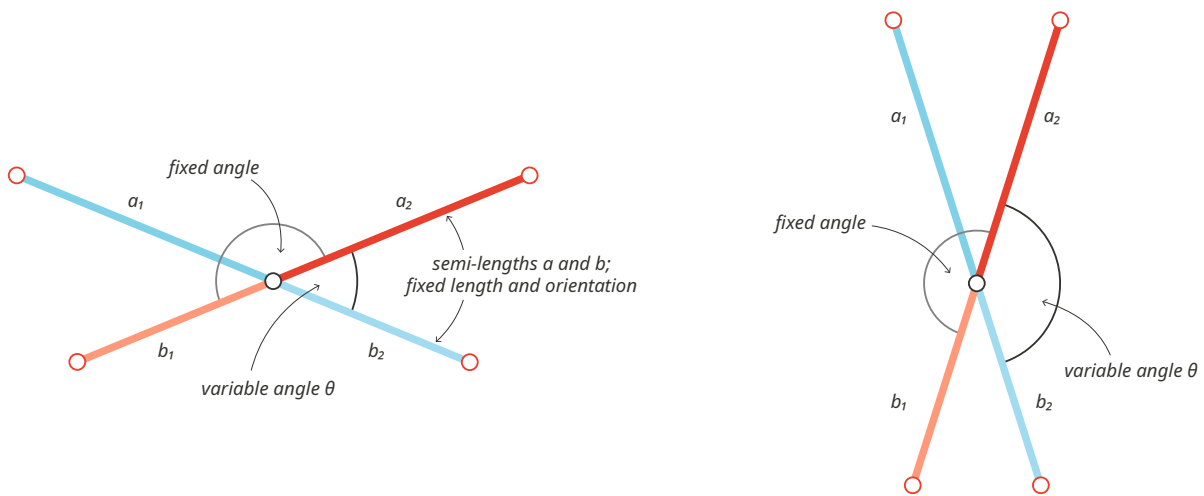


Figure 24: Simulation parameters: Angle between outer layer semi-lengths a_1 and a_2 and inner layer semi-lengths b_1 and b_2 serves as a variable for deployment. Additional constraints are to keep all bars same length and to keep line-segments antiparallel (straight).

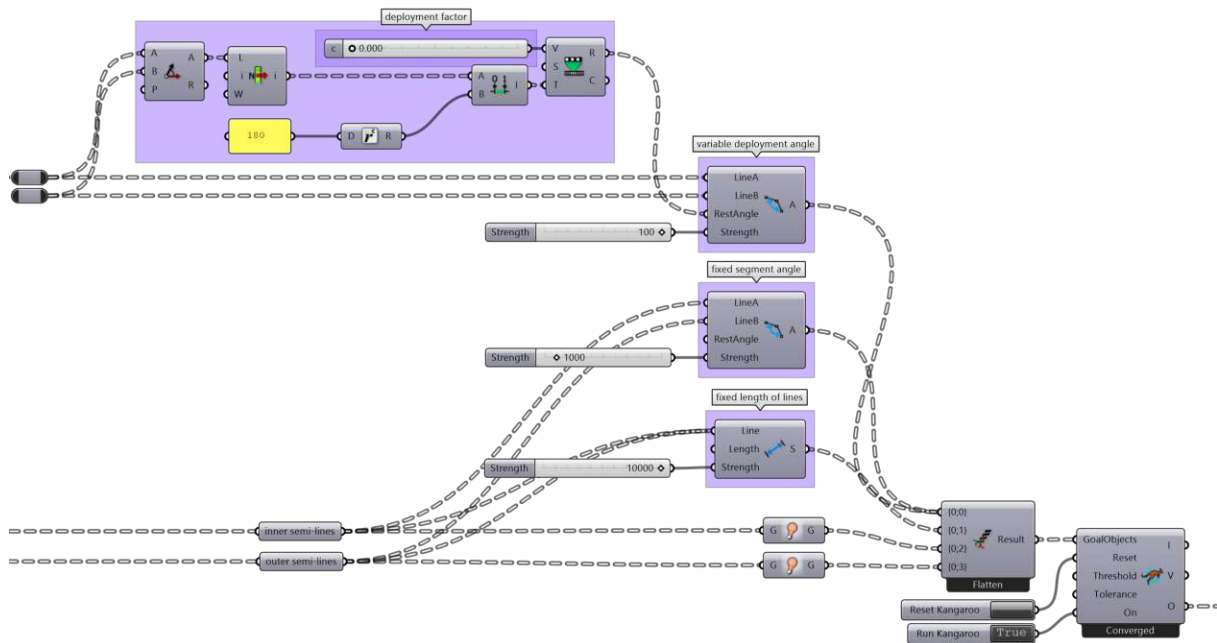


Figure 25: Deployment simulation setup; initial angle between semi-lengths is measured in completely deployed state ($c = 0$) and can be varied to a degree where all the bars are aligned and the grid is theoretically reduced to a single line ($c = 1$).

3.4.4. Discussion

The digital tools and methods presented, offer various strategies for designing geometrically compatible deployable scissor grids. Optimizing mesh topology to hold a dense pattern of circle packing presents a promising approach for monitoring deployability constraints during the initial process of form-finding. The need to account for a data structure, suitable for modeling the structure in detail, and for a later fabrication and assembly, while generating a scissor grid, was addressed. The goals for simulating the deployment process using Kangaroo2 were defined and explained. The next section will apply the presented methods to produce a variety of grid configurations.

3.5. Digital experiments

In the following section, the principles and methods covered so far are applied to a series of different base surfaces. The goal is to establish and refine a strategy for scissor grid design and deployment simulation working with line models and converge towards a working setup for the final case studies.

3.5.1. Spherical domes

To demonstrate how the deployability constraint can be equated to a compact circle packing on a surface the first model shows a geodesic dome (Fig. 26), where the grid follows a pattern of tangential circles by default.

3V GEODESIC DOME					
unit type	thickness [m]	scissor bar quantity [n]	scissor bar length [m]	BB dim c=0 [m]	BB dim c=0.95 [m]
polar	0.80	240	180x 2.40	L = 11.18	L = 1.08
			60x 2.00	H = 4.94	H = 2.36

Table 2: Model specifications - 3v geodesic dome.

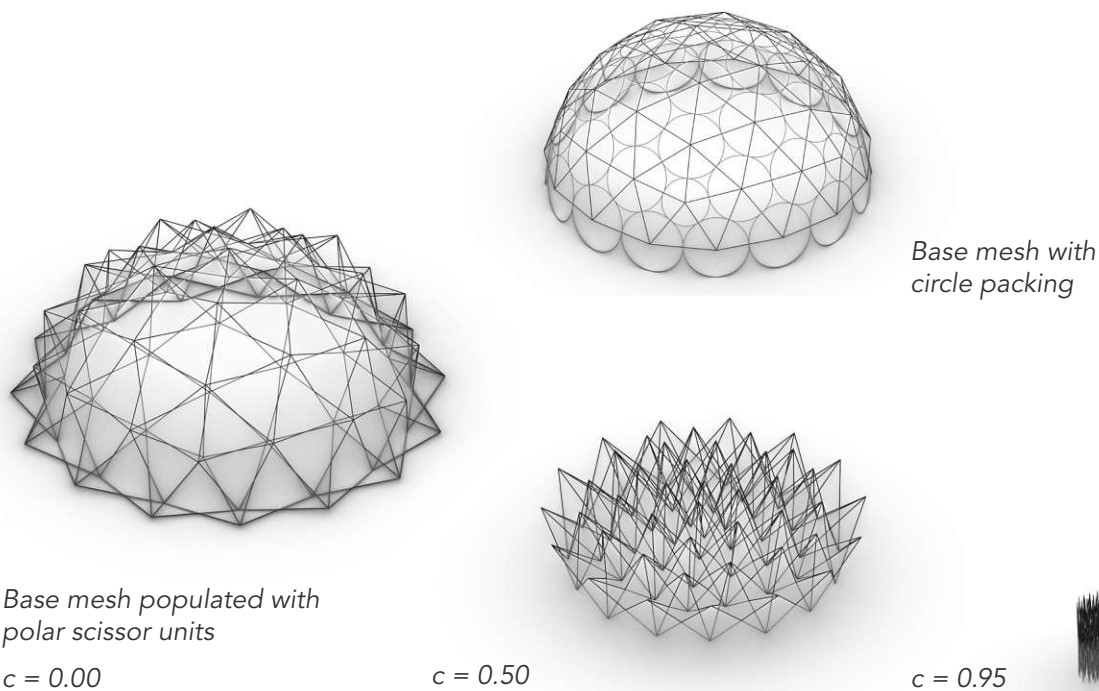


Figure 26: 3v geodesic dome with the corresponding pattern of tangential circles. The mesh is populated with polar scissor units and illustrated in three stages of deployment.

The next model shows a spherical dome subdivided by a uniform rhomboid pattern (Fig. 27), constructed as a grid of identical polar scissor units. The base grid was derived by projecting a square grid onto a spherical surface.

UNIFOR RHOMBOID SPHERICAL DOME					
unit type	thickness [m]	scissor bar quantity [n]	scissor bar length [m]	BB dim c=0 [m]	BB dim c=0.95 [m]
polar	1.00	168	2.40	L = 12.85	L = 0.84
				H = 3.86	H = 2.37

Table 3: Model specifications - uniform rhomboid spherical dome.

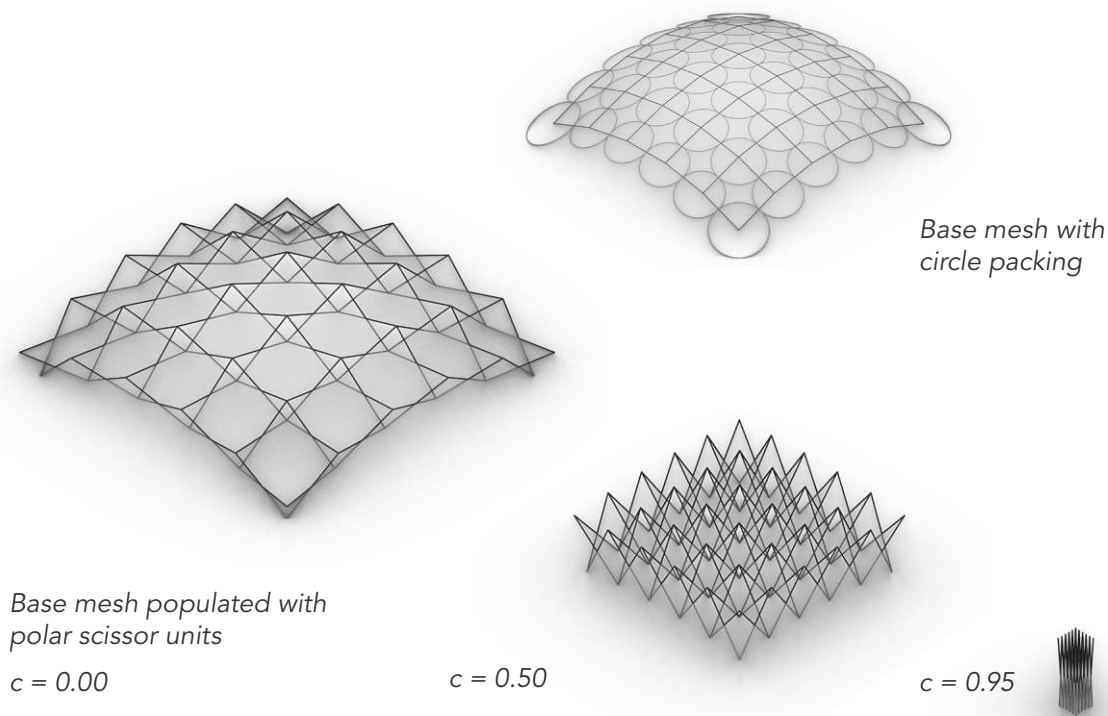


Figure 27: Uniform rhomboid spherical dome with the corresponding pattern of tangential circles. The mesh is populated with identical polar scissor units and illustrated in three stages of deployment.

The final experiments on a spherical surfaces apply a mesh triangulation method based on a pattern of tangential circles as described in section 3.3.2. Starting with a subdivided quad-sphere patch where the subdivision points are used in a Delaunay triangulation. The resulting triangulated mesh topology is then optimized to hold a circle packing where the vertices are at the center points of the tangential circles using Kangaroo2 (Fig. 28 and 29).

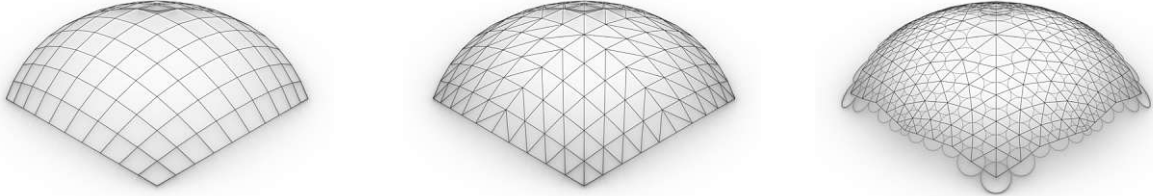
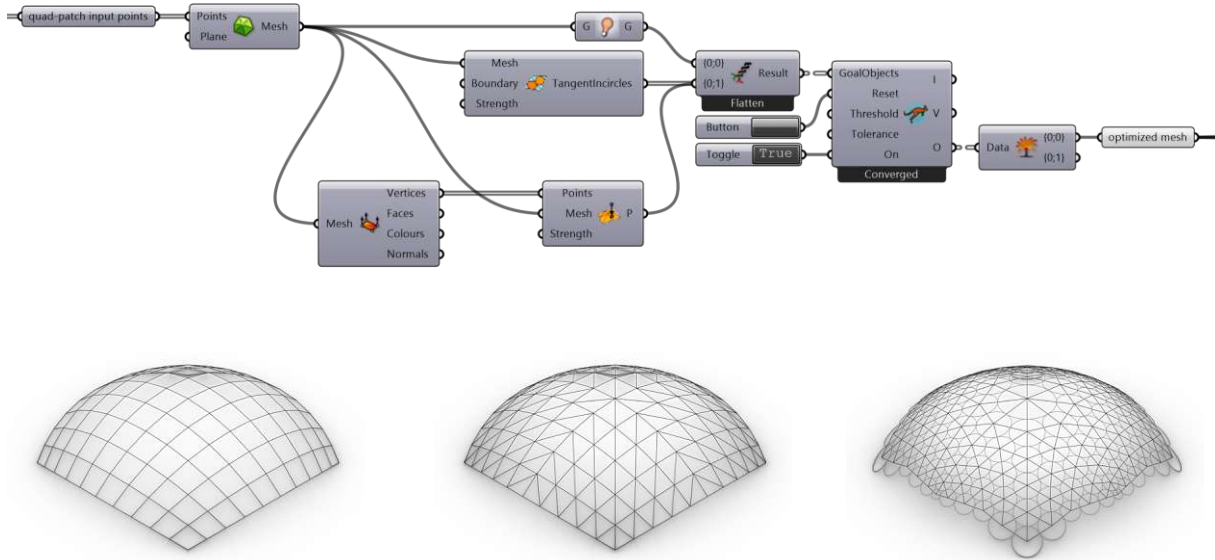
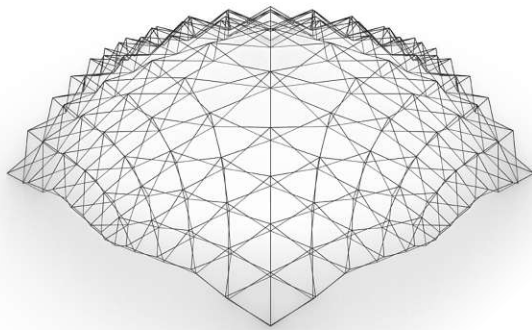


Figure 28: Grasshopper definition of mesh topology optimization to hold a circle packing where the vertices are at the center points of the tangential circles using Kangaroo2.

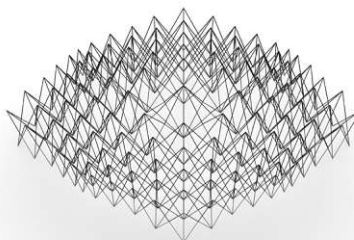
TANGENT CIRCLES SPHERICAL DOME I					
unit type	thickness [m]	scissor bar quantity [n]	scissor bar length [m]	BB dim c=0 [m]	BB dim c=0.95 [m]
polar	0.70	640	min. 0.94	L = 12.54	L = 1.54
			max. 2.35	H = 3.92	H = 2.29

Table 4: Model specifications - tangent circles spherical dome I.



Base mesh populated with polar scissor units

$c = 0.00$



$c = 0.50$



$c = 0.95$

Figure 29: Spherical dome with triangulation based on circle packing I. The mesh is populated with polar scissor units and illustrated in three stages of deployment.

By optimization of a triangular mesh topology to hold a pattern of mutually tangential circles it is possible to quickly generate a double layer scissor grid of any triangulated spherical mesh.

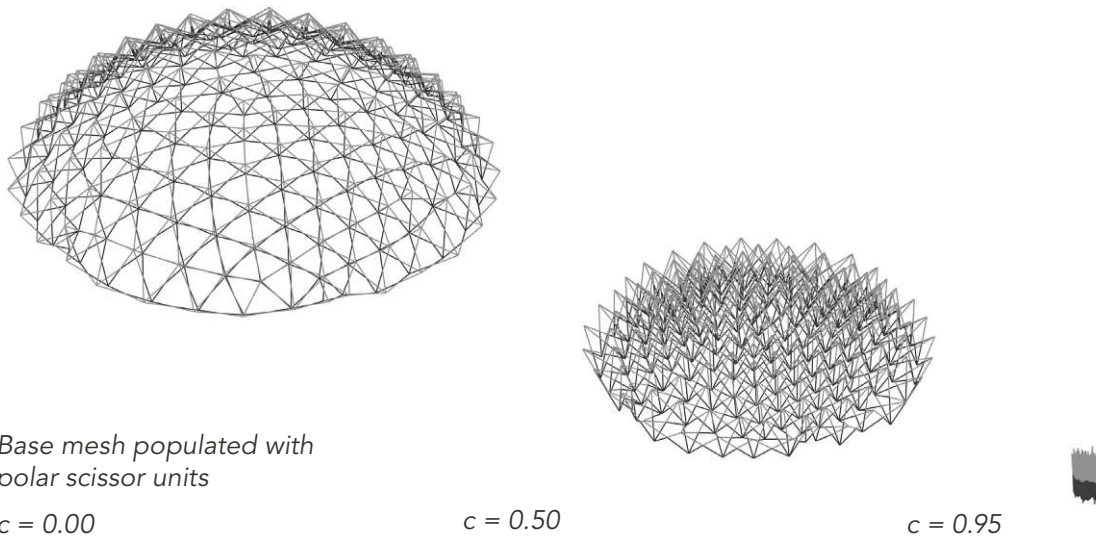
An example of this is shown in Figure 30 and 31. A spherical surface is converted into a mesh of near equilateral triangles, then the topology is optimized to hold a dense circle packing. This base mesh is then used to generate a double layer scissor grid.



Figure 30: Near equilateral triangular mesh topology optimization to hold a dense circle packing using Kangaroo2.

TANGENT CIRCLES SPHERICAL DOME II					
unit type	thickness [m]	scissor bar quantity [n]	scissor bar length [m]	BB dim c=0 [m]	BB dim c=0.95 [m]
polar	0.70	970	min. 1.05	L = 18.23	L = 1.67
			max. 2.22	H = 5.66	H = 2.08

Table 5: Model specifications - tangent circles spherical dome II.



Base mesh populated with polar scissor units

$c = 0.00$

$c = 0.50$

$c = 0.95$

Figure 31: Spherical dome with triangulation based on circle packing II. The base mesh is populated with polar scissor units and illustrated in three stages of deployment.

3.5.2. Rotational and Translational surfaces

A rotational surface in the shape of a cylindrical vault is used as a base surface to generate a deployable scissor grid of uniform polar units in the transverse direction and uniform plane-translational units in the longitudinal direction (Fig. 32). The combination of uniform polar and translational units results in a completely stress-free deployment process.

CYLINDRICAL VAULT					
unit type	thickness [m]	scissor bar quantity [n]	scissor bar length [m]	BB dim c=0 [m]	BB dim c=0.95 [m]
polar	1.00	72	2.35	L/W = 15.60/12.00	L/W = 0.69/2.15
translational	1.00	72	2.19	H = 6.00	H = 2.32

Table 6: Model specifications - translational grid with double curvature.

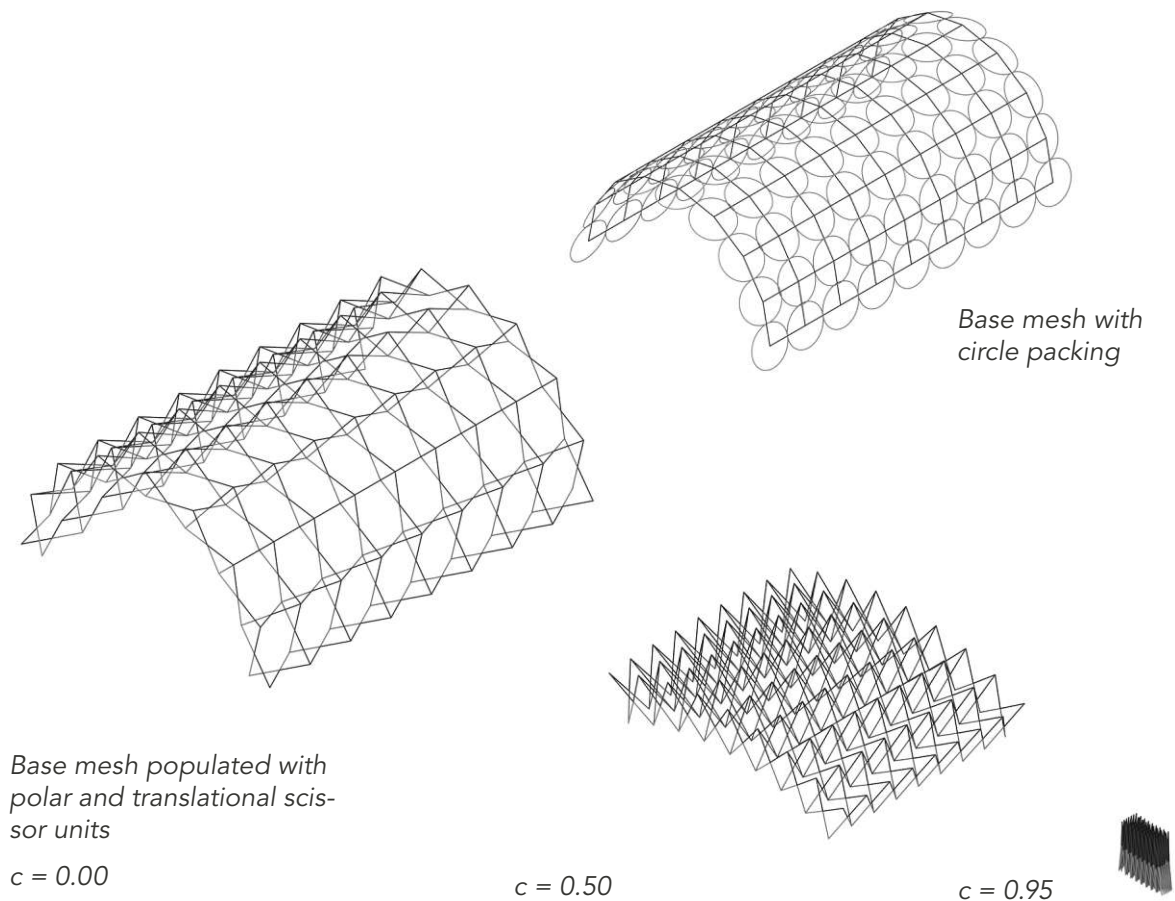


Figure 32: Cylindrical vault consisting of uniform polar and plane-translational scissor units, resulting in stress-free deployment behavior, illustrated in three states of deployment.

A translational surface, subdivided by length to form a uniform rhomboid grid holding a compact circle packing is shown in Figure 33. This base grid is then populated by curved-translational scissor units, where the scissor bars have different lengths. Because the given base surface is not spherical but shows double curvature in some areas, only curved-translational or angulated units can be used to construct deployable scissor grids on double curvature surfaces (Section 3.3.3). Again, this results in a stress-free deployment process.

TRANSLATIONAL GRID WITH DOUBLE CURVATURE					
unit type	thickness [m]	scissor bar quantity [n]	scissor bar length [m]	BB dim. c=0 [m]	BB dim. c=0.95 [m]
curved-translational	1.00	220	min. 3.29	L/W = 28.86/20.00	L/W = 2.73/1.39
			max. 4.46	H = 8.91	H = 5.95

Table 7: Model specifications - translational grid with double curvature.

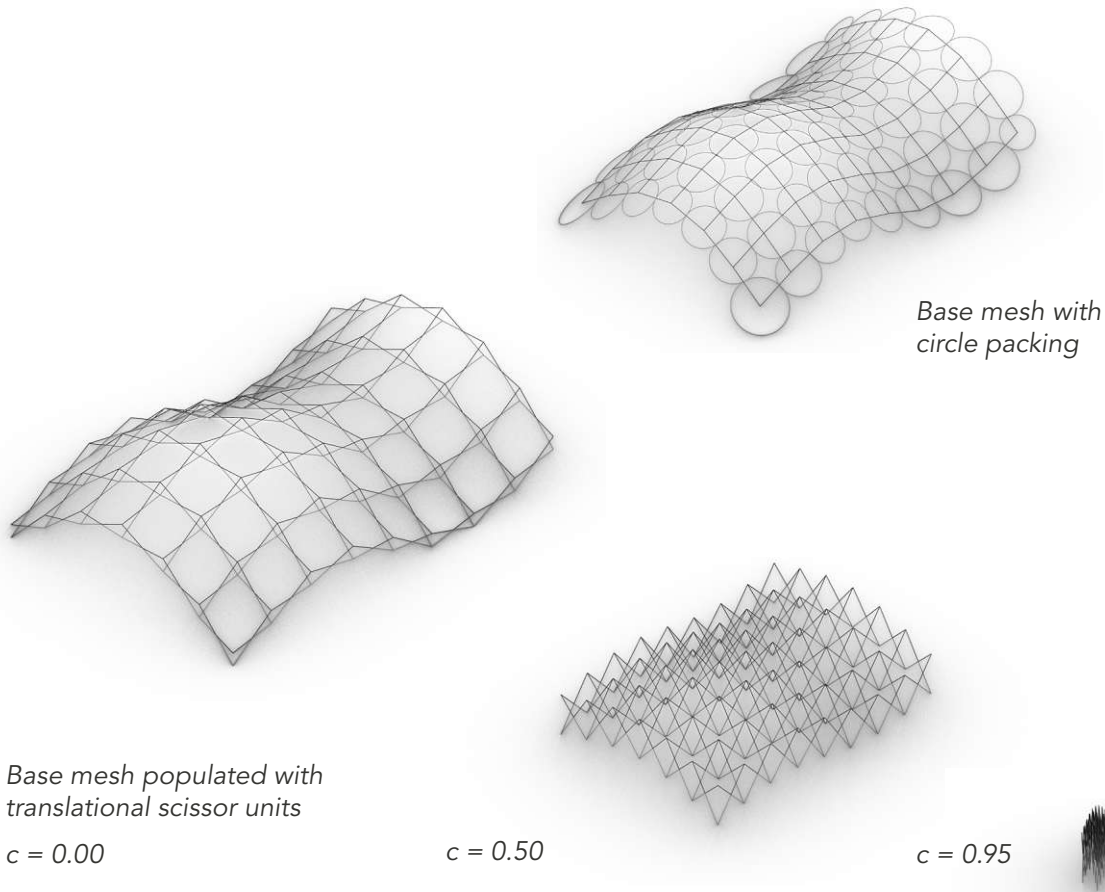


Figure 33: Translational surface with double-curvature, uniform rhomboid subdivision pattern, populated with curved-translational units. Three stages of deployment, completely stress-free.

3.5.3. Other surfaces

When it comes to using freeform surfaces as base geometry for designing foldable scissor grids, form-finding tools like mesh relaxation can provide a suitable approach. Mesh relaxation consists of a procedure for iteratively making the mesh topology smoother. It can be used to simulate minimal surfaces, akin to the soap film models used by architects like Frei Otto. The digital application of such a form-finding process can be quickly set up within Kangaroo2. By adding different goals to the solver, various types of meshes can be generated and controlled, other than meshes approximating minimal surfaces.

One such mesh typology, which can be helpful when designing geometrically compatible deployable scissor grids, is that of cyclic quadrilaterals. In Euclidian geometry, a cyclic quad is described as a four-sided shape that can be inscribed into a circle (Marshall & Eppstein, 1999). Each vertex of the quadrilateral lies on the circumference of the circle and is connected by four chords. Figure 34 shows the Grasshopper definition of a mesh relaxation from a flat grid into a cyclic quad mesh, anchored by four points located at the midpoint of each boundary contour line, resulting in the shape of a cross-vault (Fig. 35). Figure 36 shows the corresponding pattern of circle packing along the mesh vertices which will be used to model a foldable double layer scissor grid.

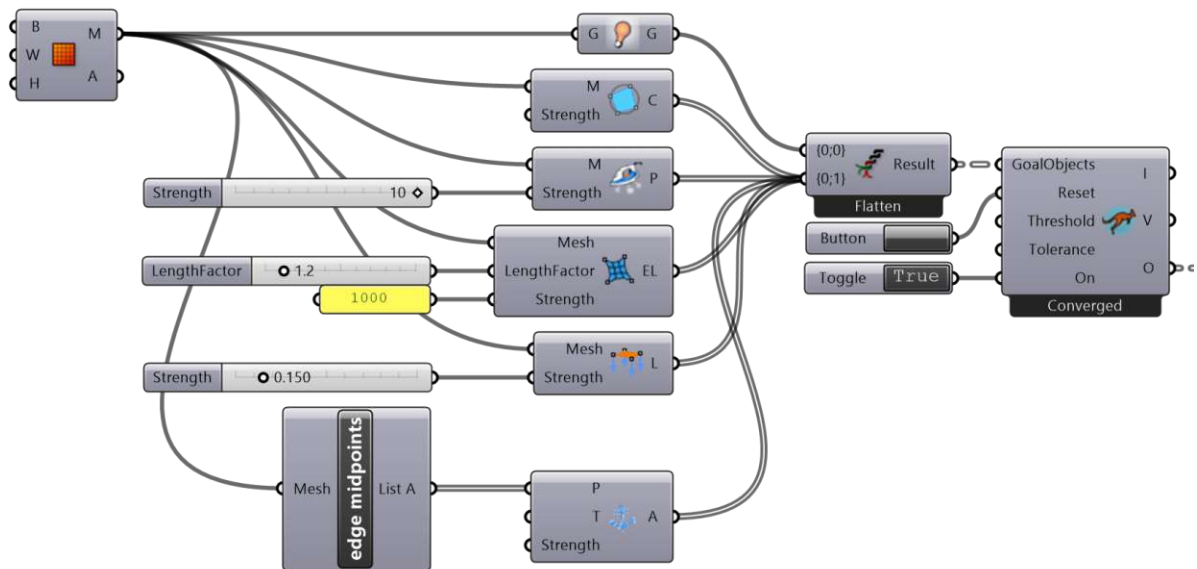


Figure 34: GH Definition for a mesh relaxation into a cyclic quad.

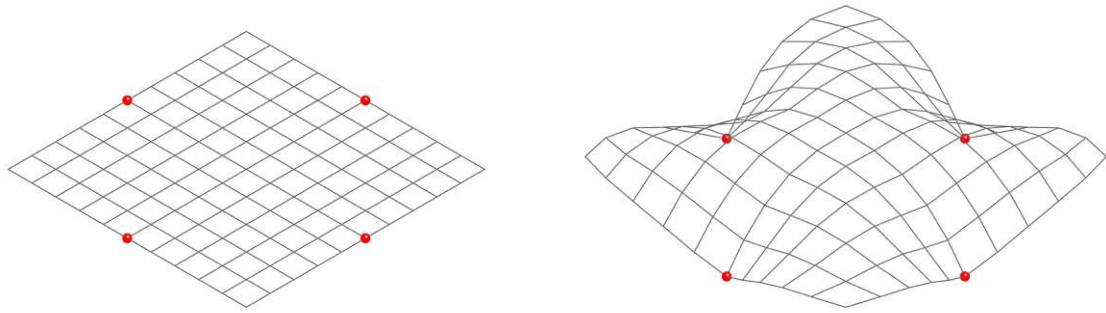
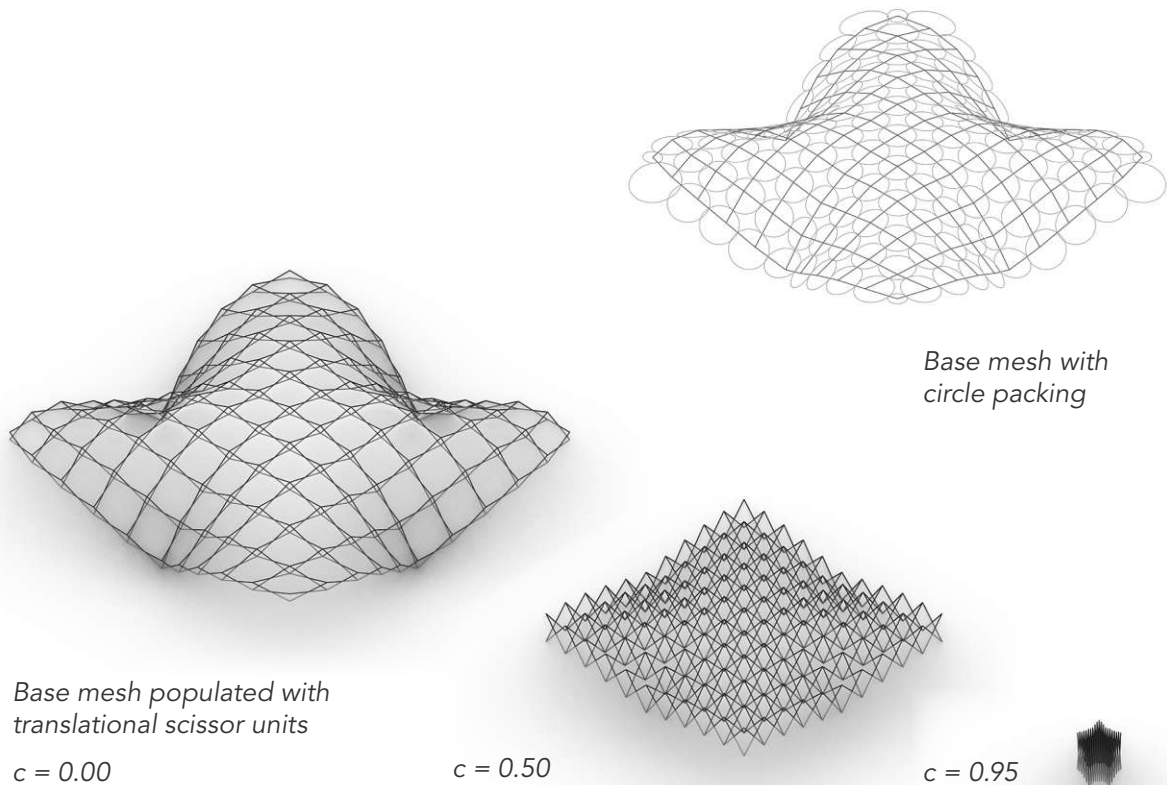


Figure 35: Mesh relaxation of a flat grid with four anchor points into a cyclic quad mesh. Illustration of resulting cross-vault geometry.

CYCLIC QUAD CROSS-VAULT					
unit type	thickness [m]	scissor bar quantity [n]	scissor bar length [m]	BB dim. c=0 [m]	BB dim. c=0.95 [m]
curved-translational	0.50	440	min. 2.03	L = 23.19	L = 1.70
			max. 2.81	H = 5.91	H = 3.55

Table 8: Model specifications - cyclic quad cross-vault.



Base mesh populated with translational scissor units

$c = 0.00$

$c = 0.50$

$c = 0.95$

Figure 36: Translational scissor grid based on cyclic quad mesh relaxation in the shape of a cross-vault. Three stages of deployment.

The pattern of circles corresponding with the vertices of the resulting mesh topology is not perfectly tangential, however, when populating the base grid with curved-translational scissor units, the simulation of deployment displays a smooth, stress-free transformation between the different stages, as illustrated in Figure 36. Translational scissor units can be applied to a wide variety of shapes, while the design issues are reduced to a set of two-dimensional problems, as all the upper and lower endpoints lie on parallel unit lines.

3.6. Discussion

For a circle packing to be converted into a deployable scissor grid, the lines going perpendicularly through the centers of each pair of tangential circles must be coplanar, as they will form the unit lines of a scissor unit (Roovers & De Temmerman 2015). This is automatically satisfied for planar and spherical grids, but not for other surfaces. The complexity of this constraint makes digital design tools essential for efficiently and intuitively solving the geometric challenges of designing these grids while also allowing for interactive adjustment of the design. Translational units eliminate this problem because their unit lines are by definition parallel.

In combination with a cyclic quadrilateral mesh relaxation as a form-finding tool, translational units offer a designer more control over a wider variety of possible grid configurations and thereby produce a more versatile catalog of possible shapes than polar scissor units.

Because of this observation, this design method will be explored further in the following chapters, where the proposed cross-vault geometry will be further refined.

4. RESULTS

4.1. Introduction

The form-finding method developed in the last chapter, where the base shape for modeling geometrically compatible scissor grids, composed of translational units, is generated by mesh relaxation with the topology of a cyclic quad, will be applied to generate several case studies for further analysis in this chapter. This entails the modeling of a detailed structural model, fulfilling the mechanical conditions of a scissor structure, used for an FE-analysis in Karamba3d and the deployment simulation in Kangaroo2.

Detail modeling requires consideration of the cross-section dimensions of the scissor bars and the resulting offset distance necessary to avoid collisions. It also includes modeling the hinge and node axes and defining them as the revolute joints. The end joints of the scissor bars will be designed in form of lugs connecting to the nodes and will be detailed later on along with the node connectors themselves (Fig. 37). In addition, because translational scissor grids have the characteristic of a foldable mechanism, making the transformation completely stress-free, the structure will need additional bracing measures, when it's completely deployed, to restrict the deformation of the fully installed structure. This is implemented by adding vertical members in form of telescopic rods to connect the upper and lower layer of nodes, as well as tensioning members in the form of steel cables.

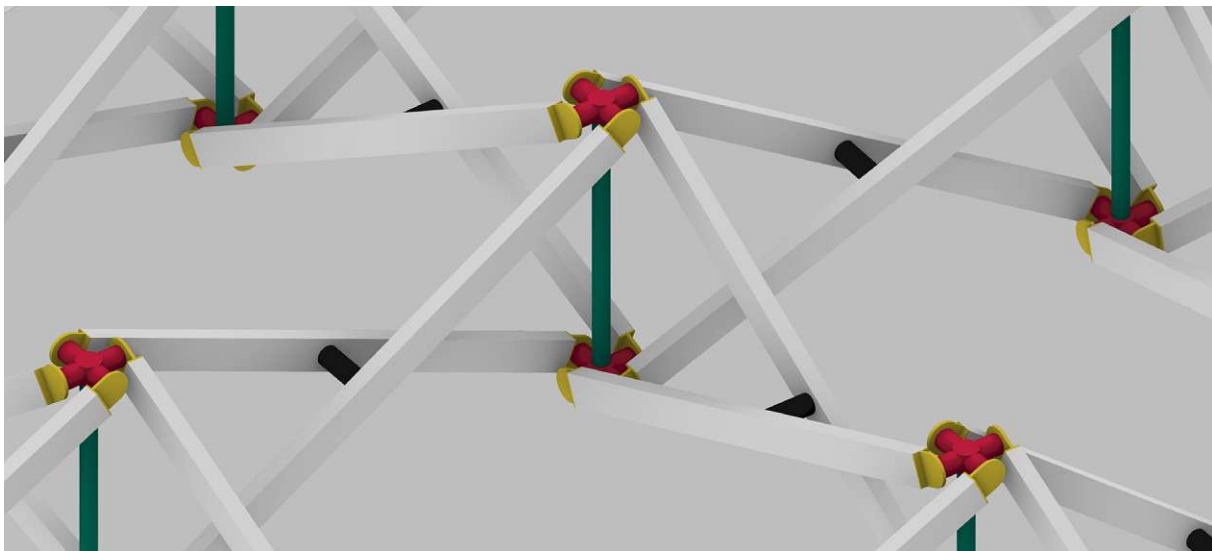


Figure 37: Detailed 3D model including scissor bars with end-lugs, hinges, nodes, and vertical bracing rods.

Following structural analysis and optimization, the detailed model with determined cross-section dimensions and node diameter will be used for a simulation of the deployment process to monitor the size when completely contracted, thereby gaining insight into its volume expansion ratio and transportation size (Fig. 38).

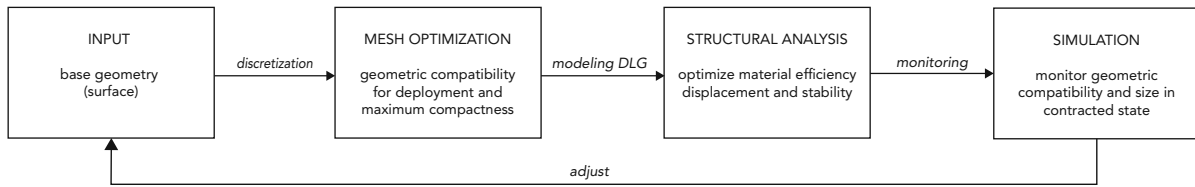


Figure 38: Form-finding, optimization, and simulation workflow.

4.2. Structural analysis and deployment simulation

In the following section the results of the structural analysis and optimization measures, done in Karamba 3d, are presented. This is followed by a documentation of the deployment simulation of a given configuration, to gain insight into the deployment factor, which marks how far a structure can be contracted before colliding. At the point of maximum contraction, the size of the structure is measured, which is used to determine the volume expansion ratio, describing the difference in size between a structure's most extreme deployment states.

Analysis, optimization, and simulation are performed on three case studies. These case studies are two cross-vault configurations and a hyperbolic barrel-vault.

4.2.1. Material

The material used for the building members in the structural model is high performance aluminum AW-7020/T6 with a yield strength of 280 N/mm². For additional tensile elements in form of cables, which help limit displacement, the material is steel S355 with a yield strength of 355 N/mm².

4.2.2. Load Cases

Two load cases (LC) are applied to each case study. LC 0 is composed of a surface load of 1 kN/m² applied over the entire area of the structure. LC 1 is composed of an asymmetric surface load of 1 kN/m², acting on one half of the structure. Both load cases include a gravity load and an initial strain load on the steel cables of 0.5 mm/m.

LC 0 is used for optimization measures on the number of vertical bracing members and on the cross-section dimension of the scissor bars. LC 1 is meant to evaluate the structure under a variable load.

4.2.3. Optimization

Optimization steps include a bi-directional evolutionary structural optimization (BESO) on the number of vertical bracing members. The BESO method is a finite element based topology optimization method, where inefficient material is iteratively removed from a structure while efficient material is simultaneously added. This is followed by a cross-section optimization assigning the most appropriate wall thickness to the scissor bars, taking into account the load bearing capacity while limiting the maximum utilization of the structure. Both optimization steps are performed under LC 0.

The intention of these optimization steps, is to achieve high material efficiency and weight reduction, thereby limiting the necessary performance level of the joining members, namely the hinges and the node connectors.

4.2.4. Documentation of results

The order in which the results will be presented for each case study in the following sections is as such:

- Description of the base grid geometry and specifications in figurative and tabular form.
- Visualization of the applied load cases on the structural model.
- Cross-section quantities and dimensions of the individual building members; weight, utilization, and displacement of the entire model. Tabular comparison of the initial setup and the results after optimization.
- Visualization of the structural analysis in Karamba 3d, showing utilization and displacement for the initial setup, the results after BESO optimization, and the results after cross-section optimization.
- Simulation of the deployment process with the determined member dimensions. Tabular summary of the results.

4.3. Cross-vault 20-12

For the first case study, the cross-vault geometry presented at the end of the last chapter is subjected to further refinement. The base grid geometry (Fig. 39) is derived by mesh relaxation into a cyclic quad. The initial quad grid used in the form-finding process has a dimension of 20 by 20 meters and a UV resolution of 12 faces in each direction. It results in a cross-vault with a bounding box side length of 21.95 m. The rise at the highest point measures 4.04 m. Support points consist of three lower nodes at the centers of the bounding contours.

4.3.1. Base grid configuration

A double-layer scissor grid with a thickness of 60 cm, composed of translational units and constructed along the edges of this base grid, results in 624 scissor bars with a member length of 1.51 to 2.30 meters, connected by 312 hinges and 338 nodes (Tab. 9). Vertical bracing rods connecting the upper and lower layer of nodes, in the form of telescopic rods consisting of three cylindrical tubes nested within each other, which will be extending or retracting during deployment are introduced for stiffness (Fig. 41). In addition to this, tensile elements in form of two steel cables are introduced, binding the elevated corners of the structure, to further limit displacement.

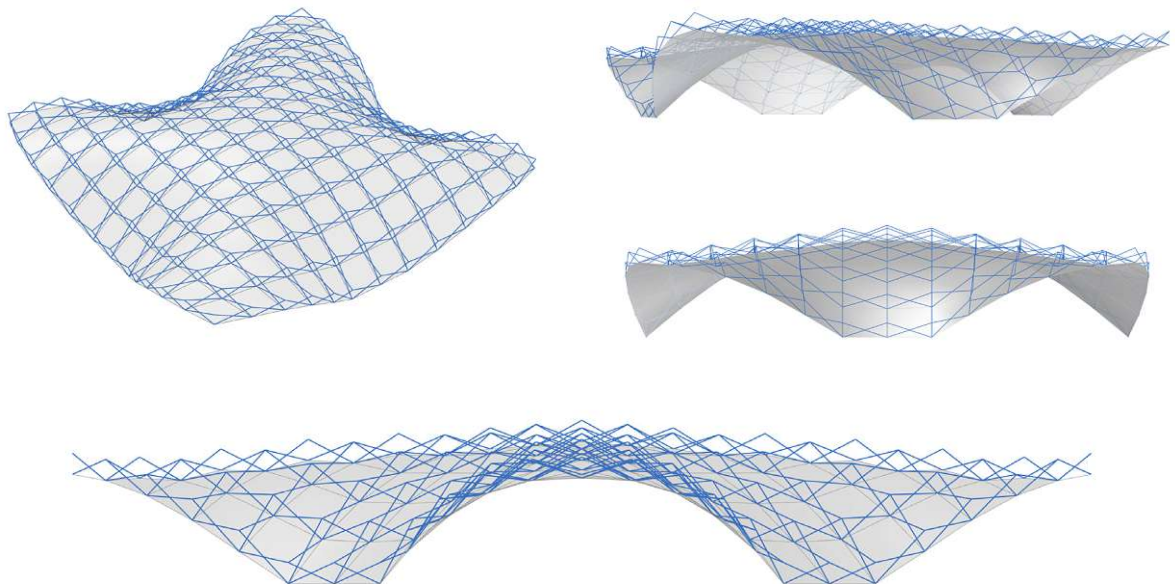


Figure 39: Line model of the base grid geometry for "Cross-vault 20-12".

CROSS-VAULT 20-12	
BB side length [m]	21.95x21.95
BB area [m ²]	481.80
BB hight [m]	4.73
interior rise [m]	4.04
UV resolution	12x12
unit type	translational
structural thickness [m]	0.60
number of scissor bars [n]	624
scissor bar member length [m]	1.51 - 2.30
number of hinges [n]	312
number of nodes [n]	338

Table 9: Model specifications for "Cross-vault 20-12".

4.3.2. Load cases

Figure 40 shows the loads acting on the structural model in LC 0 and LC 1. LC 0, consisting of a surface load of 1 kN/m², is used in two optimization steps. First, for BESO optimization on the number of vertical bracing members. The resulting pattern is shown in Figure 41. After BESO optimization the resulting model is subjected to a cross-section optimization, targeting the wall thickness of the scissor bars while limiting utilization to 80%. LC 1 consists of an asymmetric surface load of 1 kN/m² affecting half of the structure. Both load cases include gravity and an initial strain of 0.5mm/m affecting the tensioning steel cables.

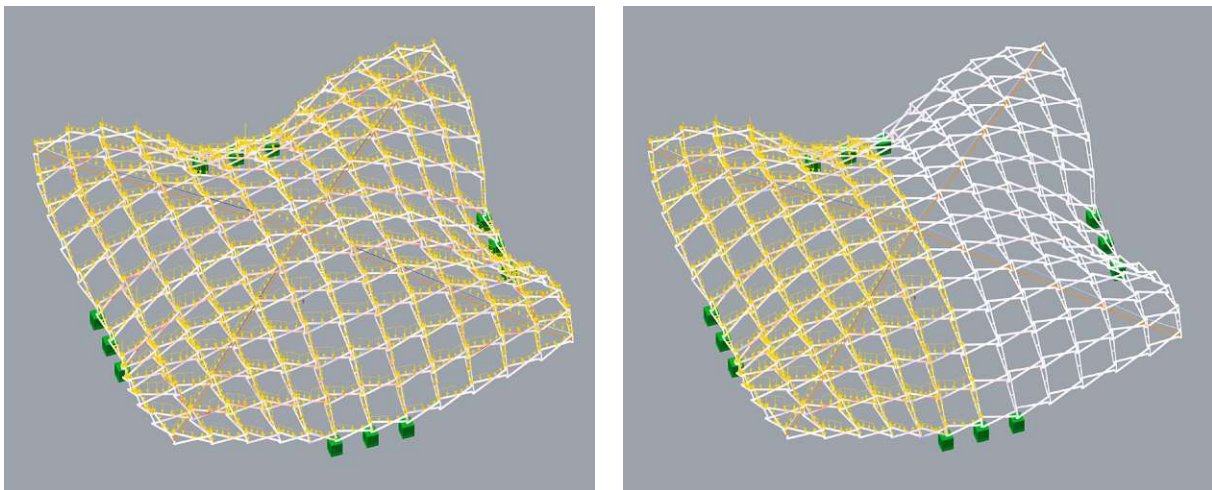


Figure 40: Loads acting on the structural model for "Cross-vault 20-12". LC 0 (left) and LC 1 (right).

4.3.3. Cross-section dimensions and optimization

CROSS-VAULT 20-12						
INDIVIDUAL MEMBERS			initial model		optimized model	
material	member	cro-sec	quantity [n]	cro-sec dim. [mm]	quantity [n]	cro-sec dim. [mm]
AW 7020 T6 ft=28kN/cm ²	scissor bars	rec.	624	100x50x6.3	599	100x50x3
		rec.			8	100x50x4.5
		rec.			5	100x50x3.6
		rec.			4	100x50x4
		rec.			4	100x50x5
		rec.			2	100x50x5.6
		rec.			1	100x50x7.1
		rec.			1	100x50x8
	vertical bracing	circ.	169	60x9	92	60x9
	hinges	circ.	312	60x6	312	60x6
nodes	circ.	338	80x1.2	338	80x1.2	
S 355	steel cables	circ.	2	20	2	20

Table 10: Cross-section table for "Cross-vault 20-12". Initial model and optimization results, affected values are highlighted in bold letters.

ENTIRE STRUCTURE		initial model	optimized model
	weight [kg]	6890	4046
LC0	utilization [%]	-55.1% - 75.3%	-70.1% - 72.5%
	displacement [cm]	5.67	15.52
LC1	utilization [%]	-69.7% - 71.6%	-79.5% - 81.7%
	displacement [cm]	8.21	18.30

Table 11: Weight, utilization and displacement values for "Cross-vault 20-12". Results for the initial and the optimized model and both load cases.

Table 10 summarizes the results of BESO and cross-section optimization on the number of vertical bracing rods and the wall thickness of the scissor bars, comparing the initial configuration to the results after optimization measures. Table 11 compares weight, utilization, and displacement values for the initial and the optimized model for LC 0 and LC 1. The documentation of these results for the initial model and each optimization step is presented for both load cases on the following pages in Figures 43 through 54.

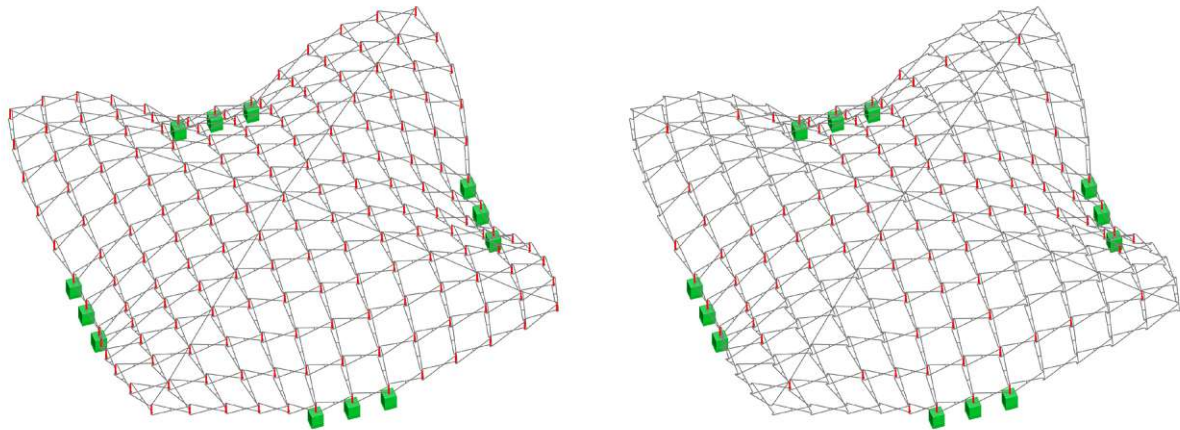


Figure 41: BESO optimization on the number of vertical bracing rods for "Cross-vault 20-12". Of 169 rods in the initial model, 92 remain, 77 are not utilized.

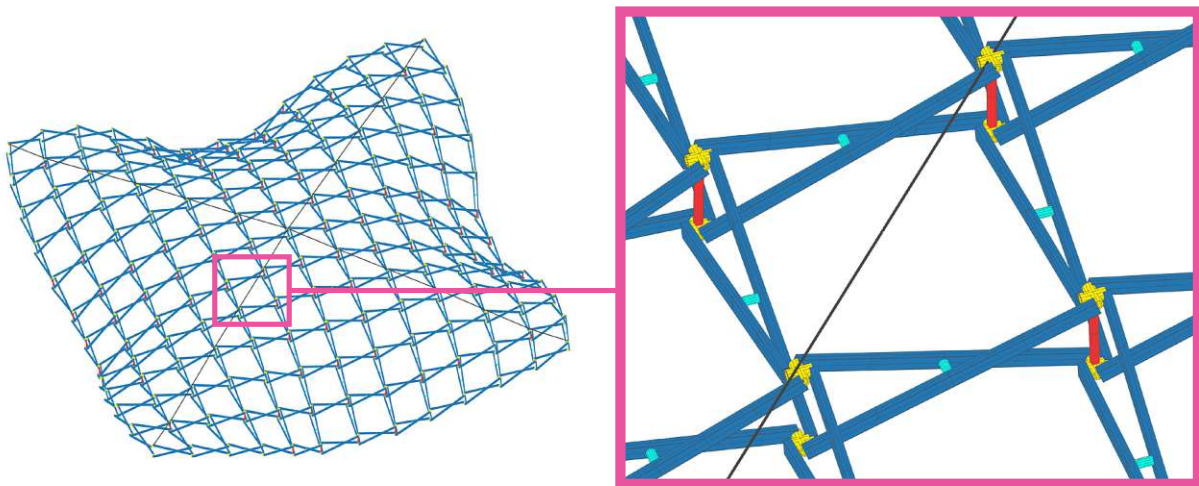
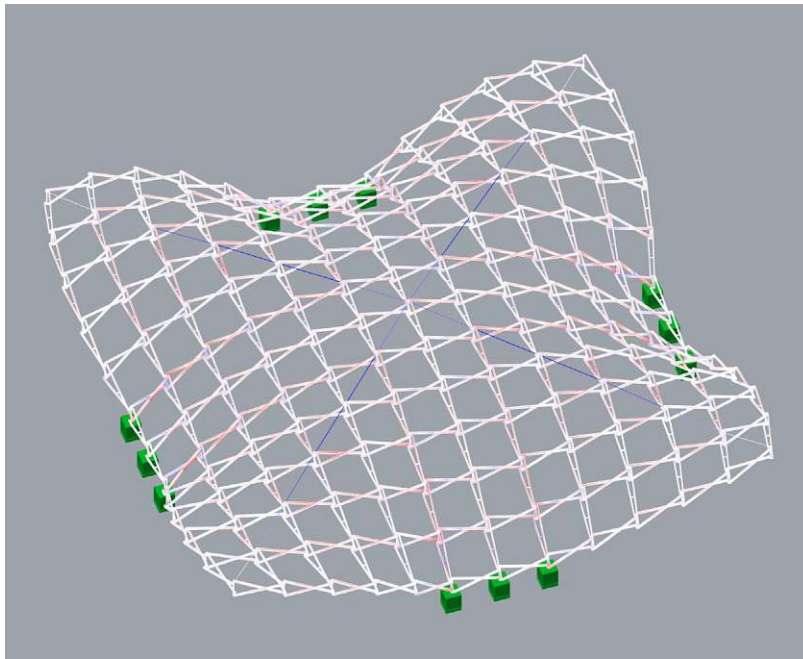


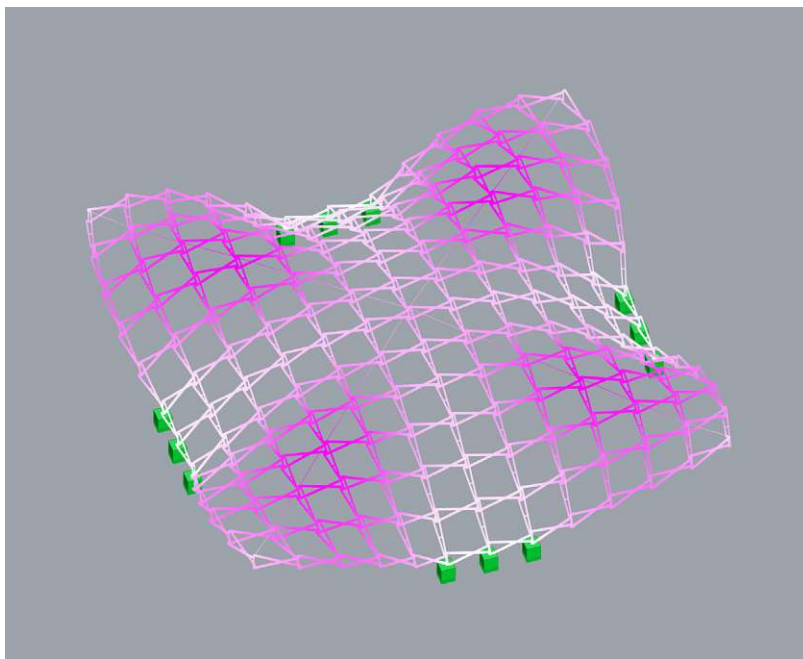
Figure 42: Color-coded cross-sections for "Cross-vault 20-12", as referenced in Table 9.

INITIAL MODEL LC 0



-55.1%
-44.1%
-33.0%
-22.0%
-11.0%
0.0%
15.1%
30.1%
45.2%
60.2%
75.3%

Figure 43: Initial model "Cross-vault 20-12" for LC0. Utilization ranges between -55.1% and 75.3%.



0.00e+00
5.67e-01
1.13e+00
1.70e+00
2.27e+00
2.83e+00
3.40e+00
3.97e+00
4.53e+00
5.10e+00
5.67e+00

Figure 44: Initial model "Cross-vault 20-12" for LC0. Maximum displacement of 5.67 cm.

INITIAL MODEL LC 1

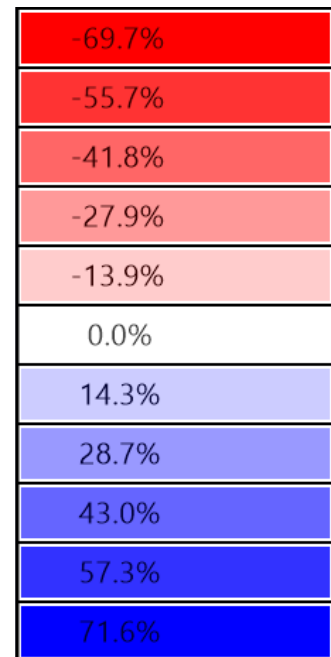
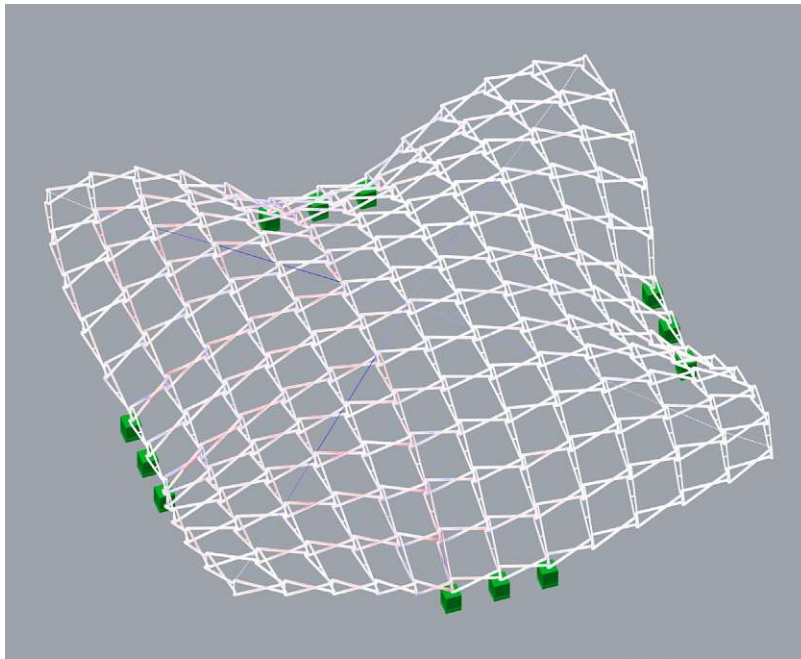


Figure 45: Initial model "Cross-vault 20-12" for LC1. Utilization ranges between -69.1% and 71.6%.

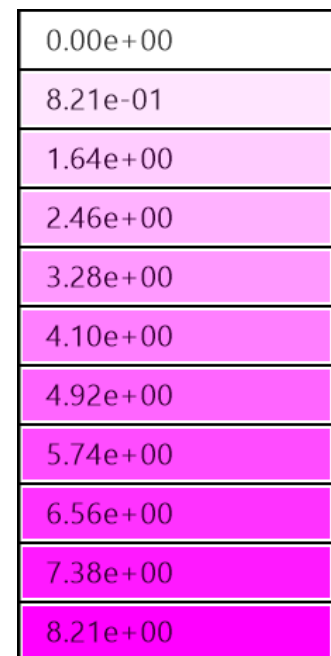
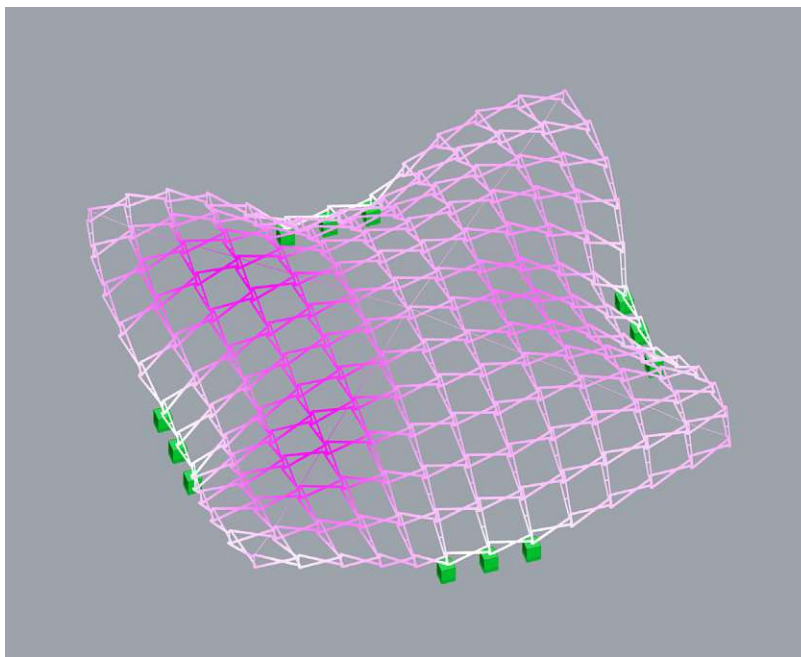


Figure 46: Initial model "Cross-vault 20-12" for LC1. Max. displacement of 8.21 cm.

BESO OPTIMIZATION LC 0

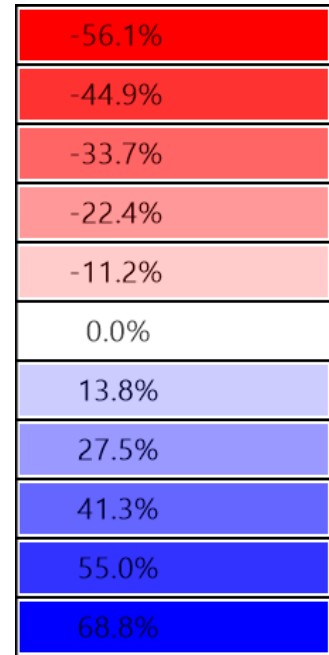
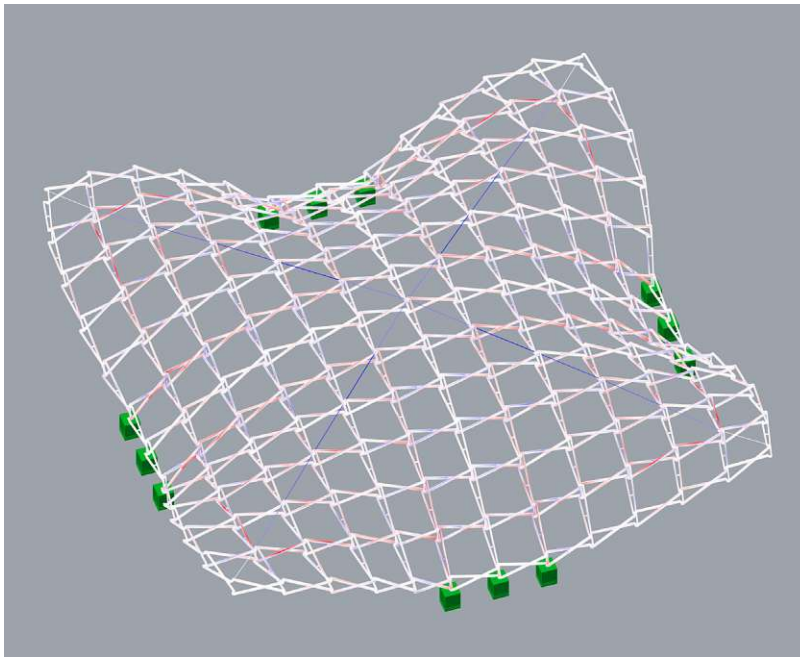


Figure 47: Utilization of "Cross-vault 20-12" for LC 0 after BESO optimization on the number of the vertical bracing members ranges between -56.1% and 68.8%.

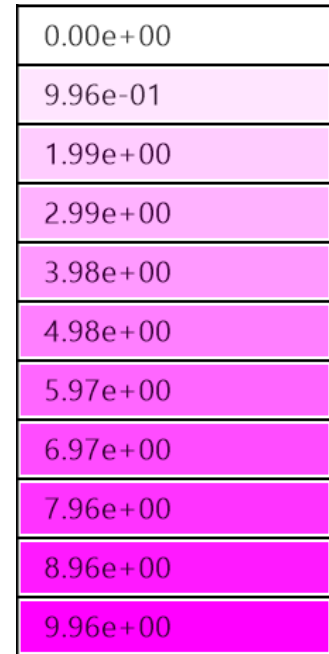
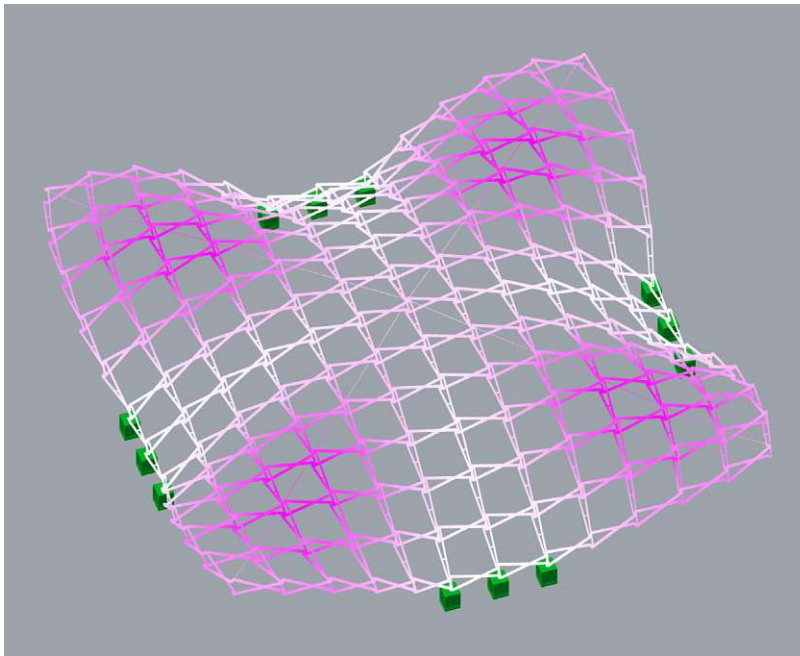


Figure 48: Displacement of "Cross-vault 20-12" for LC 0 after BESO optimization on the number of the vertical bracing members. Max. displacement of 9.96 cm.

BESO OPTIMIZATION LC 1

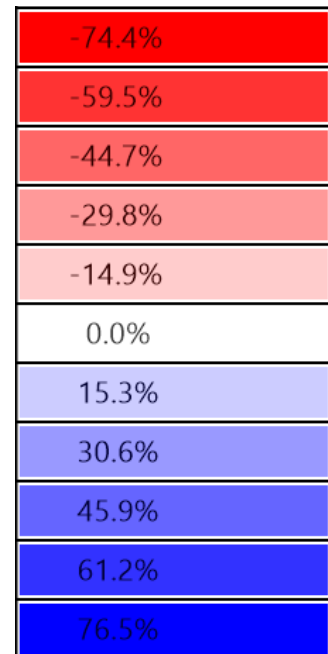
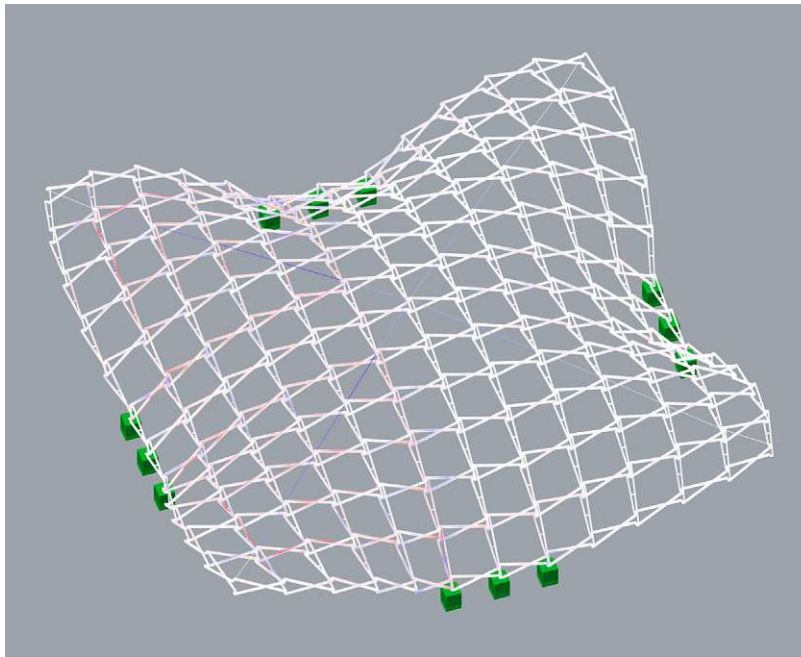


Figure 49: Utilization of "Cross-vault 20-12" for LC 1 after BESO optimization on the number of the vertical bracing members ranges between -74.4% and 76.5%.

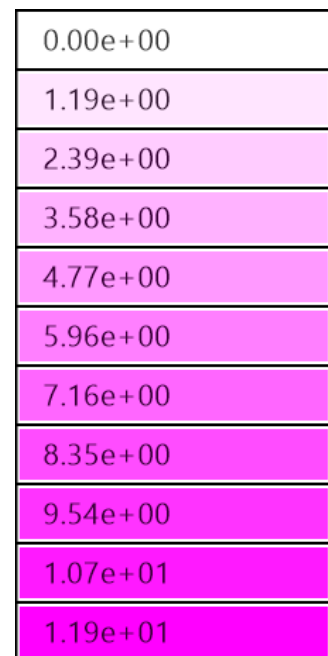
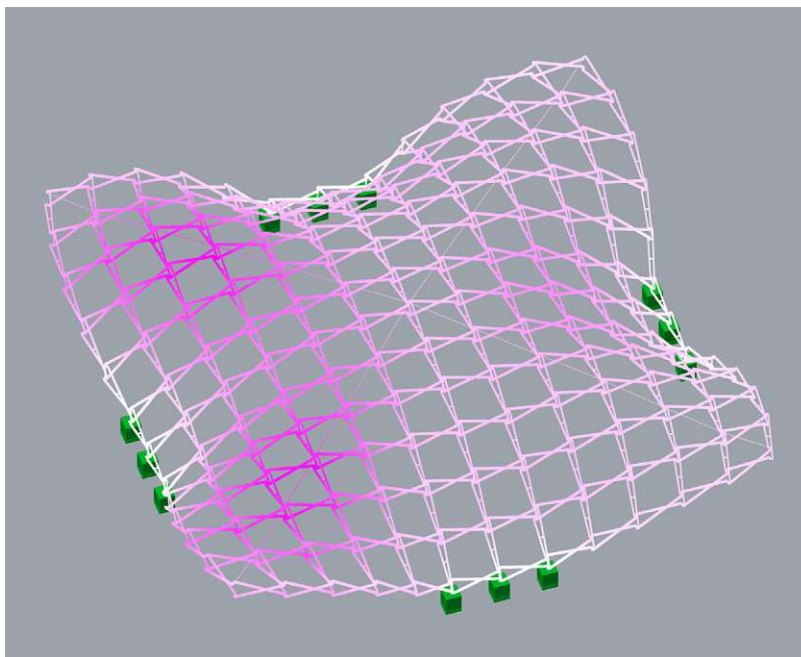


Figure 50: Displacement of "Cross-vault 20-12" for LC 1 after BESO optimization on the number of the vertical bracing members. Max. displacement of 11.9 cm.

CROSS-SECTION OPTIMIZATION LC 0

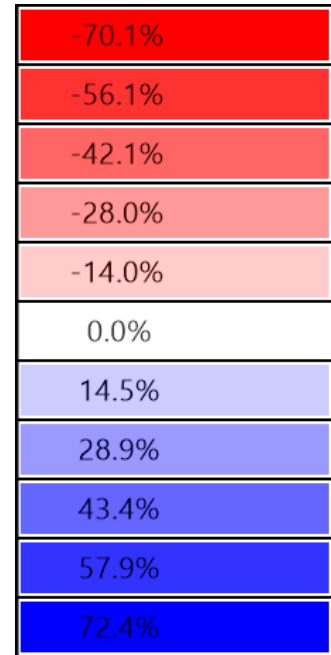
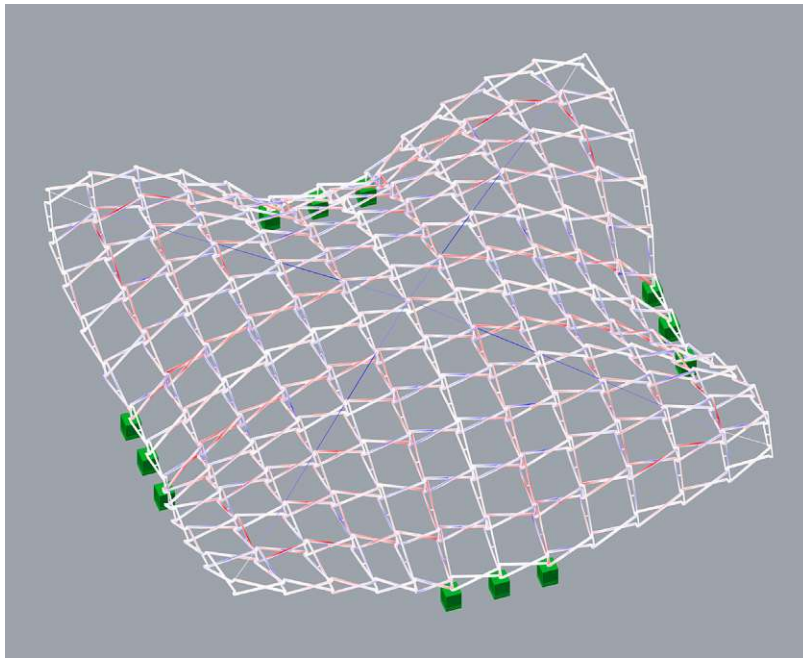


Figure 51: Utilization of "Cross-vault 20-12" for LC 0 after cross section optimization targeting the wall thickness of the scissor bars ranges between -70.1% and 72.4%.

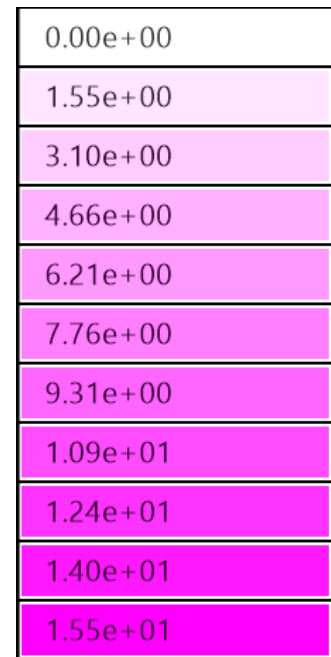
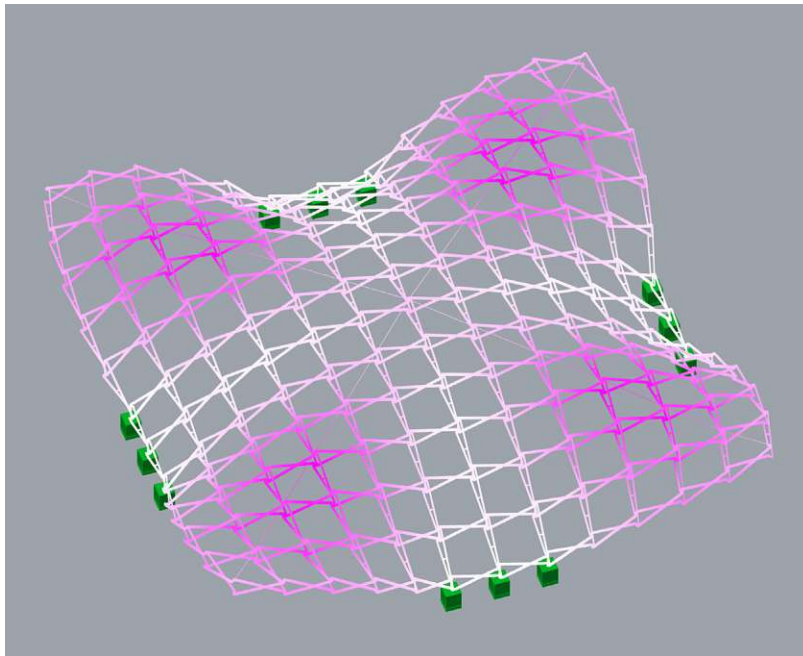


Figure 52: Displacement of "Cross-vault 20-12" for LC 0 after cross section optimization targeting the wall thickness of the scissor bars. Max. displacement of 15.5 cm.

CROSS-SECTION OPTIMIZATION LC 1

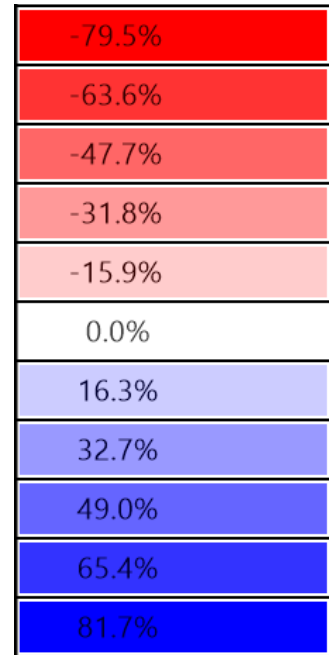
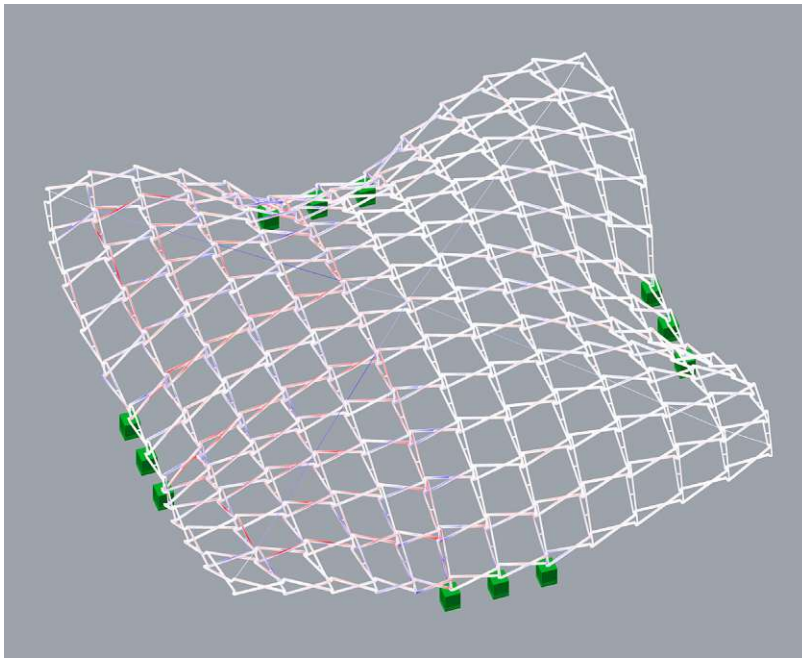


Figure 53: Utilization of "Cross-vault 20-12" for LC 1 after cross section optimization targeting the wall thickness of the scissor bars ranges between -79.5% and 81.7%.

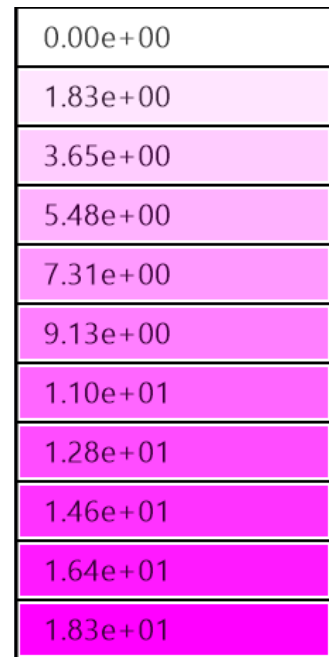
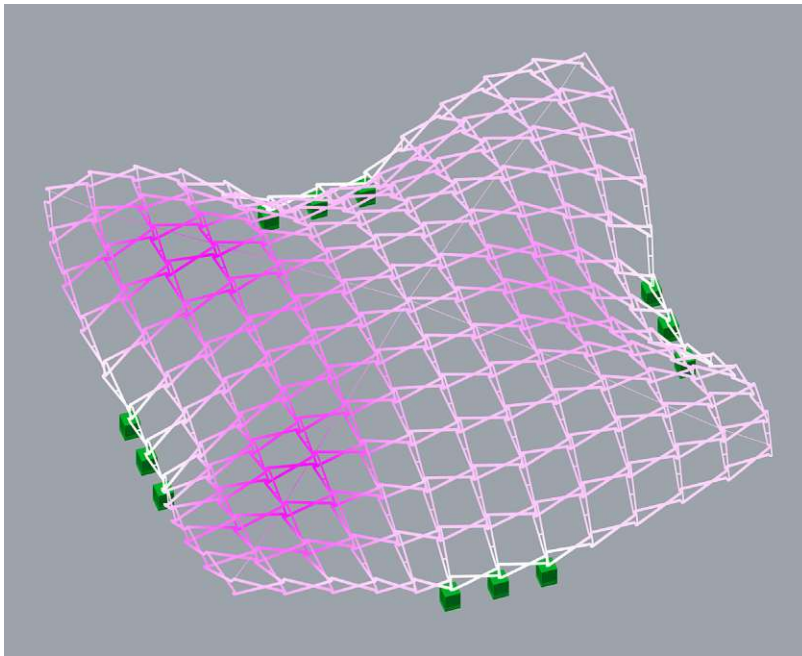


Figure 54: Displacement of "Cross-vault 20-12" for LC 1 after cross section optimization targeting the wall thickness of the scissor bars. Max. displacement is 18.3 cm.

4.3.4. Deployment simulation

CROSS-VAULT 20-12		
SIMULATION SPECIFICATIONS	deployed	contracted
deployment factor [c]	0.00	0.82
BB side length [m]	21.95	5.56
BB height [m]	4.73	3.20
vertical distance betw. nodes [m]	0.60	1.89
volume [%]	100%	4.34%

MODEL SPECIFICATIONS	structurally determined values
number of scissor bars [n]	624
scissor bar member length [m]	1.51 - 2.30
scissor bar cro-sec dimension WxH [mm]	50x100
number of nodes [n]	338
node diameter/hinge length [mm]	190

Table 12: Evaluation of the deployment simulation for "Cross-vault 20-12".

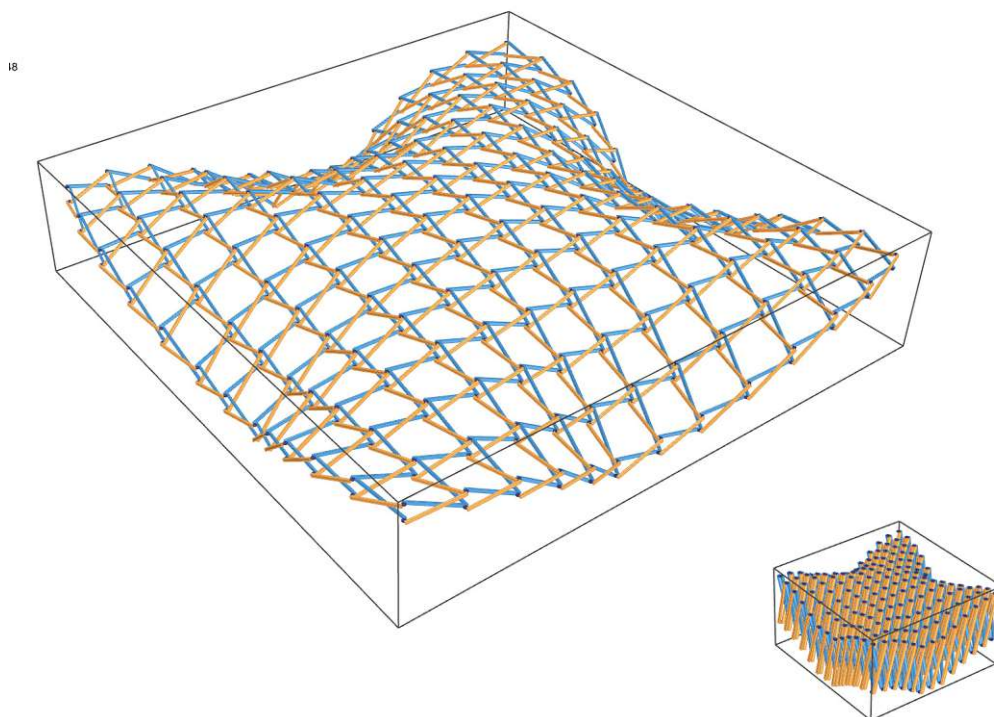


Figure 55: Deployment simulation for "Cross-vault 20-12" at two stages of deployment. Fully deployed structure (left) and maximum contraction (right).

4.3.5. Discussion

The initial structural model for “Cross-vault 20-12”, consisting of 624 scissor bars with a cross-section dimension of 50x100x6.3 mm and vertical bracing members for all 169 upper and lower node pairs, showed a utilization -69.7% to 71.6%, and a maximum displacement of 8.21 cm under an asymmetric load (LC 1).

When considering the distribution of utilization throughout the model (Fig. 43 and 45), it becomes evident that the maximum cross-section utilization is locally constricted along the symmetry axes connecting the four anchor points of the cross-vault. This observation opened the possibility of making the material distribution more efficient by optimizing the number of bracing elements and the wall thickness of the scissor bars. The resulting model shows a weight reduction of 2.8 tons. Utilization ranges between -79.5% and 81.7%, maximum displacement will however increase by almost 10 cm to 18.30 cm.

When looking at the resulting values of the deployment simulation (Fig. 55) summarized in Table 12 the structure shows an impressive volume-expansion ratio. Collisions occur, limiting further contraction, at a deployment factor of $c=0.82$, when the bounding box side length is reduced from 21.95 m to 5.56 m. This results in an area over 480 m² being reduced to 30 m². In relation to volume the structure in its contracted state takes up only 4.34% of the space, it occupies when completely deployed.

To evaluate, whether a smaller size model, with smaller node diameter and scissor bar cross-sections, can help limit the maximum displacement, and how this will affect the deployment properties of such a cross-vault structure a second iteration is presented next.

4.4. Cross-vault 14-11

For the second case study, the previous cross-vault geometry is adjusted to cover a smaller base area with reduced member dimensions, in the interest of producing a model with better performance in relation to weight, displacement, and transport size.

4.4.1. Base grid geometry

The base grid geometry is presented in Figure 56. The bounding box of the base grid covers an area of 250 m² and has a UV resolution of 11 units in each direction. The rise at the highest point of the vault measures 3.40 m, which represents a steeper curve when compared to the previous model. Support points consist of two lower nodes at the center of each bounding contour line.

The scissor structure is composed of translational units with a structural thickness of 60 cm, resulting in 528 scissor bars with a member length of 1.10 to 1.98 meters, connected by 264 hinges and 288 nodes (Tab. 13).

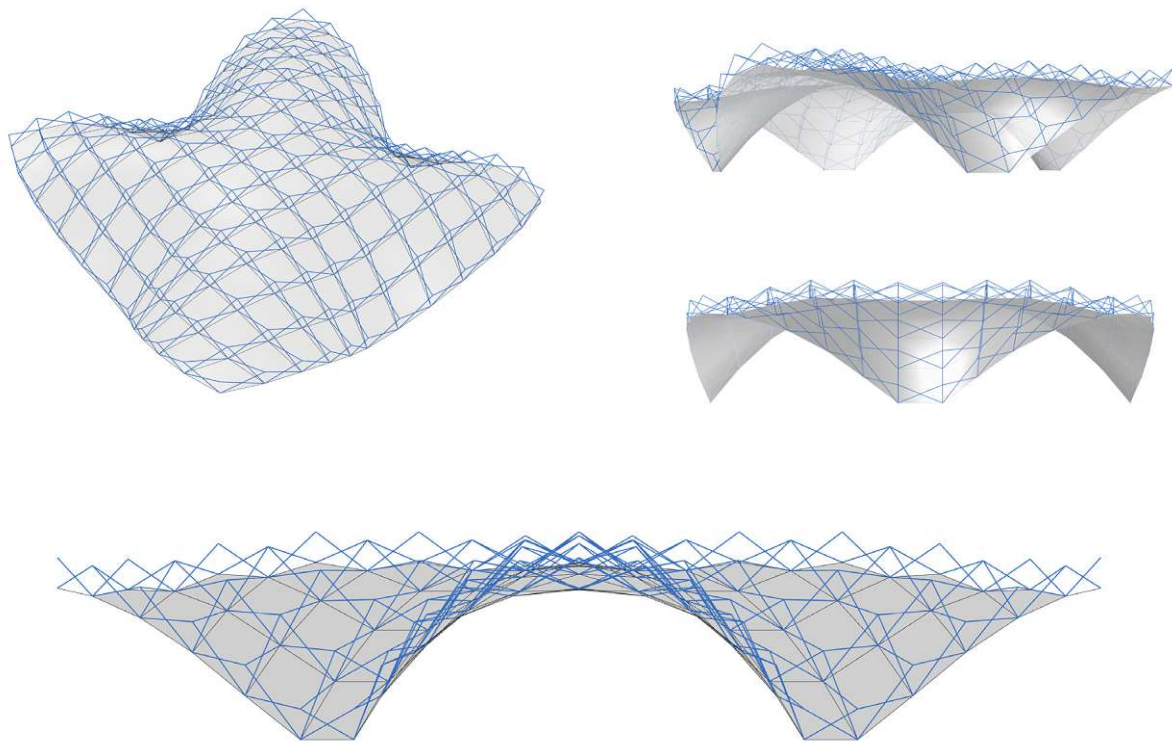


Figure 56: Line model of the base grid geometry for Cross-vault 14-11.

CROSS-VAULT 14-11	
BB side length [m]	15.80x15.80
BB area [m ²]	249.64
BB hight [m]	4.15
interior rise [m]	3.40
UV resolution	11
unit type	translational
structural thickness [m]	0.60
number of scissor bars [n]	528
scissor bar member length [m]	1.10 - 1.98
number of hinges [n]	264
number of nodes [n]	288

Table 13: Model specifications for "Cross-vault 14-11".

4.4.2. Load cases

Figure 57 shows the loads acting on the structural model for LC 0 and LC 1. The resulting pattern of vertical bracing rods before and after BESO optimization is shown in Figure 58. The structure is also subjected to a cross-section optimization, affecting the wall thickness of the scissor bars.

Amounts and dimensions for all building members, along with utilization and displacement values of the initial model and the optimized model for LC 0 and LC 1 are presented in the next section.

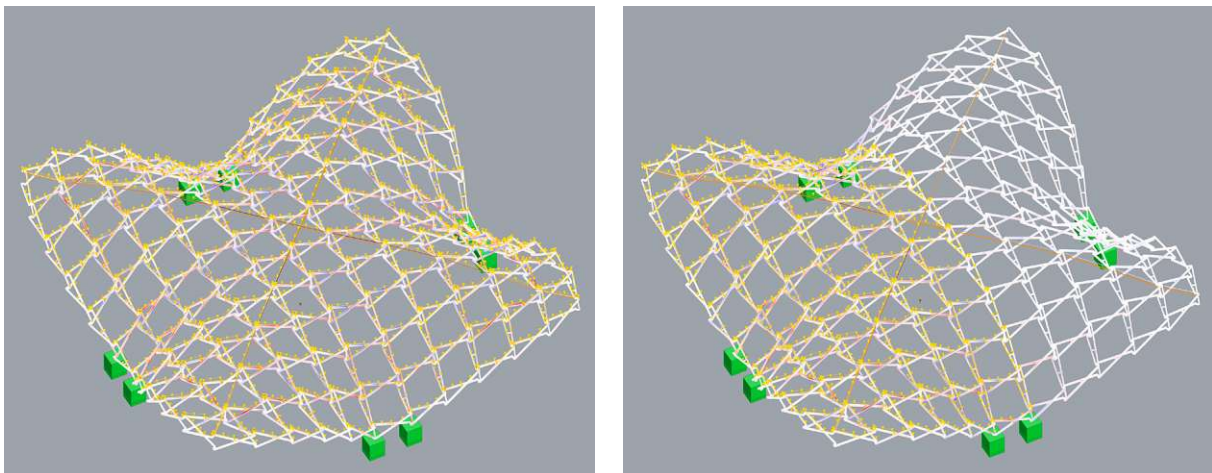


Figure 57: Loads acting on the structural model for "Cross-vault 14-11". LC 0 (left) and LC 1 (right).

4.4.3. Cross-section dimensions and optimization

CROSS-VAULT 14-11						
INDIVIDUAL MEMBERS			initial model		optimized model	
material	member	cro-sec	quantity [n]	cro-sec dim. [mm]	quantity [n]	cro-sec dim. [mm]
AW 7020 T6 ft=28kN/cm ²	scissor-bars	rec.	528	80x40x5	520	80x40x2.9
		rec.			3	80x40x4.0
		rec.			2	80x40x7.1
		rec.			2	80x40x3.6
		rec.			1	80x40x4.5
	vertical bracing	circ.	144	60x6	57	60x6
	hinge sleeve	circ.	264	60x4	264	60x2
	node sleeves	circ.	288	60x10	288	60x10
S 355	steel cables	circ.	2	14	2	14

Table 14: Cross-section table for "Cross-vault 14-11". Initial model and optimization results, affected values are highlighted in bold letters.

ENTIRE STRUCTURE		initial model	optimized model
	weight [kg]	3233	2151
LC0	utilization [%]	-45.1% - 79.3%	-64.4% - 80.0%
	displacement [cm]	3.98	10.21
LC1	utilization [%]	-56.5% - 60.9%	-70.5% - 71.7%
	displacement [cm]	5.09	12.21

Table 15: Weight, utilization and displacement values for "Cross-vault 14-11". Results for the initial and the optimized model and both load cases.

Table 14 summarizes the results of BESO and cross-section optimization in comparison to the initial configuration. Overall the use of material for this model is more efficient than for the previous iteration. The cross-section dimension of the scissor bars is more slender, which results in a smaller diameter for the nodes and a shorter length of the hinges.

Table 15 compares the weight, utilization, and displacement values of the initial and the optimized model for LC 0 and LC 1. The documentation of these results for the initial model and each optimization step is presented for both load cases on the following pages in Figures 60 through 71.

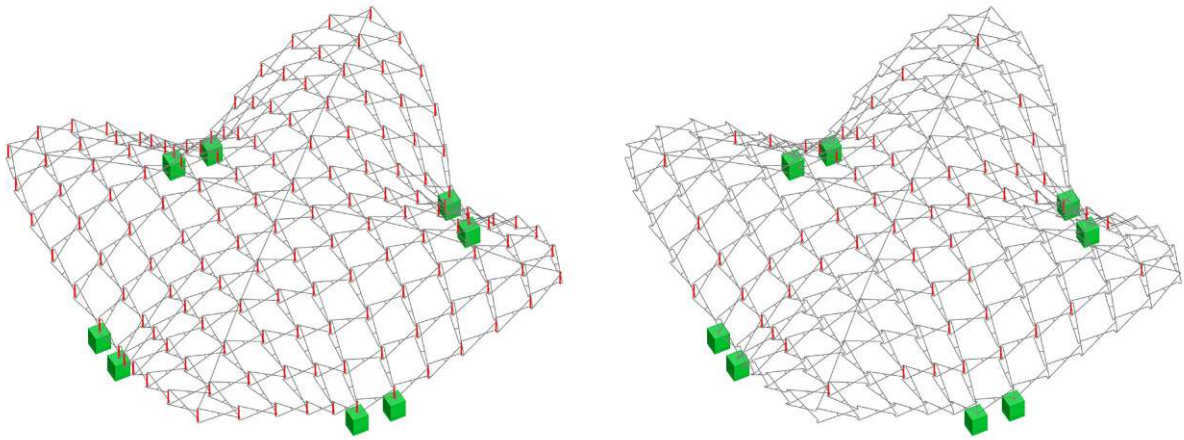


Figure 58: BESO optimization on the number of vertical bracing rods for "Cross-vault 14-11". Of 144 rods in the initial model (left), 57 remain, 87 are not utilized (right).

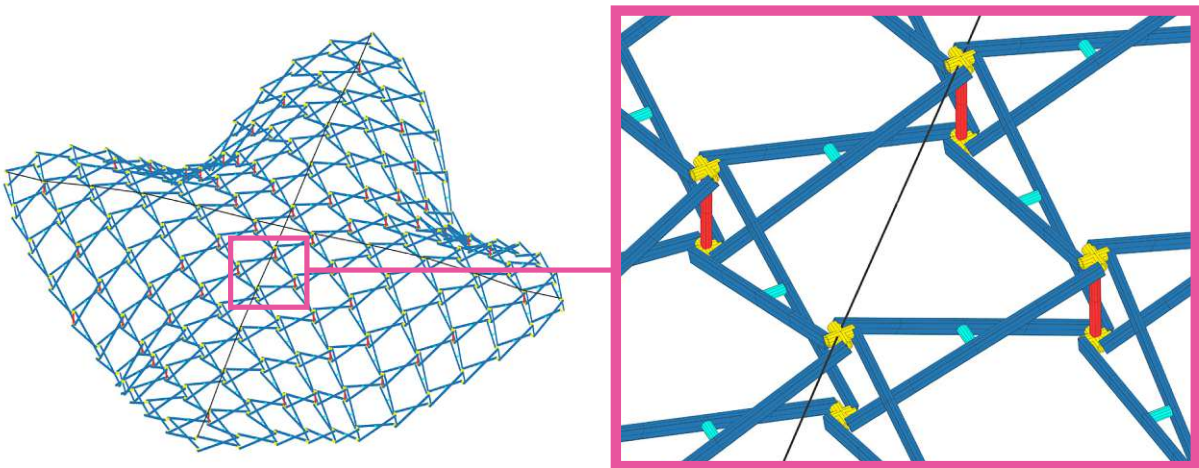


Figure 59: Color-coded cross-sections for "Cross-vault 14-11" as referenced in Table 13.

INITIAL MODEL LC 0

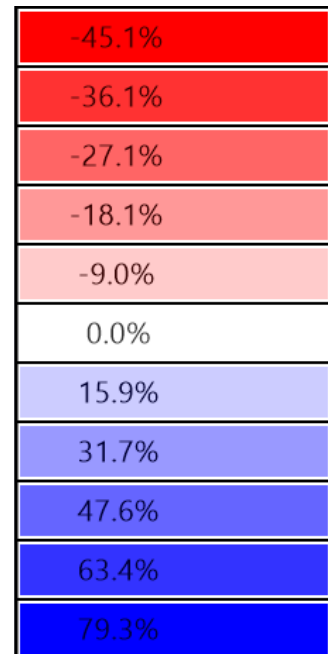
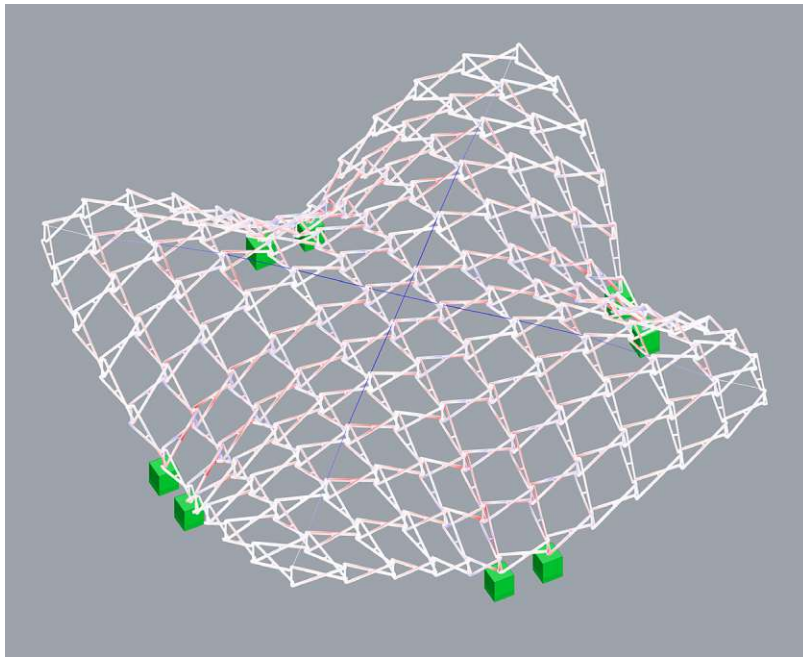


Figure 60: Initial model "Cross-vault 14-11" for LC 0. Utilization ranges between -45.1% and 79.3%.

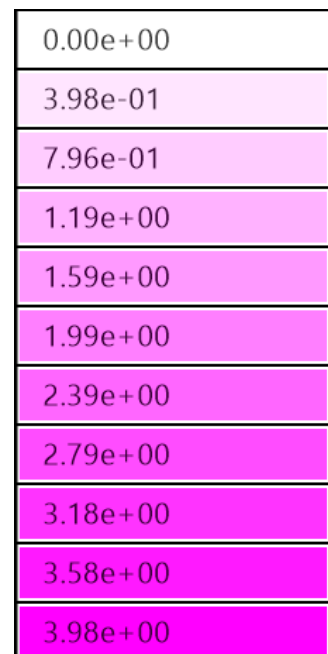
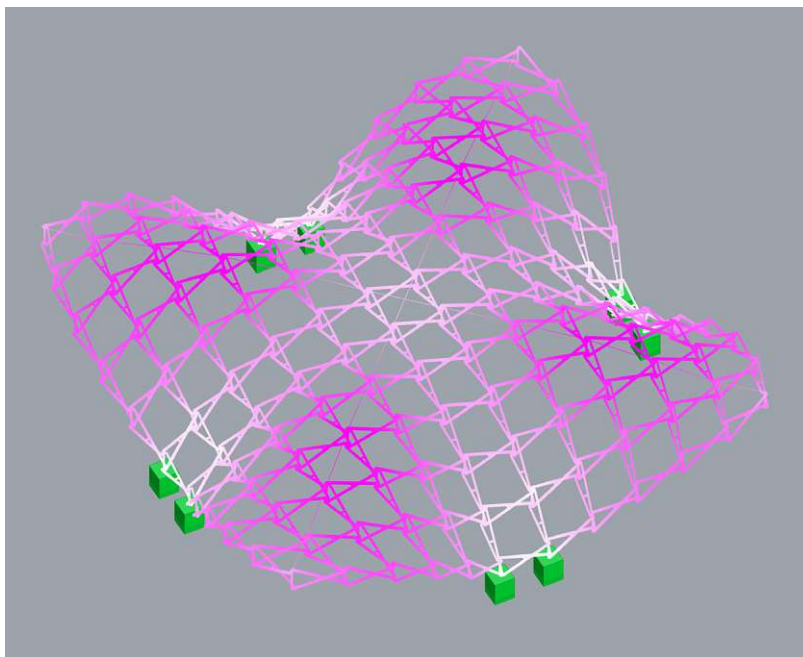


Figure 61: Initial model "Cross-vault 14-11" for LC 0. Maximum displacement of 3.98 cm.

INITIAL MODEL LC 1

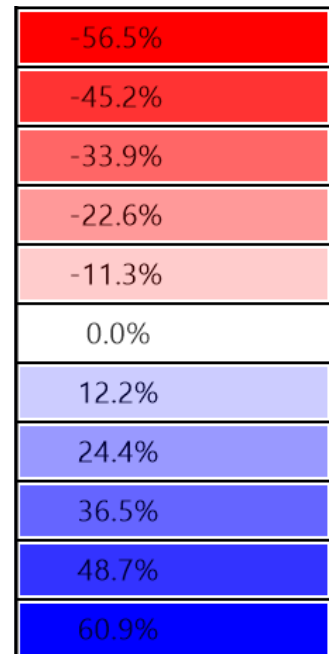
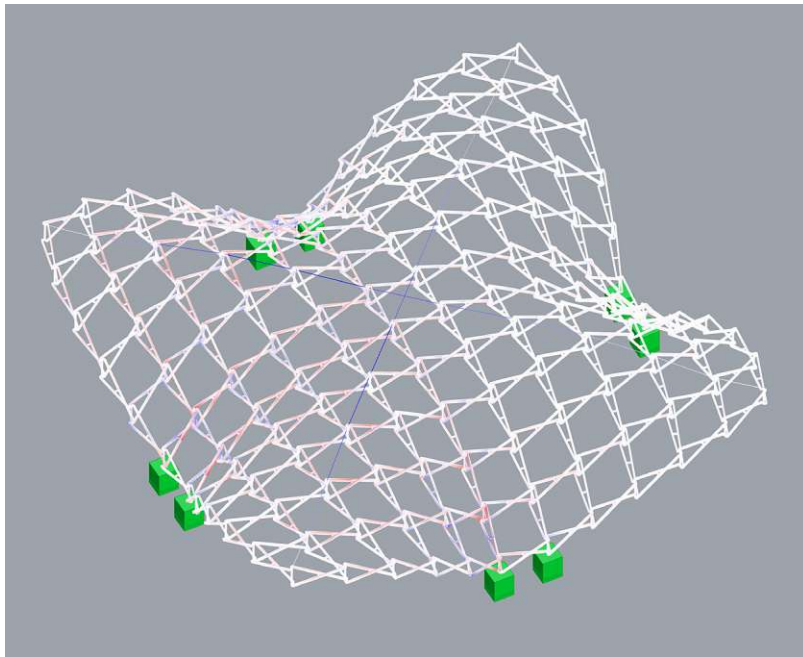


Figure 62: Initial model "Cross-vault 14-11" for LC 1. Utilization ranges between -56.5% and 60.9%.

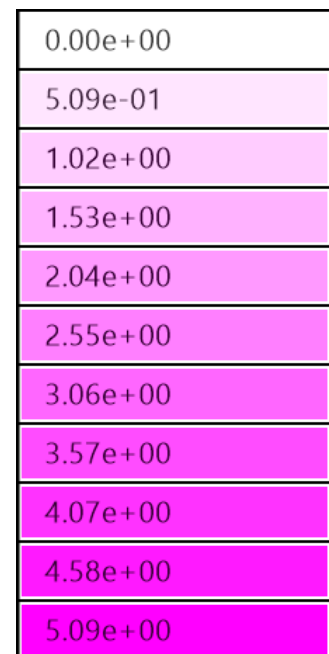
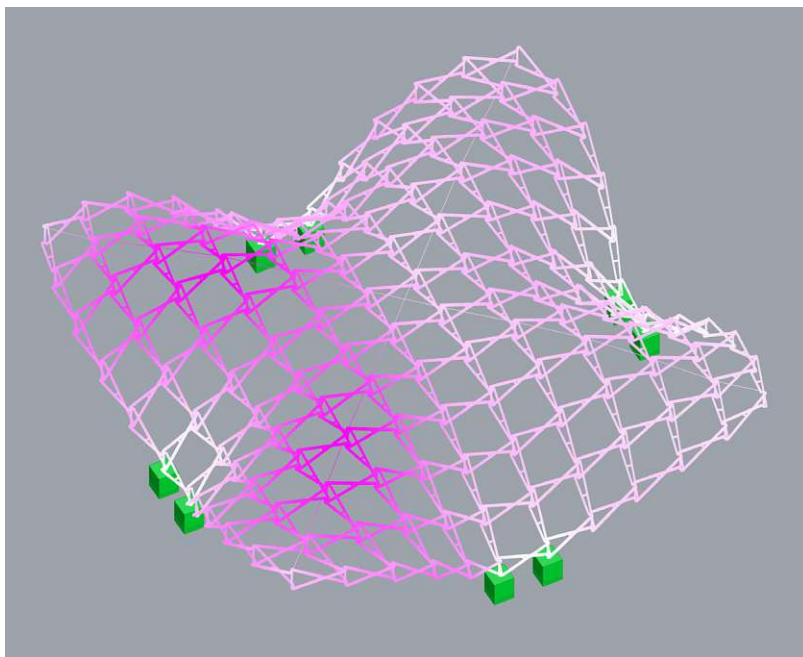


Figure 63: Initial model "Cross-vault 14-11" for LC 1. Maximum displacement of 5.09 cm.

BESO OPTIMIZATION LC 0

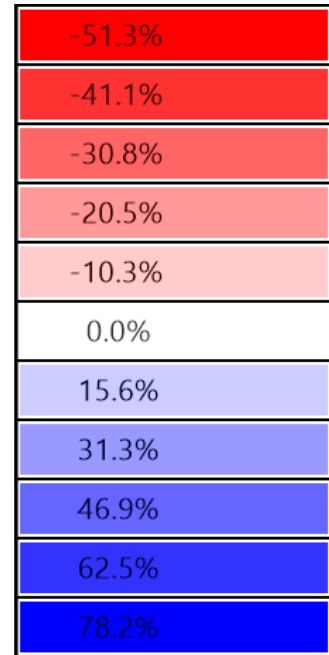
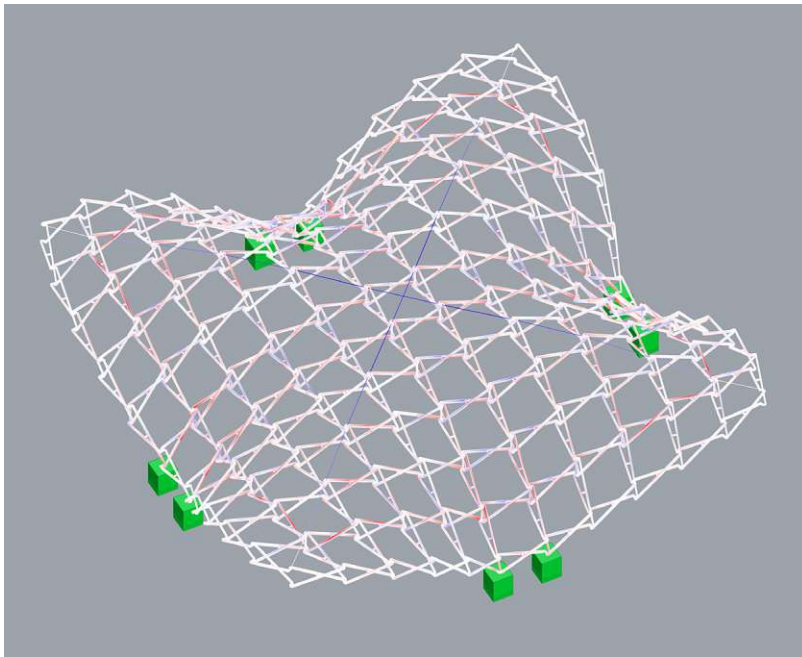


Figure 64: Utilization of "Cross vault 14-11" for LC 0 after BESO optimization on the number of the vertical bracing members, ranges between -51.3% and 78.2%.

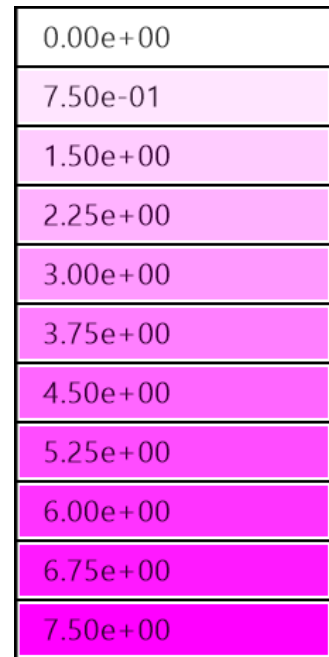
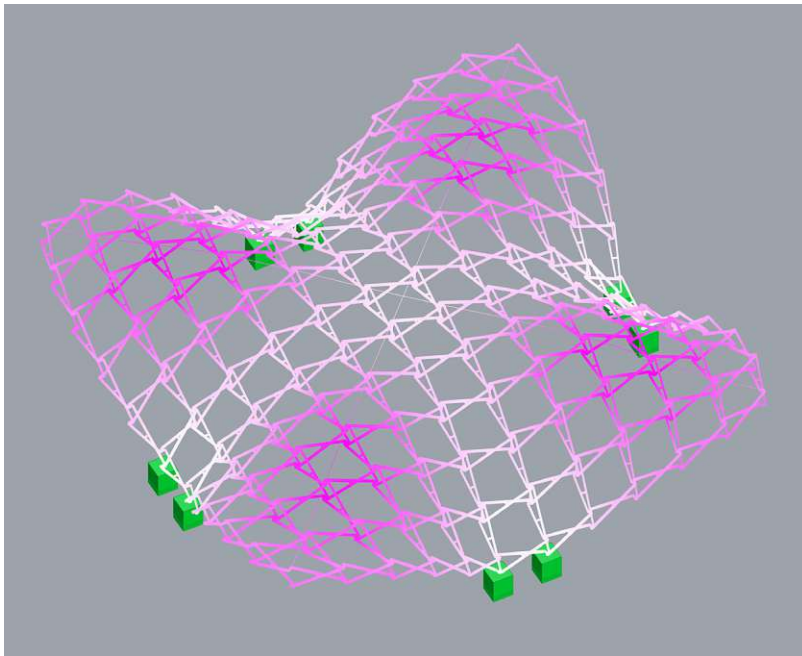


Figure 65: Displacement of "Cross vault 14-11" for LC 0 after BESO optimization on the number of vertical bracing members. Max. displacement of 7.50 cm.

BESO OPTIMIZATION LC 1

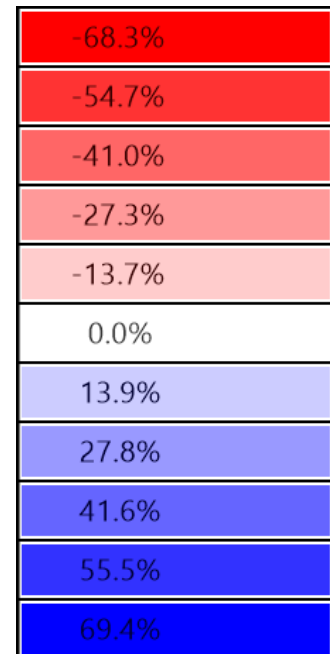
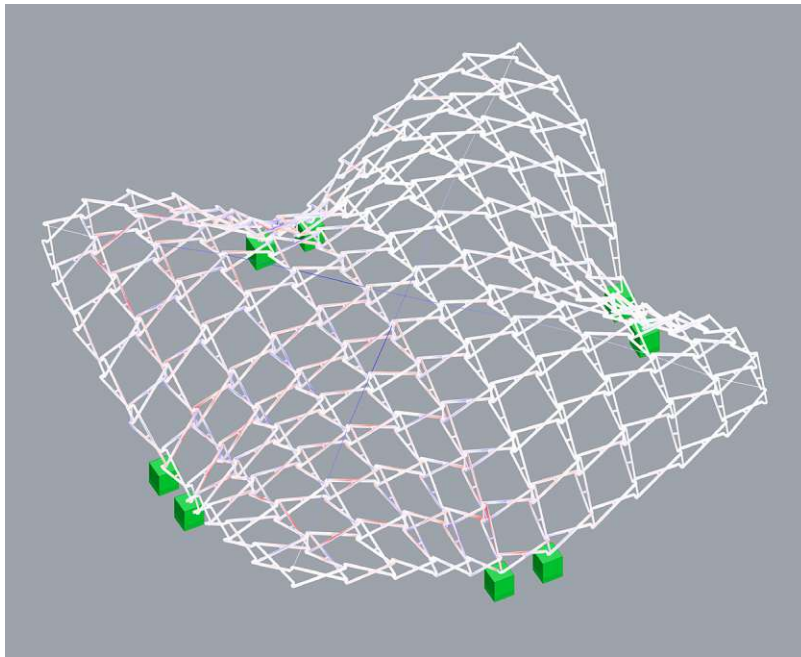


Figure 66: Utilization of "Cross vault 14-11" for LC 1 after BESO optimization on the number of the vertical bracing members, ranges between -68.3% and 69.4%.

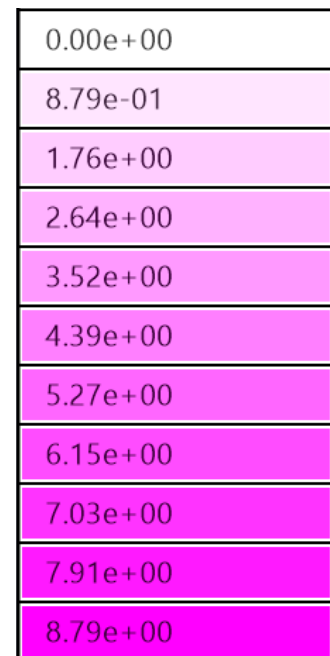
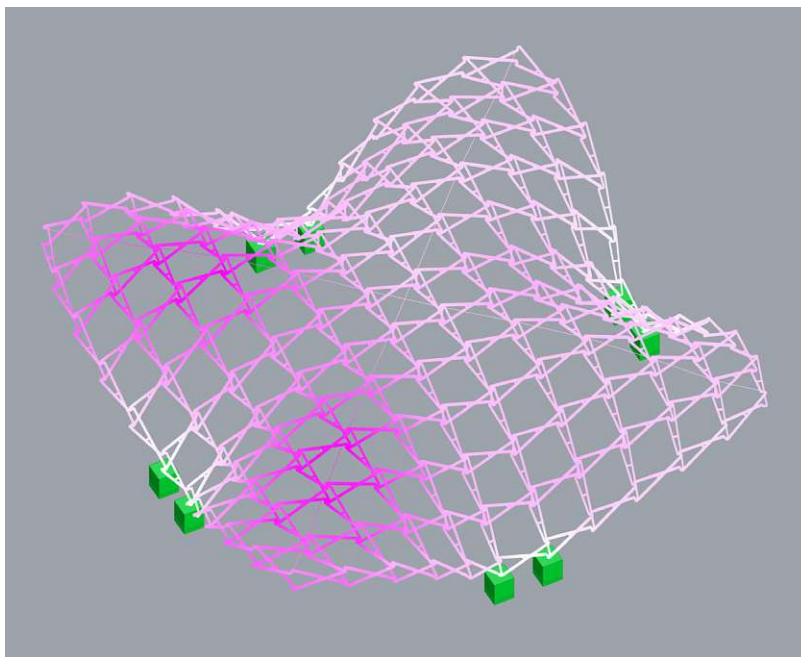


Figure 67: Displacement of "Cross vault 14-11" for LC 1 after BESO optimization on the number of vertical bracing members. Max. displacement of 8.79 cm.

CROSS-SECTION OPTIMIZATION LC 0

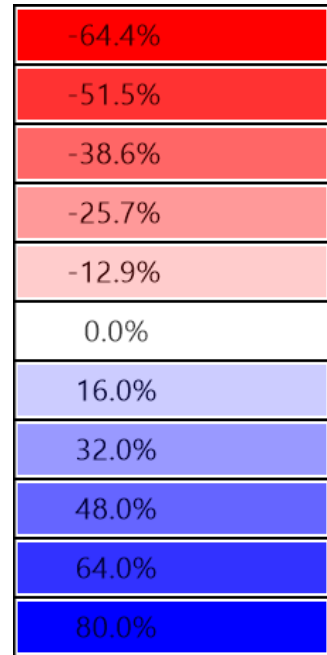
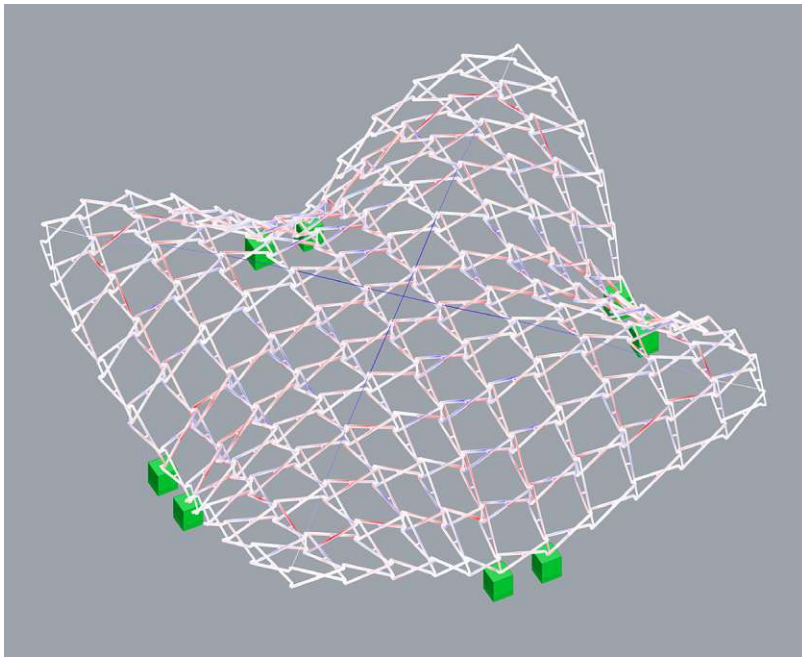


Figure 68: Utilization of "Cross vault 14-11" for LC 0 after cross-section optimization targeting the wall thickness of the scissor bars ranges between -64.4% and 80%.

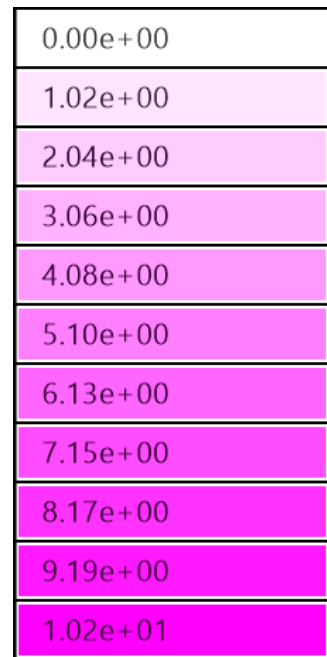
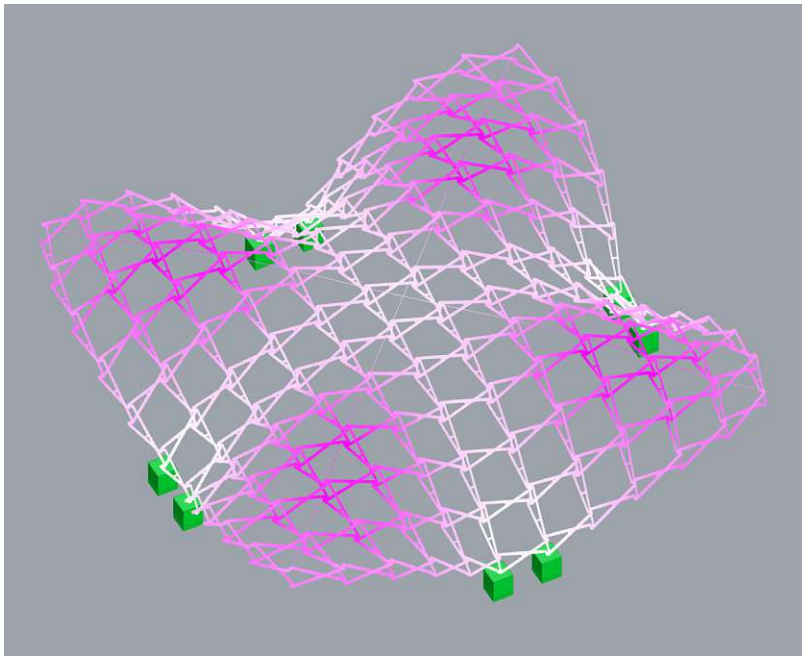


Figure 69: Displacement of "Cross vault 14-11" for LC 0 after cross-section optimization targeting the wall thickness of the scissor bars. Max. displacement of 10.21 cm.

CROSS-SECTION OPTIMIZATION LC 1

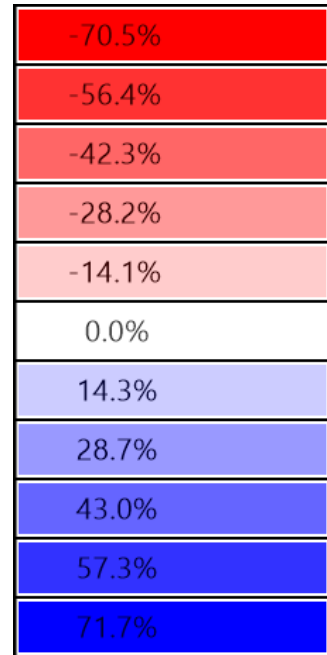
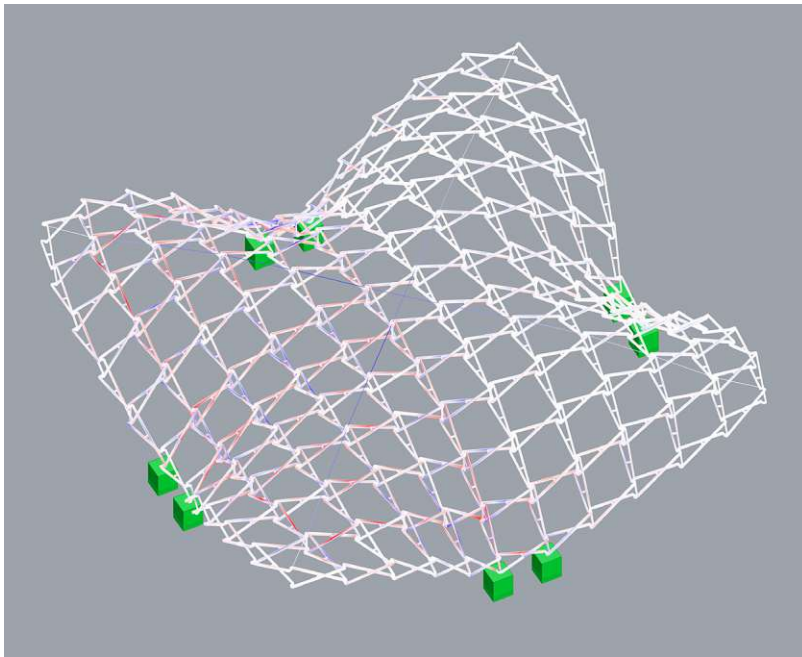


Figure 70: Utilization of "Cross vault 14-11" for LC 1 after cross-section optimization targeting the wall thickness of the scissor bars ranges between -70.5% and 71.7%.

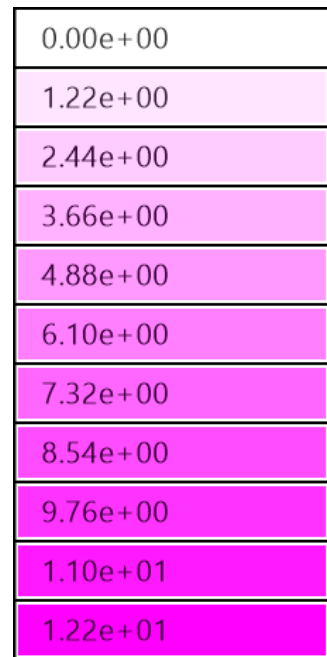
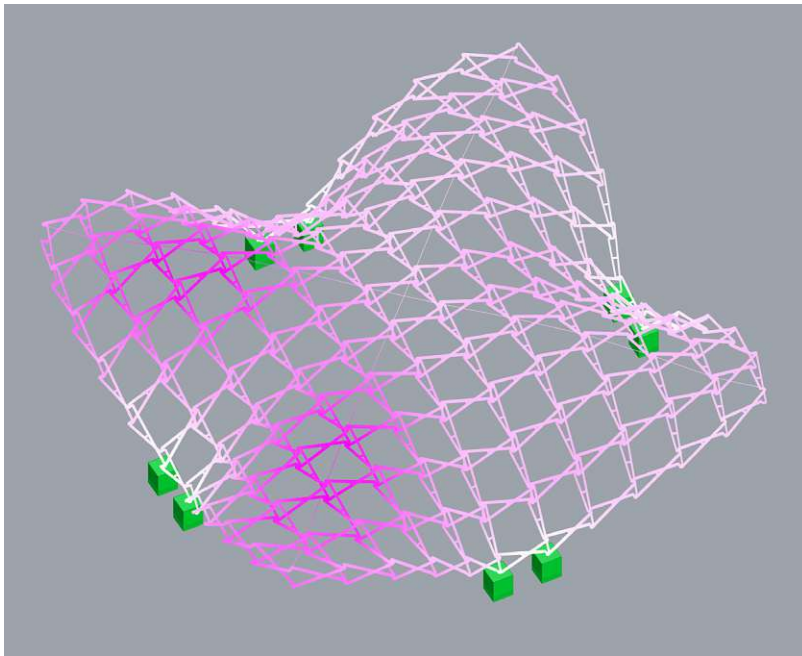


Figure 71: Displacement of "Cross vault 14-11" for LC 1 after cross-section optimization targeting the wall thickness of the scissor bars. Max. displacement of 12.21 cm.

4.4.4. Deployment simulation

CROSS-VAULT 14-11		
SIMULATION SPECIFICATIONS	deployed	contracted
deployment factor [c]	0.00	0.77
BB side length [m]	15.80	5.04
BB height [m]	4.15	2.93
vertical distance betw. nodes [m]	0.60	1.55
volume expansion [%]	100	7.14

MODEL SPECIFICATIONS	structurally determined values
number of scissor bars [n]	528
scissor bar member length [m]	1.10-1.98
scissor bar cro-sec dimension [mm]	40x80
number of nodes [n]	288
node diameter/hinge length [mm]	180

Table 16: Evaluation of the deployment simulation for "Cross-vault 14-11".

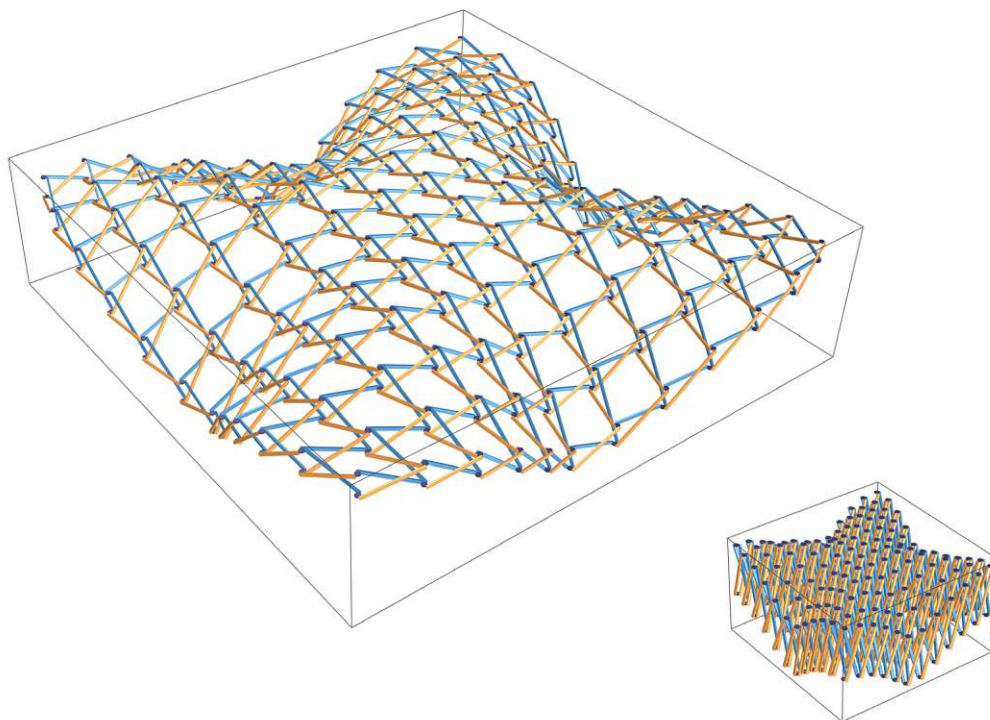


Figure 72: Deployment simulation for "Cross-vault 14-11" at two stages of deployment. Fully deployed structure (left) and maximum contraction (right).

4.4.5. Discussion

The initial structural model for cross-vault 14-11, consisting of 528 scissor bars with a cross-section dimension of 40x80x5mm and vertical bracing members for all 144 upper and lower node pairs, shows utilization of max. -56.5% to 60.9%, and a maximum displacement of 5.09 cm under an asymmetric load (LC1).

BESO optimization on the vertical bracing members reduces their number from 144 to 57. Cross-section optimization of the scissor bars results in the majority of members having their wall thickness reduced to 2.9 mm thickness. Eight scissor bars remain, needing a thicker dimension, with a wall thickness ranging from 4 mm to 7.1 mm. Both optimization steps are performed under LC0.

The resulting model shows a weight reduction of approximately one ton. Utilization ranges from -70.5% to 71.7%, and maximum displacement increases, but is limited to a maximum of 12.21 cm for LC1.

The results of the deployment simulation (Fig. 72) are summarized in Table 16. While this second cross vault model is smaller in dimension, constructed with smaller node diameter and cross-section dimensions, when compared to the previous version, its expansion ratio is lesser. Collisions occur at a deployment factor of $c=0.77$ when the bounding box side length is reduced from 15.80 m to 5.04 m. An area of 250 m² is reduced to 25 m². The structure in its contracted state takes up only 7.14% of the volume, it occupies when completely deployed.

While this second iteration of the cross-vault geometry performs better structurally, the deployment results are less efficient. For the third and final case study, a hyperbolic barrel vault will be presented in the next section.

4.5. Barrel vault 12-10

In the interest of showing more variety and testing the boundaries of such structures a third and final scissor grid is generated and subjected to analysis. The structure is designed in the shape of a hyperbolic barrel vault with two diagonally opposite corners raised. This configuration is structurally more challenging than the previously presented cross-vaults as the support points are asymmetrically arranged, located at two diagonally opposite corners.

4.5.1. Base grid geometry

The base grid geometry is presented in Figure 73. It covers an area of 190 m² and has a resolution of 10 units along u and v directions. The rise at the highest point of the vault measures 4.51 m. The structure is supported by two groups of six adjoining lower nodes, located on opposite ends of two facing boundary contours. In addition to the vertical bracing elements, five steel ropes are introduced, running diagonally between the elevated corners to provide further stiffness. The scissor structure is composed of translational units with a structural thickness of 60 cm, resulting in 440 scissor bars with a member length of 1.04 m to 1.96 m, connected by 220 hinges and 242 nodes (Tab. 17).

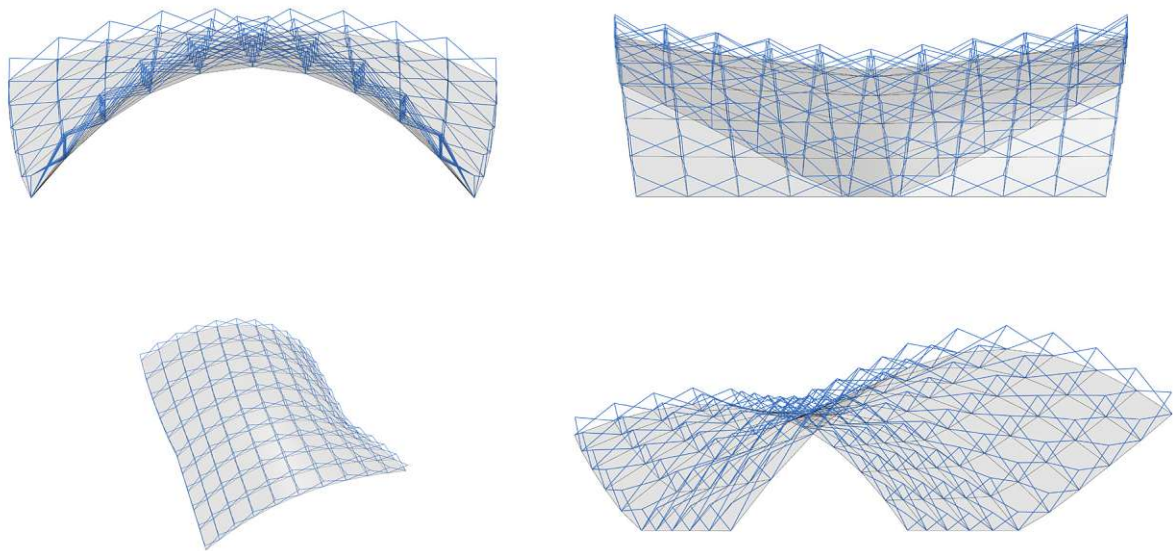


Figure 73: Line model of the base grid geometry for "Barrel-vault 12-10".

BARREL VAULT 12-10	
BB side length LxW [m]	14.70x12.90
BB area [m ²]	189.63
BB hight [m]	5.88
interior rise [m]	4.51
UV resolution	10x10
unit type	translational
structural thickness [m]	0.60
number of scissor bars [n]	440
scissor bar member length [m]	1.04-1.96
number of hinges [n]	220
number of nodes [n]	242

Table 17: Model specifications for "Barrel-vault 12-10".

4.5.2. Load cases

Figure 74 shows the loads acting on the structural model in LC0 and LC1. The resulting pattern of vertical bracing rods before and after BESO optimization is shown in Figure 75. The structure is also subjected to cross-section optimization of the wall thickness of the scissor bars. Results are documented in the next section.

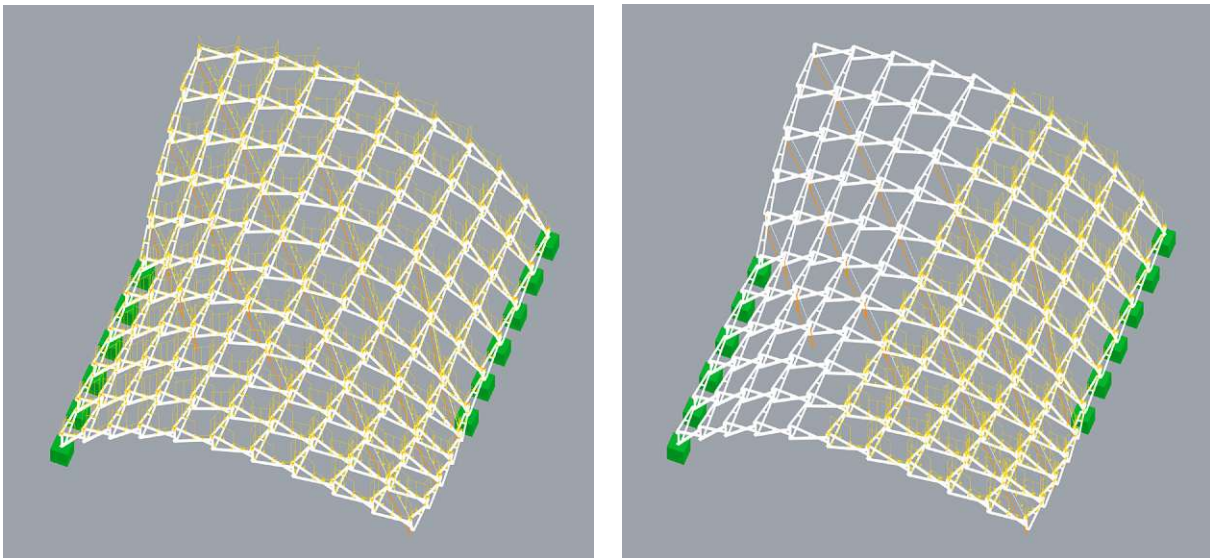


Figure 74: : Loads acting on the structural model for "Barrel-vault 12-10". LC 0 (left), LC 1 (right)

4.5.3. Cross-section dimensions and optimization

BARREL-VAULT 12-10						
INDIVIDUAL MEMBERS			initial model		optimized model	
material	member	cro-sec	quantity [n]	cro-sec dim. [mm]	quantity [n]	cro-sec dim. [mm]
AW 7020 T6 ft=28kN/cm ²	scissor-bars	rec.	440	100x50x5.6	419	100x50x3.0
		rec.			5	100x50x3.6
		rec.			4	100x50x4.5
		rec.			3	100x50x5.6
		rec.			3	100x50x5.0
		rec.			2	100x50x8.8
		rec.			1	100x50x10.0
		rec.			1	100x50x6.3
		rec.			1	100x50x4.0
		rec.			1	100x50x3.2
	vertical bracing	circ.	121	80x12	47	60x6
	hinges	circ.	220	60x8	264	60x2
	nodes	circ.	242	80x10	288	60x10
S 355	steel cables	circ.	5	14	2	14

Table 18: Cross-section table for "Barrel-vault 12-10". Initial model and optimization results, affected values are highlighted in bold letters.

ENTIRE STRUCTURE		initial model	optimized model
	weight [kg]	3916	2431
LC0	utilization [%]	-40.9 - 56.1	-70.6 - 73.0
	displacement [cm]	5.24	29.34
LC1	utilization [%]	-51.8 - 60.1	-67.5 - 72.3
	displacement [cm]	10.30	33.27

Table 19: Weight, utilization and displacement values for "Barrel-vault 12-10". Results for the initial and the optimized model and both load cases.

Amounts and dimensions for all building members, along with utilization and displacement range for the initial model and the optimized model are presented in Tables 18 and 19.

The documentation of these results for the initial model and each optimization step under both load cases is presented on the following pages in figures 77 through 88.

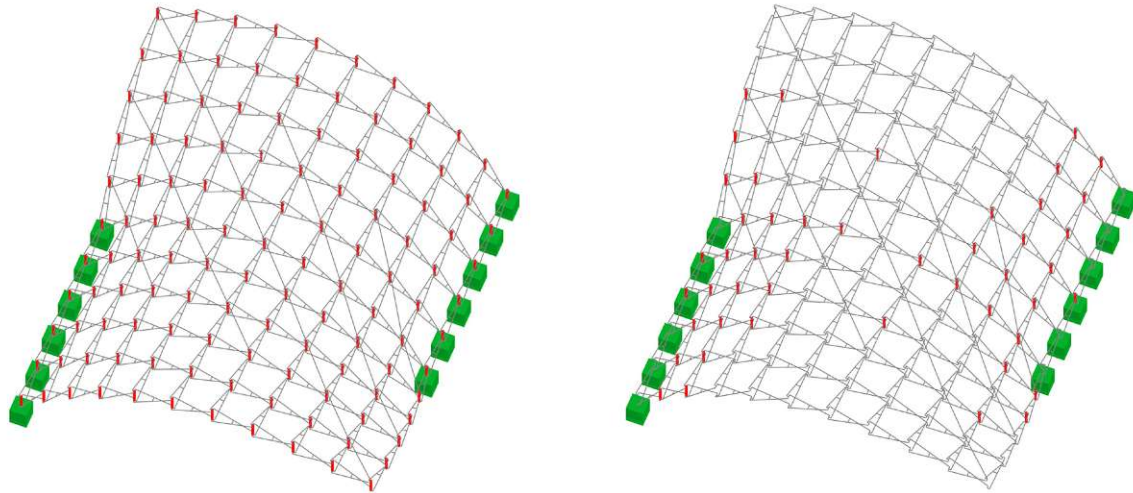


Figure 75: Result of BESO optimization on the number of vertical bracing rods for "Barrel vault 12-10". Of 121 rods in the initial model (left), 47 remain, 74 are not utilized (right).

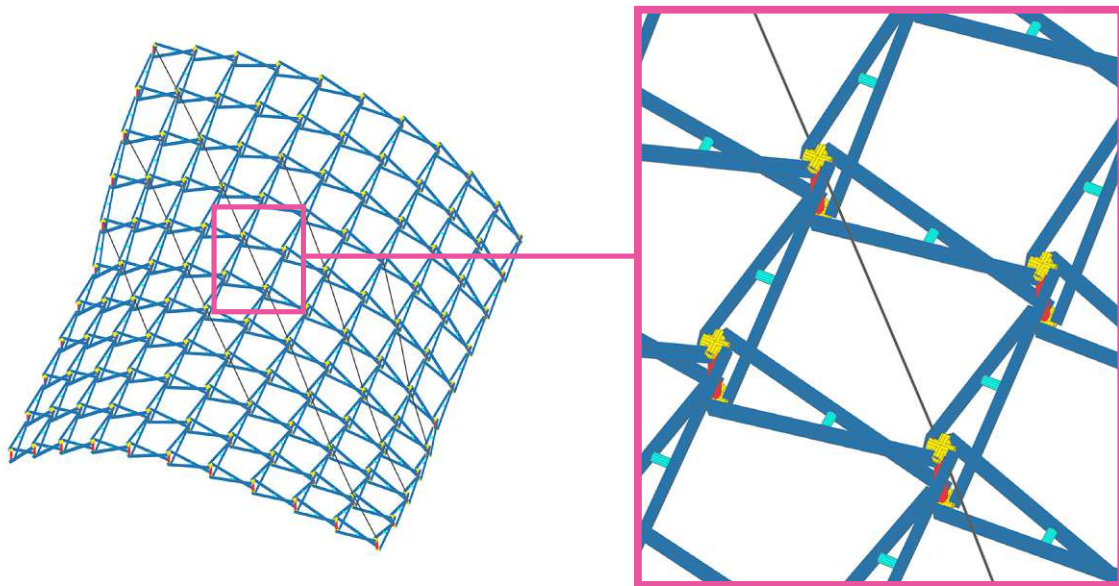


Figure 76: Color-coded cross sections, as referenced in Tab. 17 for "Barrel-vault 12-10".

INITIAL MODEL LC 0

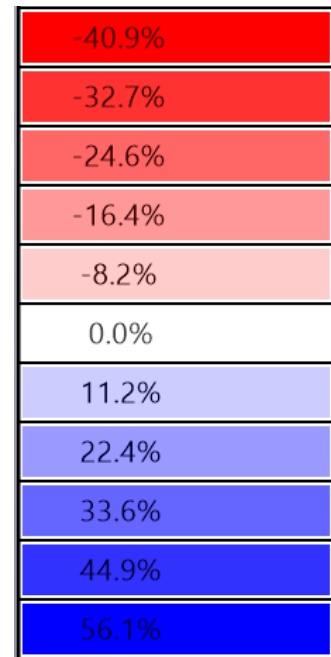
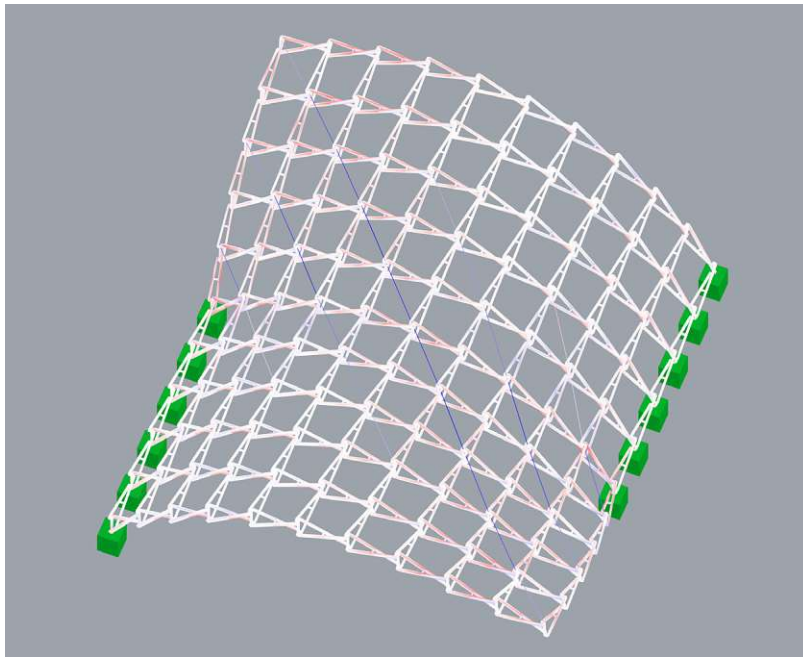


Figure 77: Initial model "Barrel-vault 12-10" for LC 0. Utilization ranges between -40.9% and 56.1%.

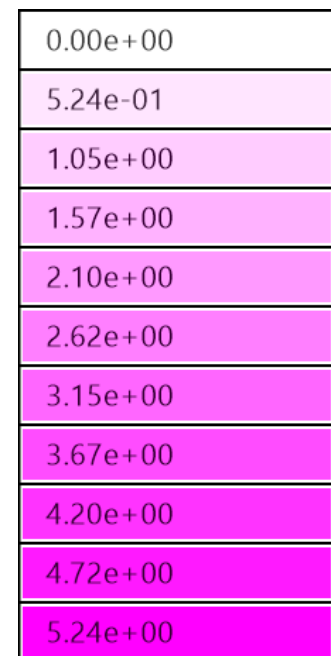
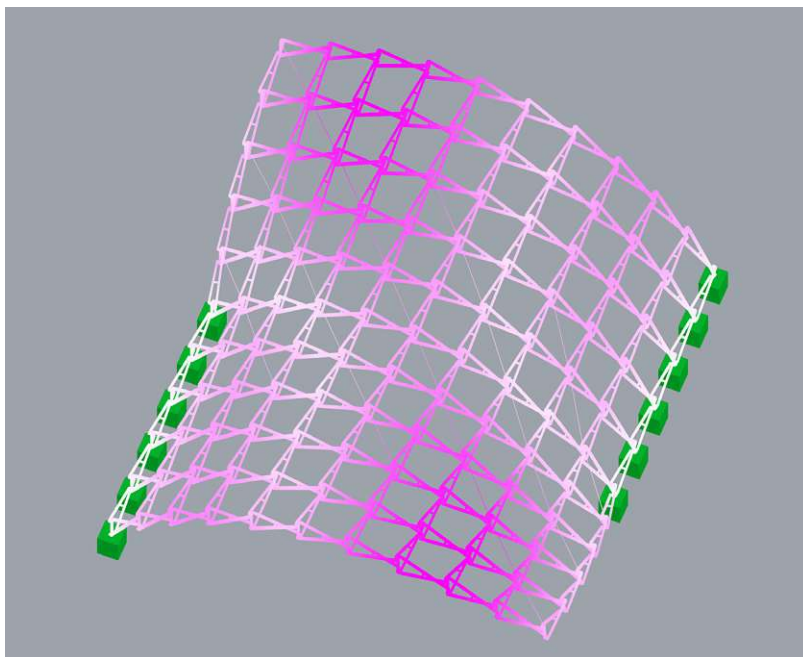


Figure 78: Initial model "Barrel-vault 12-10" for LC 0. Maximum displacement of 5.24 cm.

INITIAL MODEL LC 1

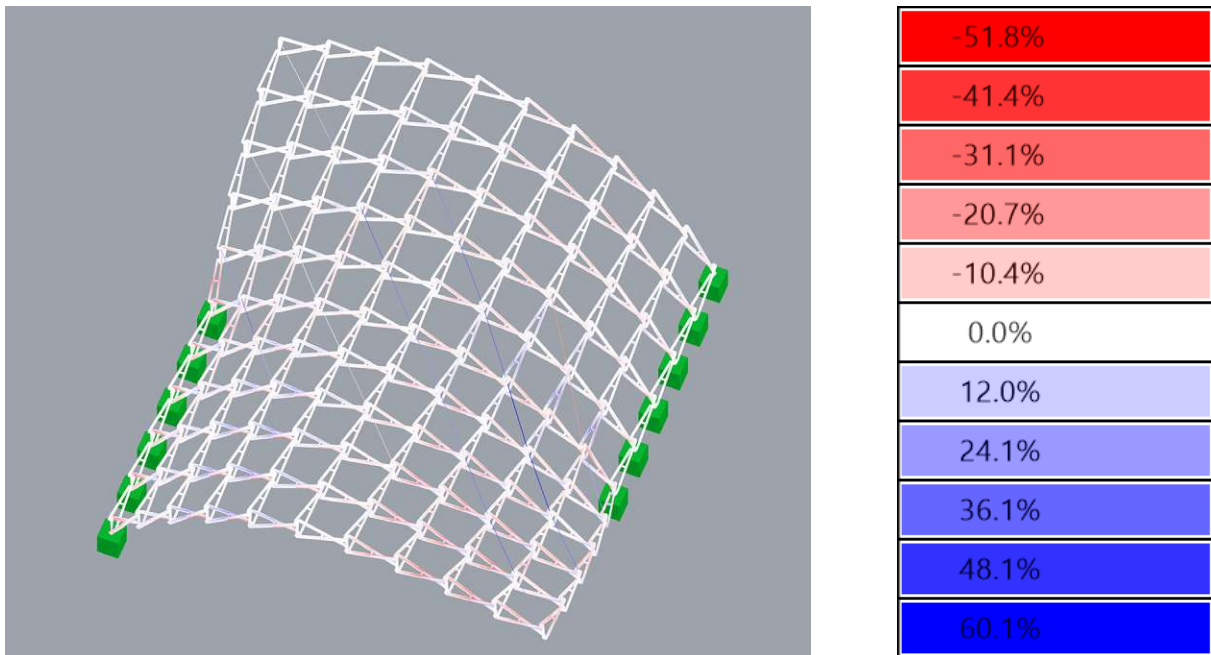


Figure 79: Initial model "Barrel-vault 12-10" for LC 1. Utilization ranges between -51.8% and 60.1%.

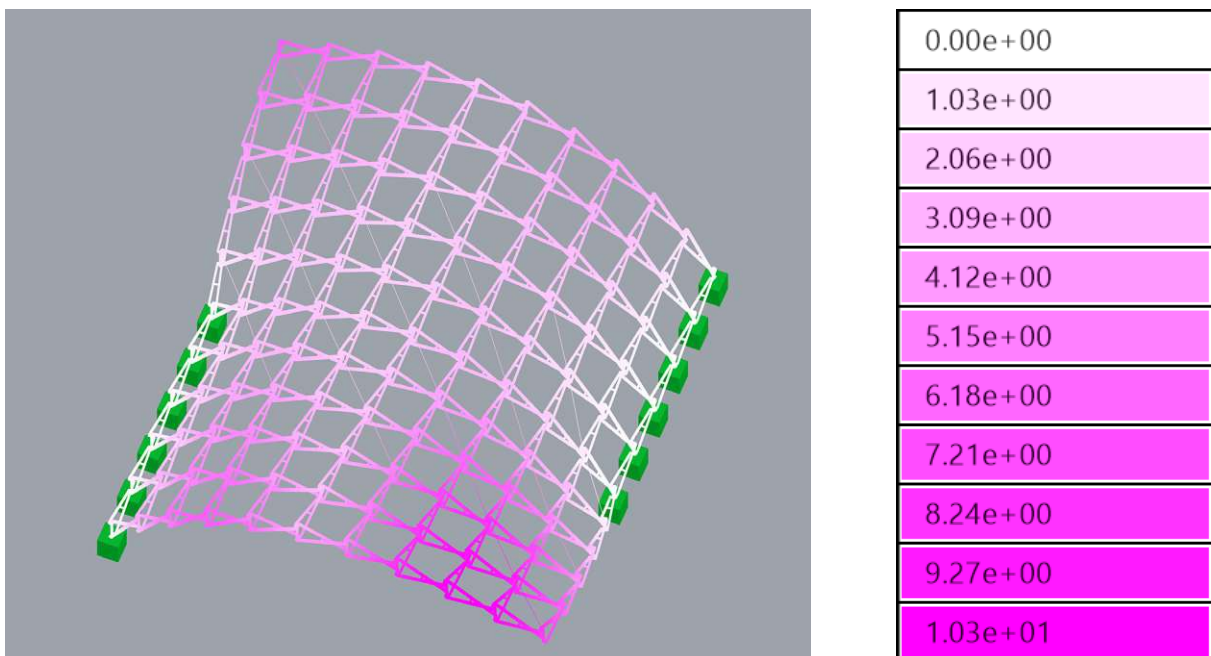


Figure 80: Initial model "Barrel-vault 12-10" for LC 1. Maximum displacement of 10.33 cm. .

BESO OPTIMIZATION LC 0

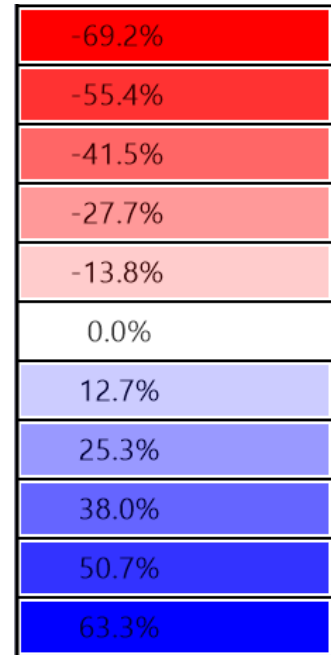
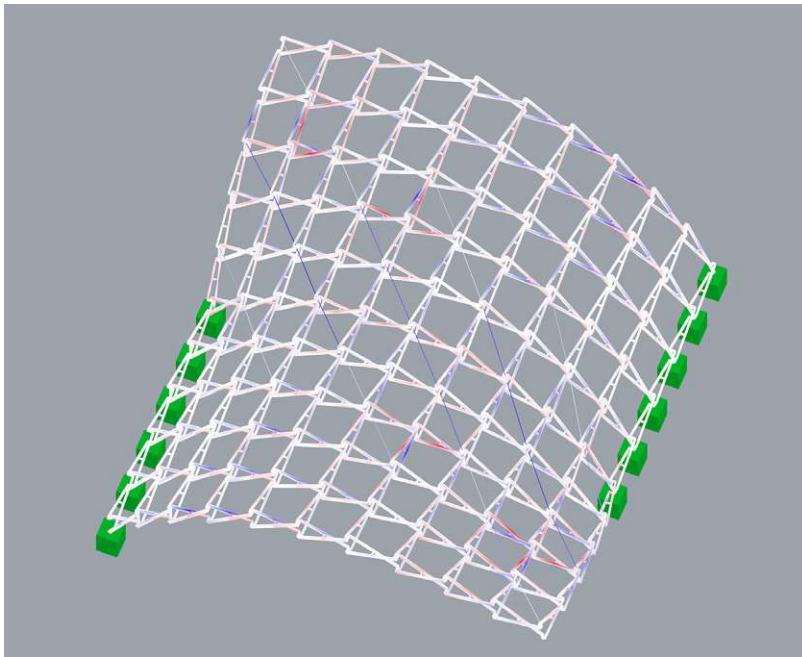


Figure 81: Utilization of "Barrel-vault 12-10" for LC 0 after BESO optimization on the number of the vertical bracing members, ranges between -69.2% and 63.3%.

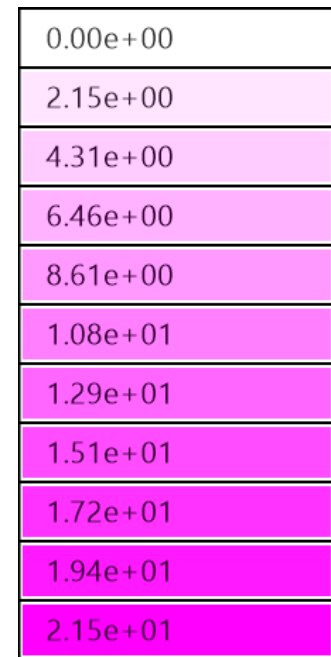
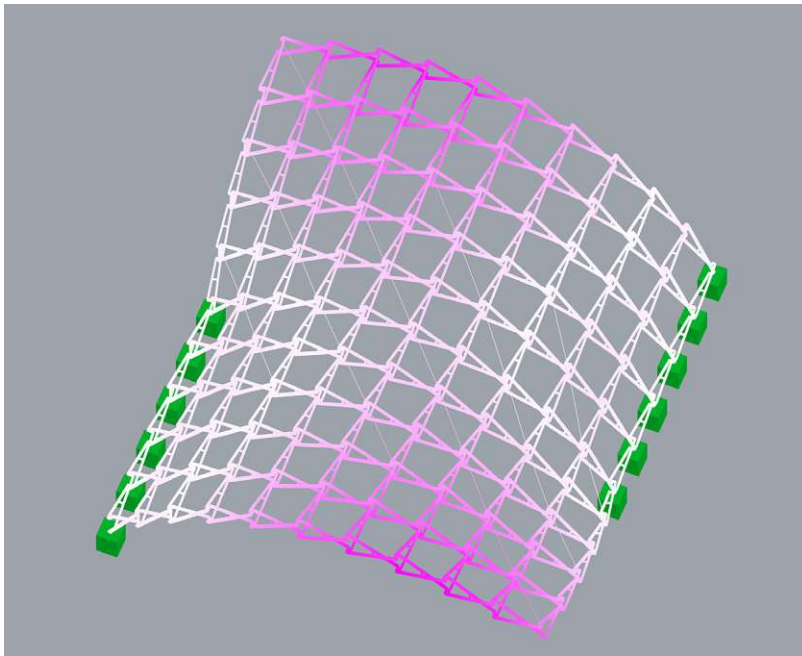


Figure 82: Displacement of "Barrel-vault 12-10" for LC0 after BESO optimization on the number of vertical bracing members. Max. displacement of 21.54 cm.

BESO OPTIMIZATION LC 1

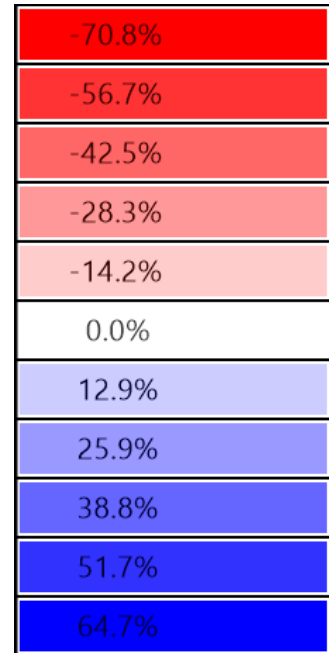
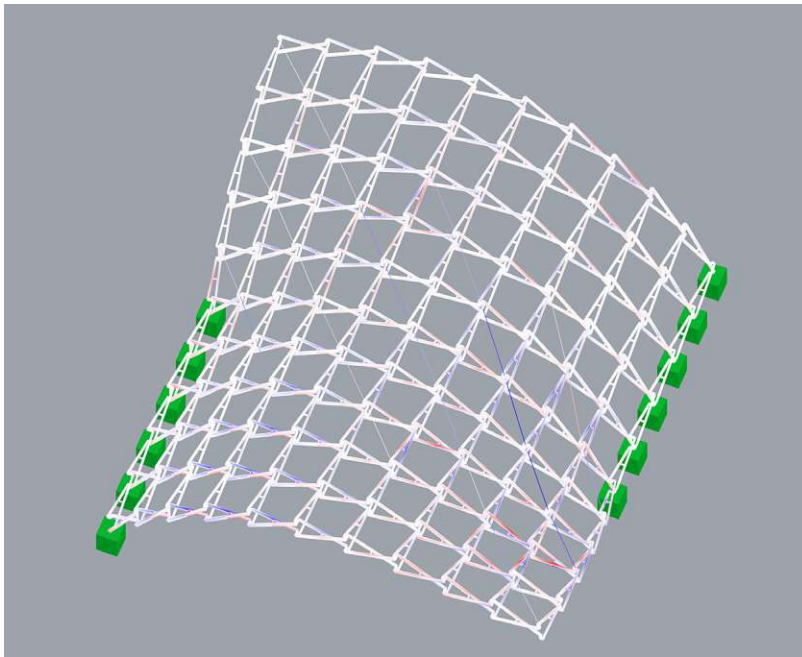


Figure 83: Utilization of "Barrel-vault 12-10" for LC 1 after BESO optimization on the number of the vertical bracing members, ranges between -70.8% and 64.7%.

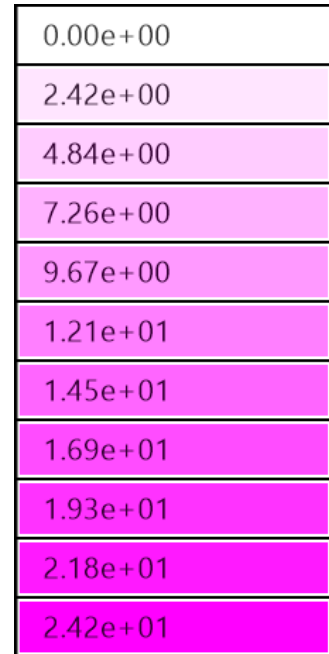
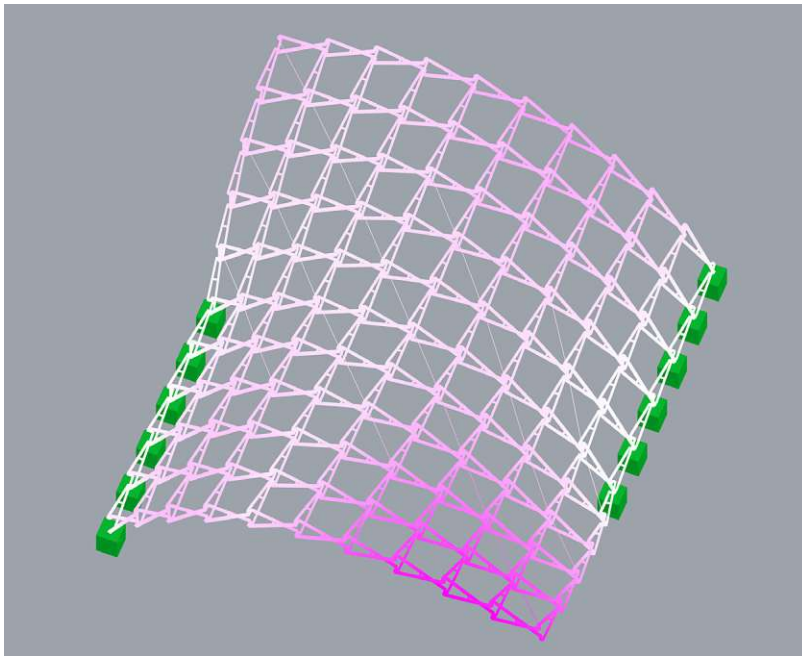


Figure 84: Displacement of "Barrel-vault 12-10" for LC1 after BESO optimization on the number of vertical bracing members. Max. displacement of 24.18 cm.

CROSS-SECTION OPTIMIZATION LC 0

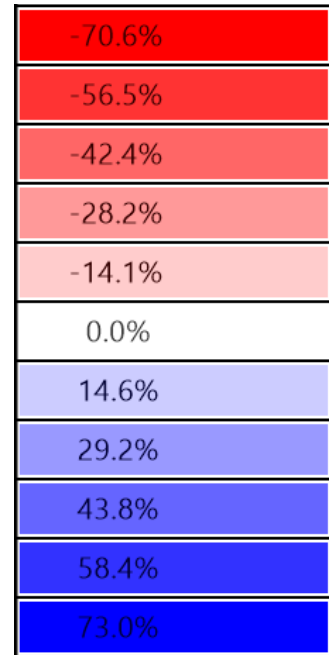
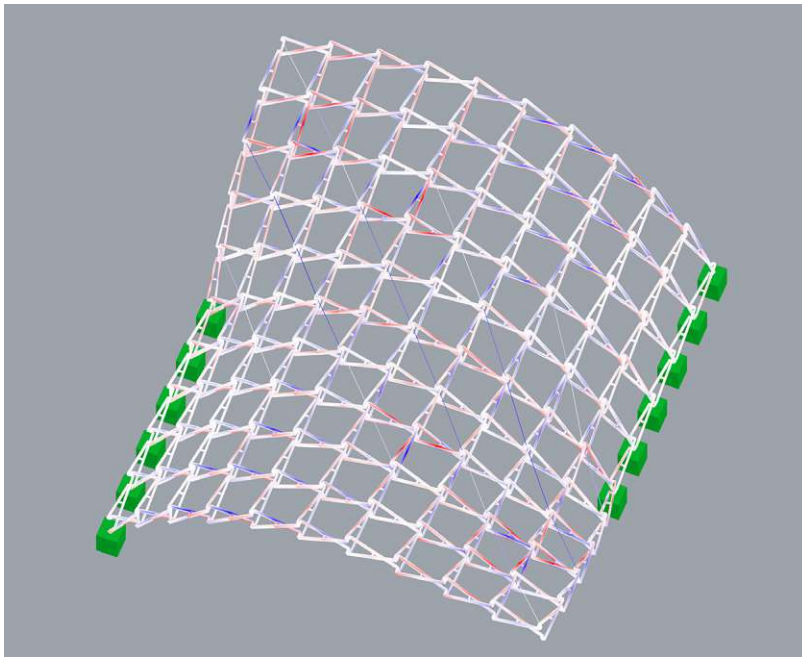


Figure 85: Utilization of "Barrel-vault 12-10" for LC 0 after cross-section optimization targeting the wall thickness of the scissor bars ranges between -70.6% and 73.0%.

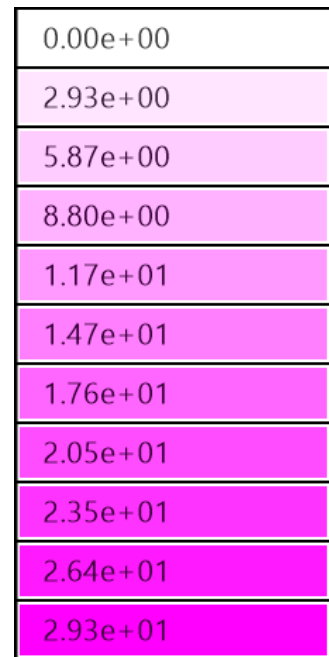
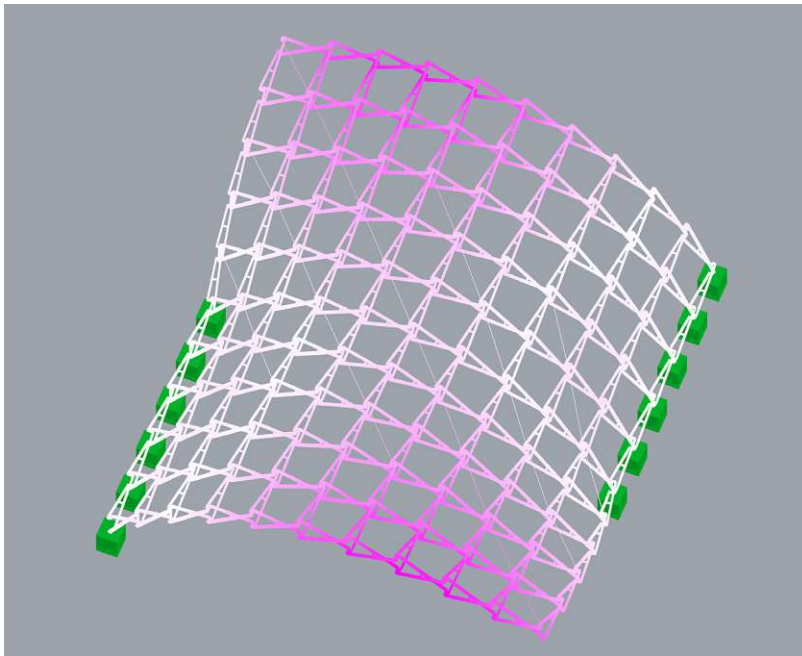


Figure 86: Displacement of "Barrel-vault 12-10" for LC 0 after cross-section optimization Max. displacement of 29.34 cm.

CROSS-SECTION OPTIMIZATION LC 1

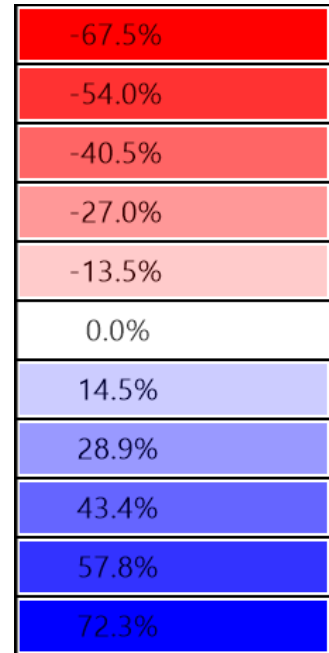
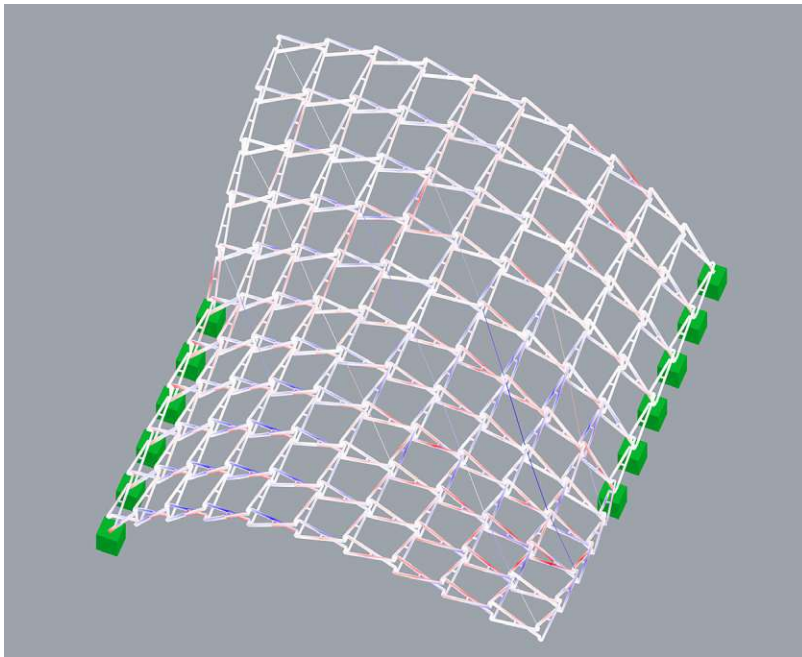


Figure 87: Utilization of "Barrel-vault 12-10" for LC 1 after cross-section optimization targeting the wall thickness of the scissor bars ranges between -67.5% and 72.3%.

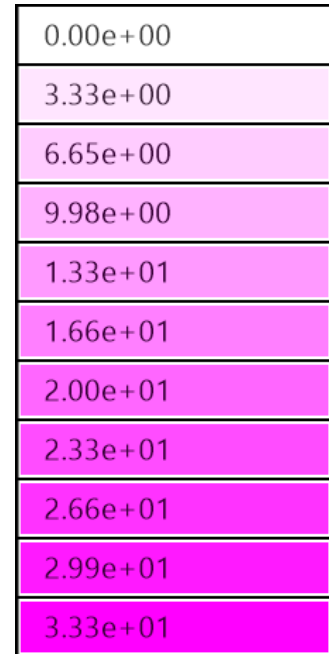
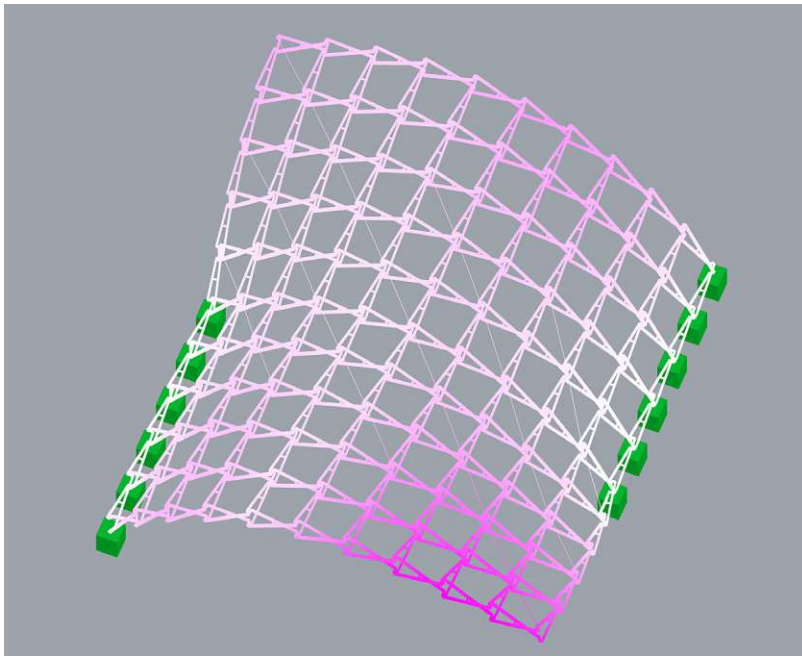


Figure 88: Displacement of "Barrel-vault 12-10" for LC 1 after cross-section optimization targeting the wall thickness of the scissor bars. Max. displacement of 33.27 cm.

4.5.4. Deployment simulation

BARREL-VAULT 14-11		
SIMULATION SPECIFICATIONS	deployed	contracted
deployment factor [c]	0.00	0.72
BB side length [m]	14.70x12.90	5.35x5.69
BB height [m]	5.88	3.65
vertical distance betw. nodes [m]	0.60	1.35
volume expansion [%]	100	9.96

MODEL SPECIFICATIONS	structurally determined values
number of scissor bars [n]	440
scissor bar member length [m]	1.04-1.96
scissor bar cro-sec dimension [mm]	50x100
number of nodes [n]	242
node diameter/hinge length [mm]	160

Table 20: Evaluation of the deployment simulation for "Barrel-vault 12-10".

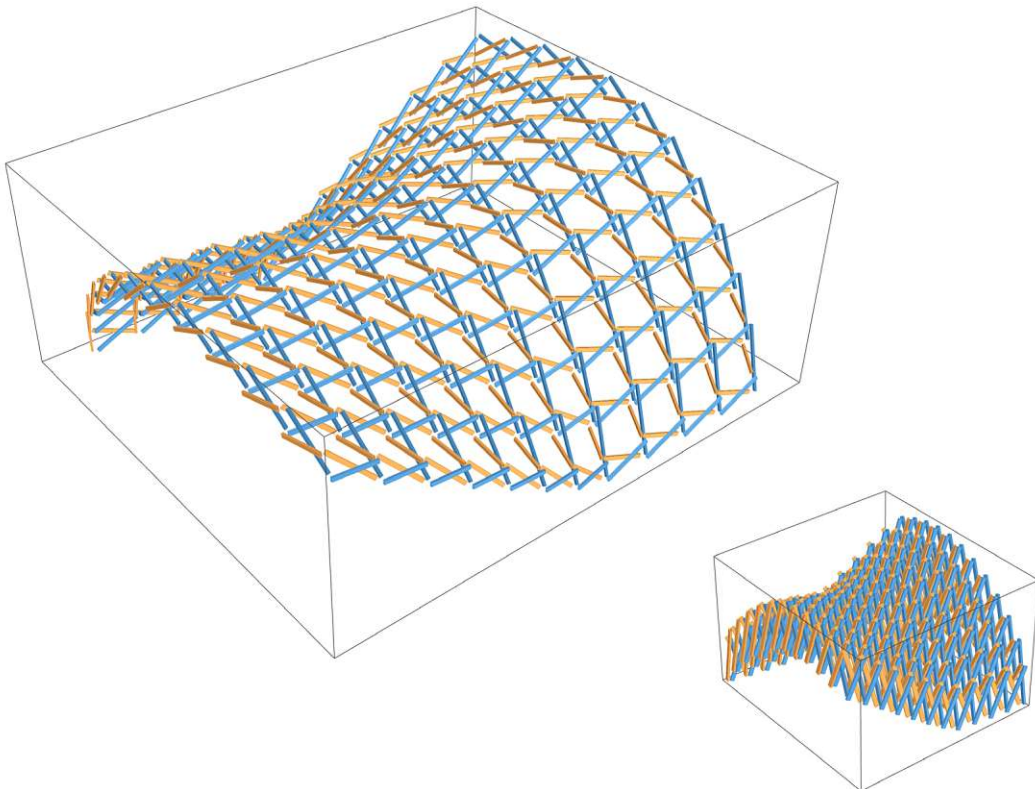


Figure 89: Deployment simulation for "Barrel-vault 12-10" at two stages of deployment. Fully deployed structure (left) and maximum contraction (right).

4.5.5. Discussion

The initial structural model for this barrel-vault, consisting of 440 scissor bars with a cross-section dimension of 50x100x5.6mm and vertical bracing members for all 121 upper and lower node pairs, shows utilization of max. -51.8% -to 60.1%, and a maximum displacement of 10.30 cm under asymmetric load (LC 1). When considering the symmetric load case of 1kN/m² (LC 0), the initial structure shows utilization ranging between -40.9% and 56.1% and a maximum displacement of 5.24cm. Limiting deformation is possible only by bracing all node pairs and adding five steel cables as additional tensioning elements. Material use in comparison with the previous models is less efficient. The structure covers the smallest area and is constructed with the least amount of building members, nevertheless, its weight of 3916 kg puts it in between the two previously presented models which are larger in volume. This is due to the high material use for the hinges, node sleeves, and vertical bracing elements, where the circular cross-sections need a wall thickness of 8 mm to 12 mm to handle the strain of the applied loads.

The optimization results for the barrel vault are less satisfying than those of the previous models. Post optimization utilization for LCO is between -70.6 % and 73.0% with a displacement of almost 30 cm. For LC 1 these values are -67.5% - 72.3%, with maximum displacement of 33.27 cm.

The results of the deployment simulation are summarized in Table 20. While this barrel-vault model is smaller in dimension, when compared to the cross-vaults, its expansion ratio is lesser. This is due to larger cross-section dimensions and higher grid density, both of which are structurally necessary measures. Collisions occur at a deployment factor of $c=0.72$ when the bounding box side length is reduced from 14.70x12.90m to 5.35x5.69m. The area is reduced from 190m² to 30m². The structure in its contracted state takes up only 9.96% of the volume, it occupies when completely deployed.

While this third configuration yields less satisfactory results it illustrates the importance of a well-balanced grid construction in a combination of the parameters base area, grid resolution, distribution of supports, and steepness of the rise to achieve an efficiently performing deployable scissor grid.

4.6. Discussion

The results of the structural analysis, optimization steps, and deployment simulation for all three case studies are summarized in Table 21. As discussed, the cross-vault models show a more efficient use of material with lesser displacement values along with a higher volume expansion ratio. The second iteration of this configuration, “cross-vault 14” shows the best performance overall.

RESULTS (values for LC 1)			
	cross-vault 20-12	cross vault 14-11	barrel-vault 10-12
BB area deployed [m ²]	582	250	190
BB volume contracted [%]	4.34	7.14	9.96
scissor bars quantity	624	528	440
nodes quantity	338	288	242
weight initial [kg]	6890	3233	3916
weight optimized [kg]	4046	2151	2431
max. utilization initial [%]	-69.7 - 71.6	-56.5 - 60.9	-51.8 - 60.1
max. displacement initial [cm]	8.21	5.09	12.33
max. utilisation opt. I [%]	-74.4 - 76.5	-68.3 - 69.4	-70.8 - 64.7
max. displacement opt I [cm]	11.9	8.79	24.18
max. utilization opt. II [%]	-79.5 - 81.7	-70.5 - 71.7	-67.5 - 72.3
max. displacement opt. II [cm]	18.30	12.21	33.27

Table 21: Comparison of analysis, optimization and simulation results for all three case studies.

5. DETAIL DESIGN AND PROTOTYPING

5.1. Introduction

The following chapter addresses the questions of detailing solutions, suitable for efficient fabrication and easy assembly.

Particular attention is given to the development of a rationalized node connector. A single building component with variable axis orientation. This way, every scissor linkage can be connected using the same building part, the fabrication of which can be serialized. Further, the connection of upper- and lower-layer nodes by vertical bracing members is examined, and a design for telescopic rods containing a 2-stage linear drive system to control the deployment process is presented.

Before moving on to the detailing steps, the next section documents the production of two functioning prototypes, proofing the concepts developed on the digital model. This will provide insight into the design requirements for the mechanical parts, as well as demonstrate the proposed structure's behavior during the deployment process.



Figure 90: Node detail Prototype B.

5.2. Proof of concept

To verify the results documented in the previous chapter two functioning prototypes at a scale of 1:5 are built, based on the model “Cross-vault 20-12”.

For prototype A, a patch consisting of three by three scissor modules located at the outer corner of the structure is extracted (Fig. 91). For prototype B a patch of four by four modules, located at one of the support points of the structure, is extracted (Fig. 92). Scissor units, hinges, and nodes are modeled in detail for fabrication.

The individual scissor bars are cut out of 10 mm thick beech plywood, each providing three drill holes, two at the end for connection to the nodes and one at the center for connection with the hinges. The length of the scissor bars ranges from 26.7 cm to 47.8 cm.

The hinges are designed in form of steel bolts, lying within a cylindrical sleeve keeping the mechanically necessary distance. The node connectors have the form of cylindrical extrusions with the necessary holes in the walls to receive the nuts and bolts, which will connect the ends of the scissor bars while allowing for one degree of freedom.

Prototype A consists of 48 bars, 24 hinges, and 32 nodes. Prototype B consists of 80 bars, 40 hinges, and 50 nodes. All parts are modeled in 3d, labeled, and nested for fabrication by CNC milling and 3d printing. This process is documented in Figures 93-101.

The fully assembled prototypes are shown in its contracted and deployed state in Figures 102-105. The assembly is fairly straightforward, due to the fact, that translational units have their hinge point, always located at the center point of a scissor bar, as the semi-lengths of each bar have the same length. This is advantageous, as it eliminates the risk of placing a member in the wrong direction during assembly.

The deployment process is smooth, while the structure is quite rigid and shows little deformation. This is considered a success, as it shows, that the simulation of deployment executed with the digital model in Kangaroo2 produces a reliable result.

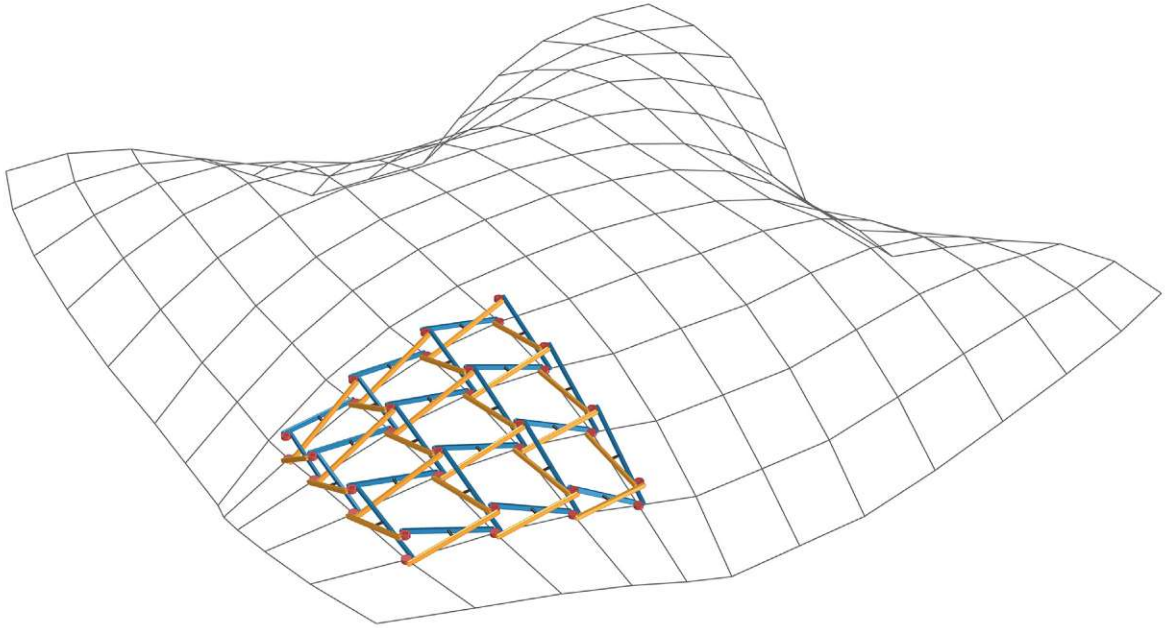


Figure 91: Extracted patch for prototype A. Three by three modules located at one of the raised corners of the structure.

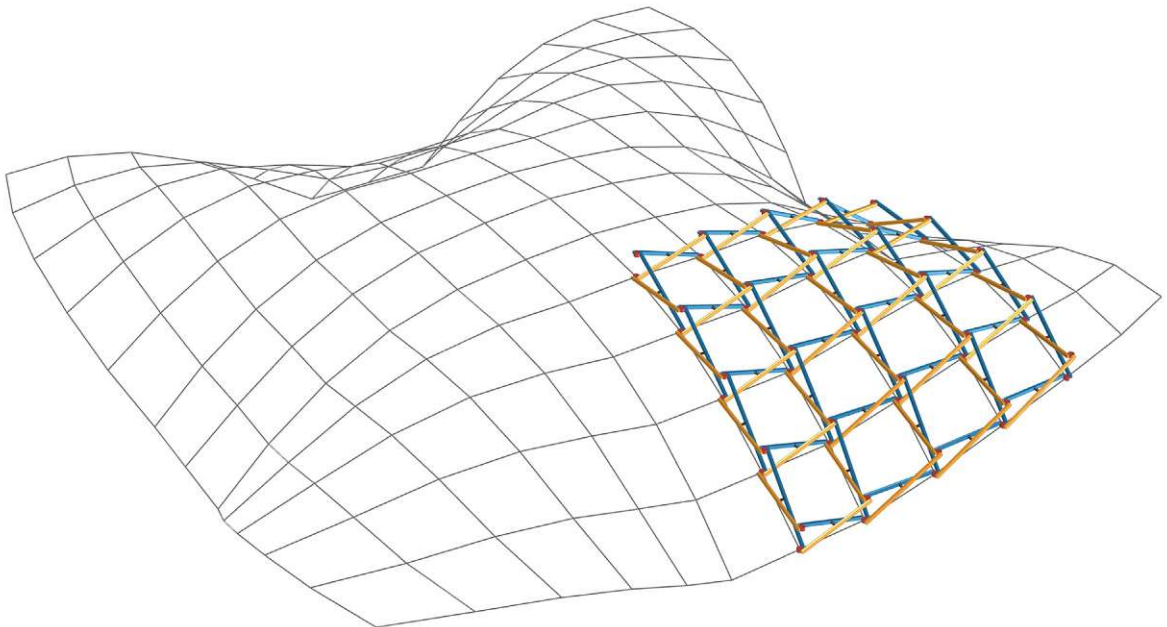


Figure 92: Extracted patch for prototype B. Four by four modules located at one of the support points of the structure.

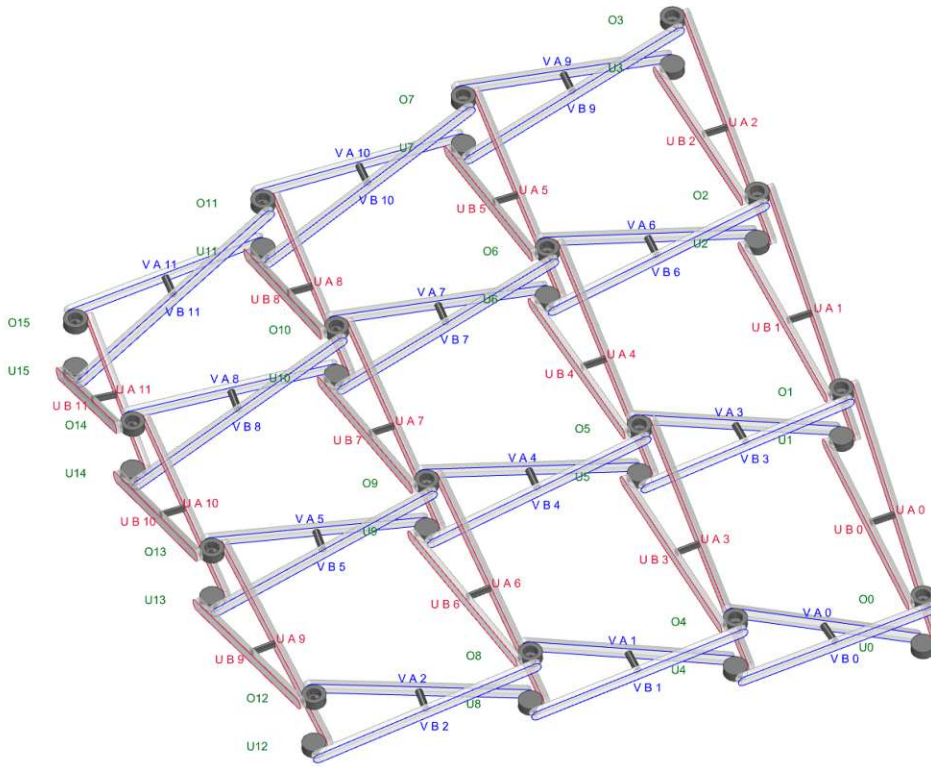


Figure 93: Prototype A, labeling for fabrication and assembly.

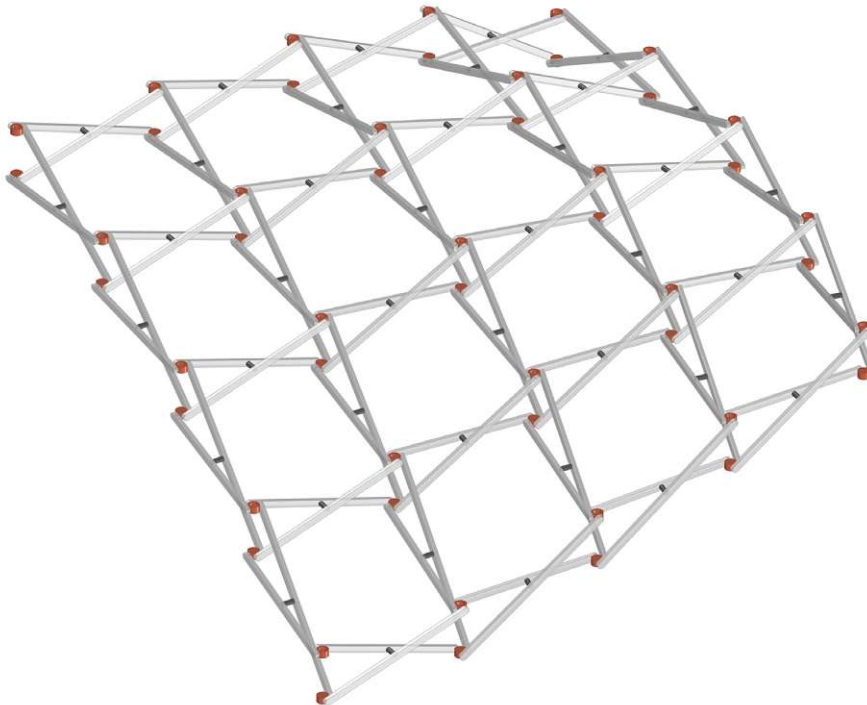


Figure 94: Prototype B, detailed model.

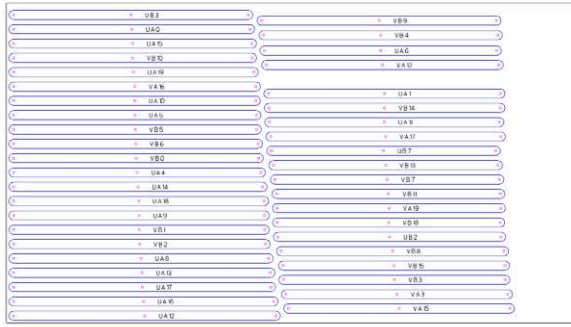


Figure 95: Nested and labeled scissor bars for milling.

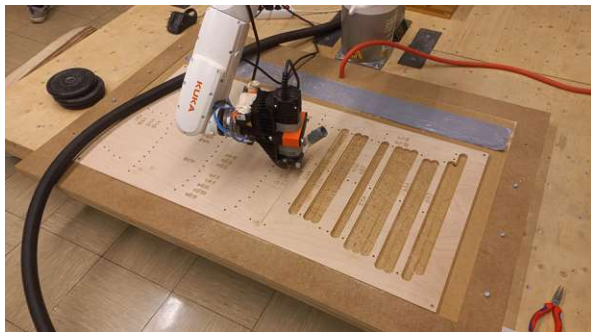
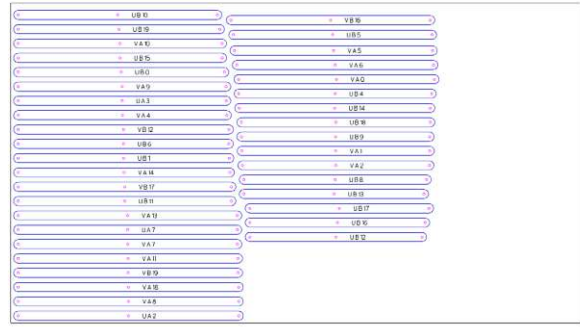


Figure 96: CNC milling of scissor bars.



Figure 97: Scissor bars for assembly.



Figure 98: 3d printed node-connector.



Figure 99: Disassembled scissor unit.



Figure 100: Assembled scissor unit, closed.



Figure 101: Assembled scissor unit, open.



Figure 102: Prototype A, contracted.

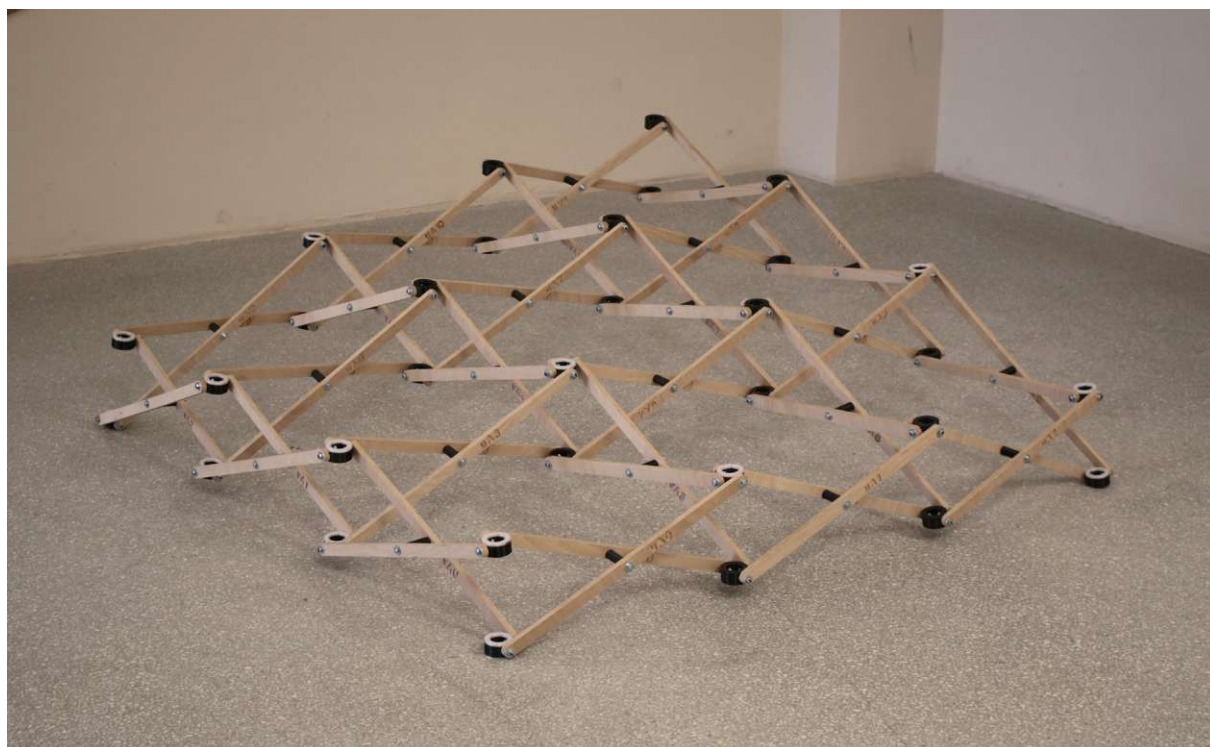


Figure 103: Prototype A, deployed.

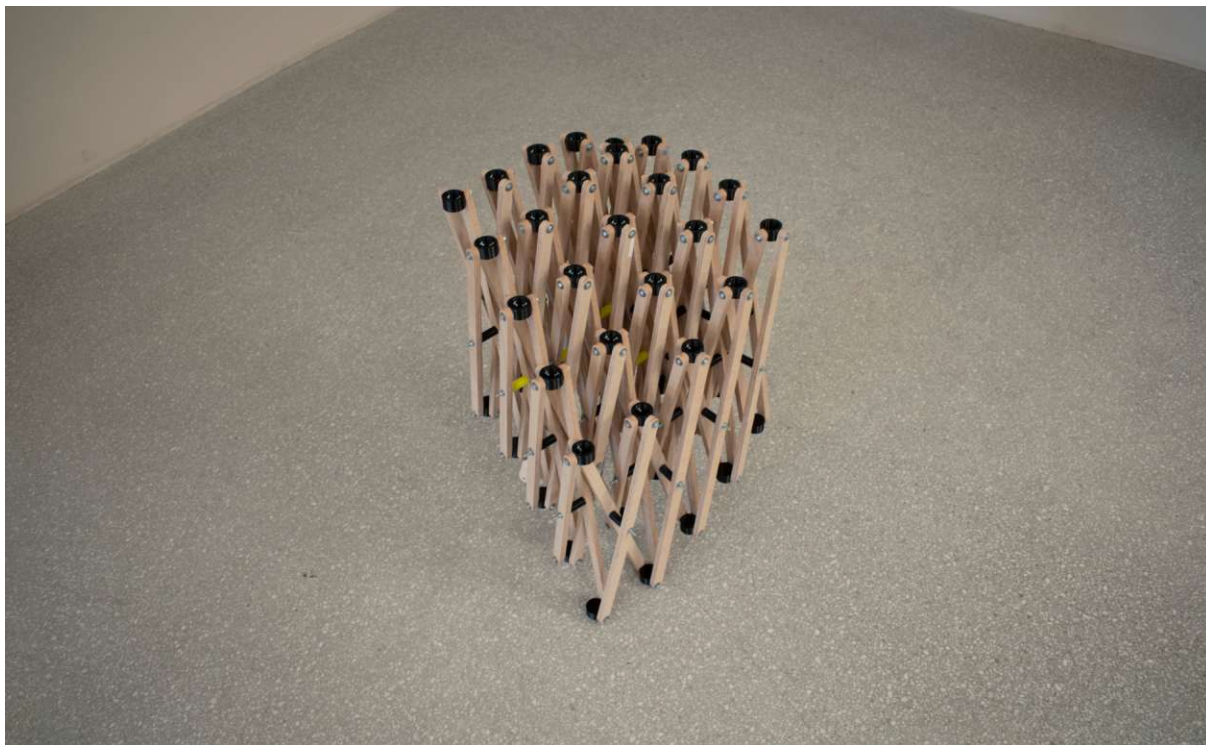


Figure 104: Prototype B, contracted.

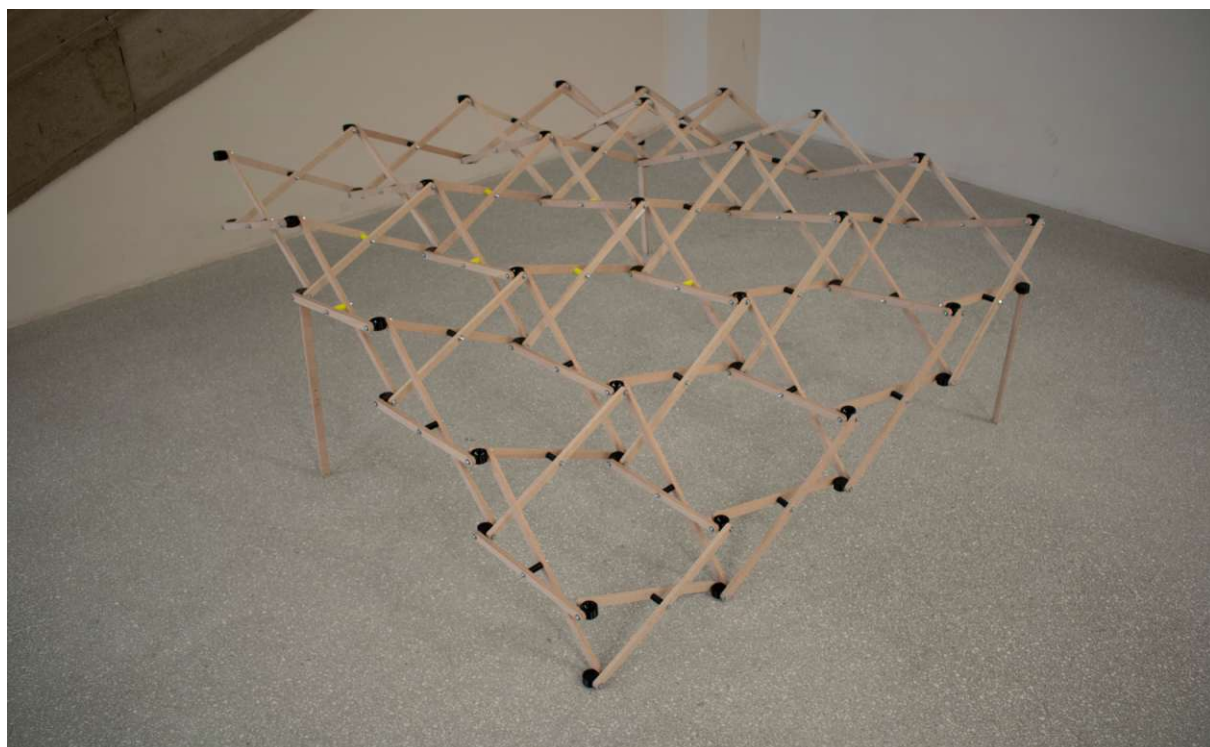


Figure 105: Prototype B, deployed.

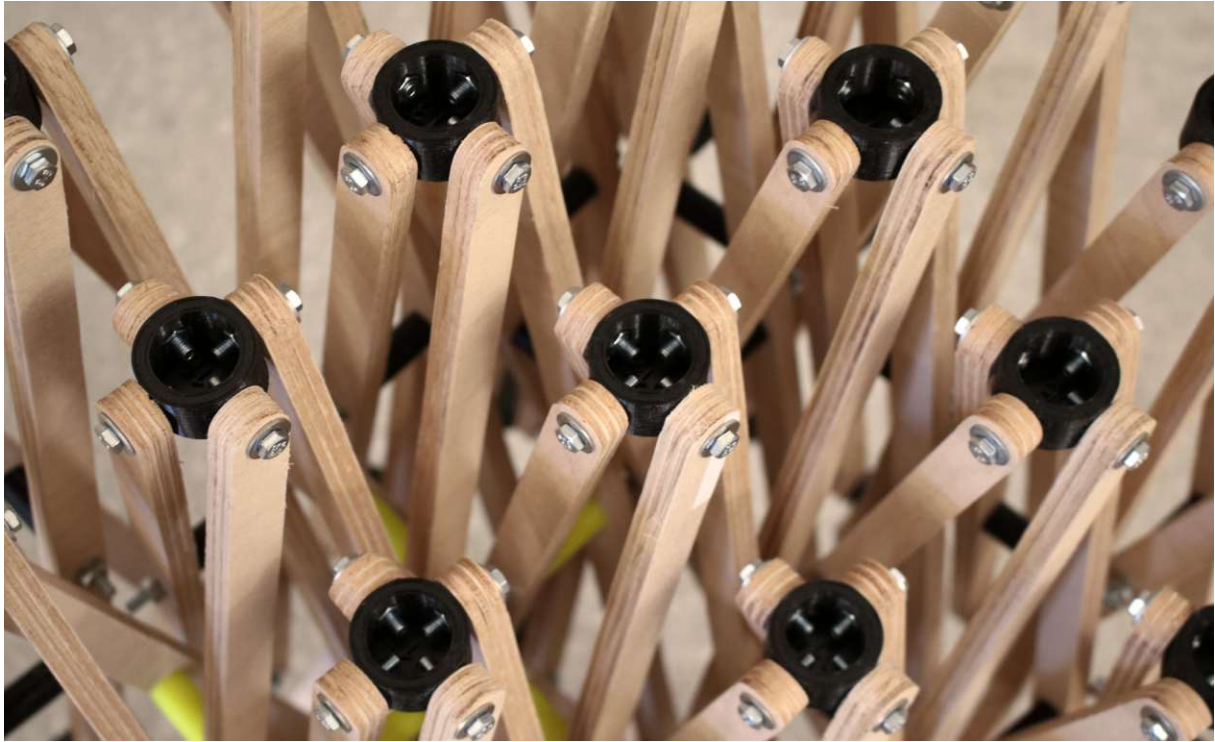


Figure 106: Prototype B, close-up, contracted.

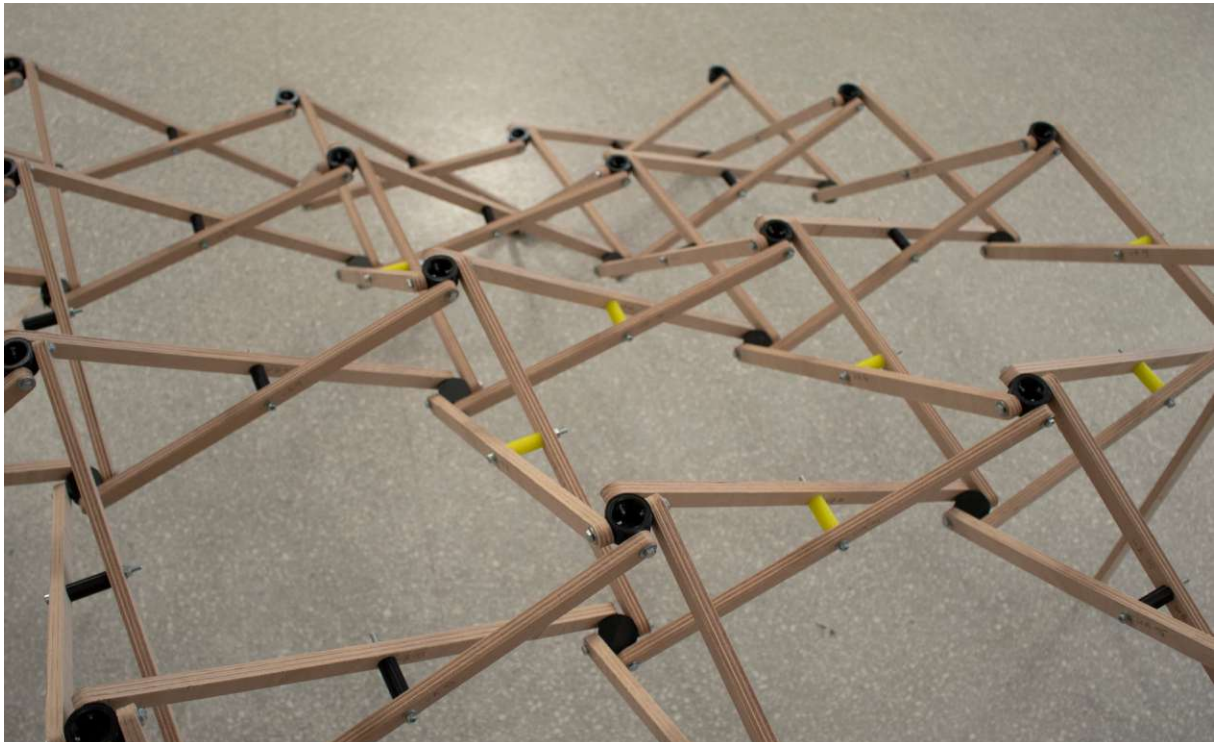


Figure 107: Prototype B, deployed.



Figure 108: Prototype B, close-up, deployed.

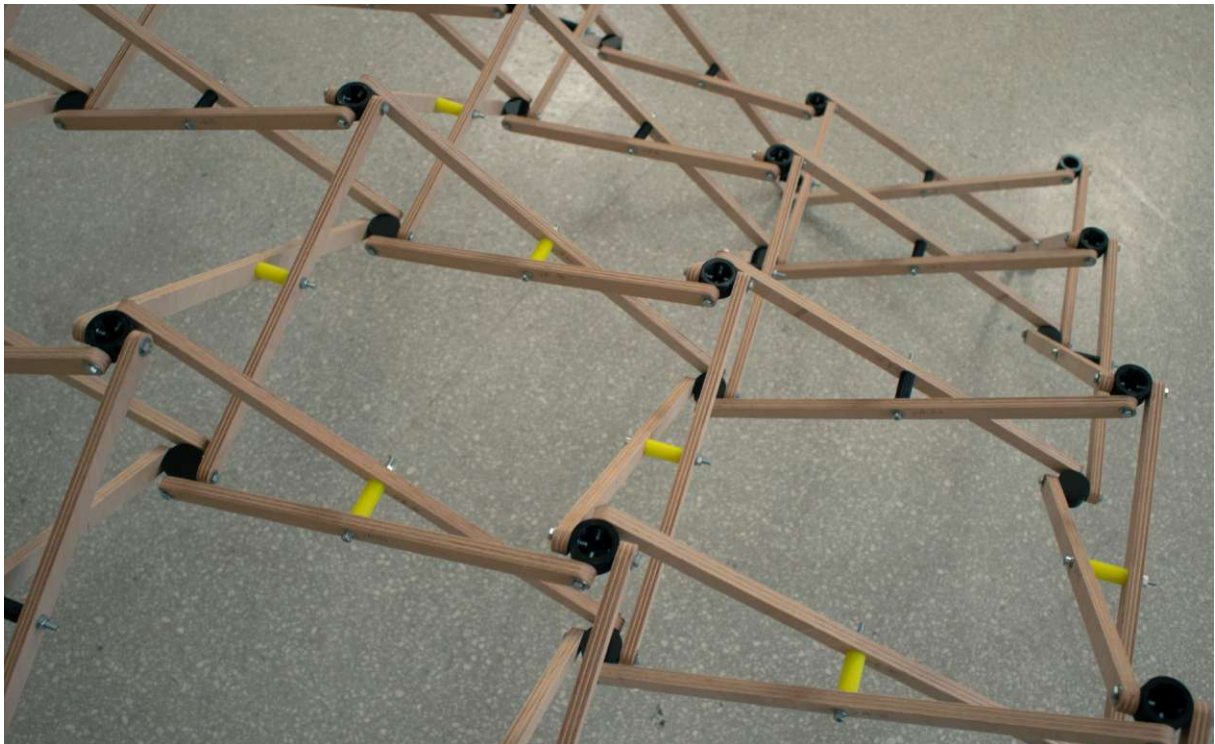


Figure 109: Prototype B, deployed.

5.3. Node connectors and vertical bracing rods

To develop detailing solutions for the design of the vertical bracing members connecting the upper and lower layer of nodes, as well as for the node connectors themselves the following sections will present two design iterations along with isometric representations, section drawings, and prototypical scale models constructed to test functional efficiency.

5.3.1. Bracing node prototype

After building the first functioning prototypes, to test the reliability of deployment, some consideration was given to developing a design strategy for minimizing the node diameter and connecting the vertical bracing members.

A prototype model was built, where the node connectors are constructed in the form of four sleeves arranged crosswise, each containing an internal screw thread to connect four scissor units, for which the end joints are designed in form of lugs. These lugs can be moved out of the axis of the scissor bars to minimize the node diameter and hinge length.

In addition to minimizing the node diameter, a bracing member in form of a telescopic rod is introduced to the model, connecting the upper and lower layer of node connectors. The telescopic rod will expand when contracted and retract during deployment. In addition to its function as a bracing member, it offers the possibility for an integrated drive system controlling the deployment process.

The production of the bracing node prototype and its mechanical function is documented in Figures 110 to 112.



Figure 110: Telescopic vertical bracing rod. Expanded (left) and contracted (right)

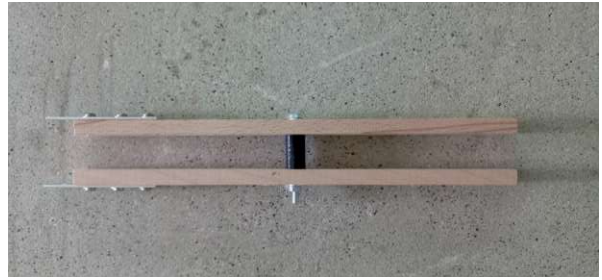
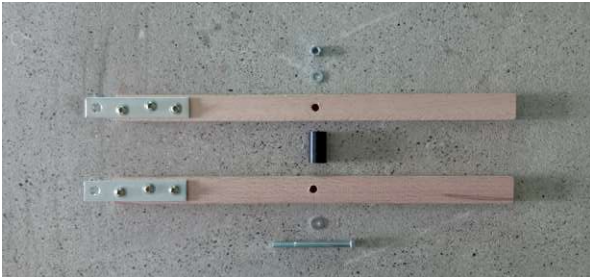


Figure 111: Scissor unit with end-lugs. Disassembled (left) and assembled (right).



Figure 112: Bracing node prototype. Contracted (left) and deployed (right).

5.3.2. Design challenges

Following the results of the structural analysis (Chapter 4) vertical bracing members are introduced, connecting the upper and lower nodes in certain points of the structure as determined by the process of a BESO optimization. As demonstrated on the prototype model, these bracing members will be designed in form of telescopic rods, consisting of multiple concentric circular sections, which will expand when the structure contracts and retract when the structure deploys. The length dimension of the telescopic sleeves will fix the structure at the determined thickness. The design in form of telescopic rods opens up the possibility to include in them an actuator system in form of a linear or a telescopic drive. In addition to the actuated telescopic bracing members, the node connectors also present a difficult design challenge.

In the structural model used for FE analysis in the previous chapter, the nodes were defined in form of circular hollow sections arranged crosswise, containing the axes connecting to the endpoints of the scissor bars, while allowing one degree of freedom, forming a revolute joint (Fig.113). In addition to linking the scissor endpoints, some of the nodes will also have to connect to the telescopic bracing members and tensile elements. The nodes lying at the points of support will also have to facilitate the anchoring of the structure. A further difficulty lies in the fact, that the axes of the nodes, connecting to the scissor endpoints, are generally not oriented orthogonally to each other. This presents a problem for fabrication, as it indicates that a high amount of node connectors will have to be custom-built.

Corresponding nodes of the upper and lower layer show the same angle configuration, with each pair rotated by 180° to each other. This reduces the number of custom nodes by half.

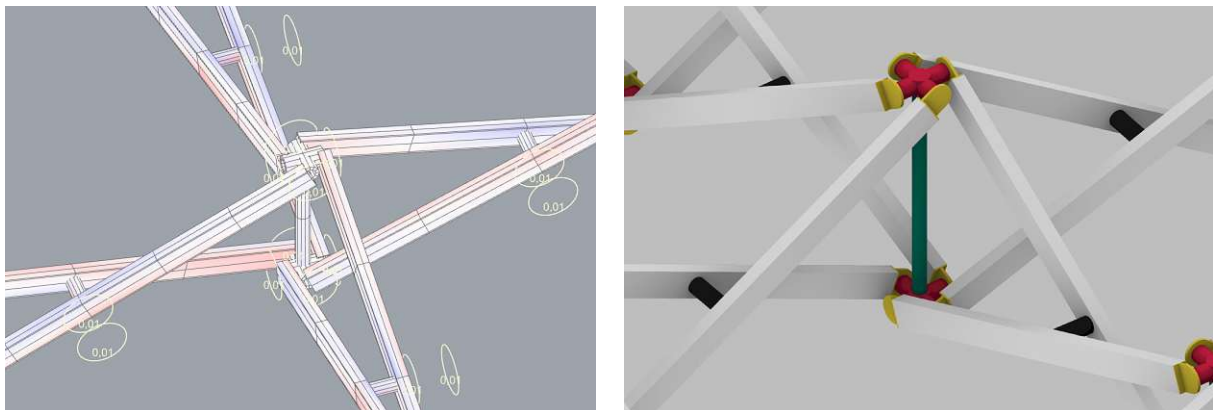


Figure 113: Node and hinge joints in the FE model (left) and in the detailed 3d model (right).

When considering the cross-vault structures presented in the previous chapter, there exist two axes of symmetry, resulting in four sets of identical node configurations. This further reduces the number of individual nodes by a quarter. Regarding the model “Cross-vault 20-12”, this leaves 43 parts to be custom-built. For “Cross-vault 14-11” the necessary amount of custom nodes is 36.

In the interest of cost-efficient fabrication, a rationalized design for the node connectors is desirable. With this intention, two design iterations for a node connector with variable axis orientation will be presented, along with design proposals for the telescopic bracing rods containing an actuated drive system.

5.3.3. Assembly using rationalized node connectors

A strategy for assembly of the structure using a rationalized node connector with variable angle configuration is illustrated on the model “Cross vault 14-11” in Figure 114.

Because of the two axes of symmetry and a quadrangular grid configuration, the modules running along the symmetry lines form rectangular linkages where the node connector can be placed in the standard 90° orientation. These modules will be assembled first (Fig. 114 a). Then, for each of the four identical corner patches, beginning at the already assembled interior corner and moving diagonally towards the perimeter, the remaining modules can be assembled (Fig. 114 b-e).

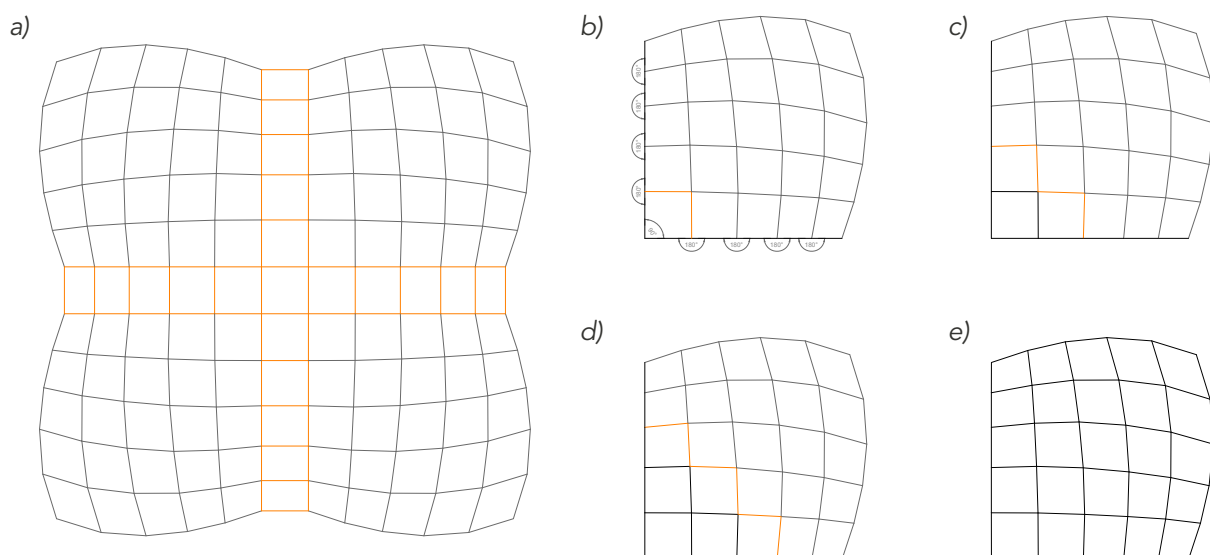


Figure 114: Assembly sequence using uniform node connector with variable axes.

The correct angle configuration will be determined by triangulation with the length of the connecting scissor bars. Once assembled the node connectors will be fastened with bolts to provide the necessary stiffness.

5.4. Node connector - Design A

The angles enclosed between adjoining node axes for “Cross vault 14-11” range from 90° to 56°. For “Cross-vault 20-12”, the angles range between 90° and 62°. This determines the necessary rotation range for designing a node connector with variable axis orientation.

The aim of rationalizing the node connector is to develop a design where each axis can be rotated continuously, within the necessary range defined above. Once the node connector is placed in position during assembly and the axes have been oriented correctly, the configuration will have to be fastened to provide the necessary stiffness. The vertical axis through the center of the node connector is kept hollow, as it will have to provide a connection for vertical bracing members, tensioning elements, and supports.

A first approach to solving this problem is illustrated by way of a section through the interior of the node connector in Figures 115 and 116. Each of the node axes lies in a sleeve which is connected to a radial bearing inside the node. This results in four radial bearings which are arranged concentrically around the center of the node. Guide rails, allowing the rotation of the bearings are connected to an upper and lower pressure plate forming two symmetrical caps for the node. Once the axes are oriented as needed, the caps are fastened by tensioning screws, thereby locking the sleeves in position between them.

Figures 117-119 show isometric views of the node connector geometry and assembly and Figures 120 and 121 document the fabrication of a 3D-printed scale prototype to test the design. While the necessary function of variable axis orientation is fulfilled, some areas of improvement are identified through this process.

The principle of connecting each axis to its individual bearing makes the design overly complicated, consisting of too many small parts, thereby calling into question the initial intent of efficiency through rationalization. This will be addressed in a second design proposal.

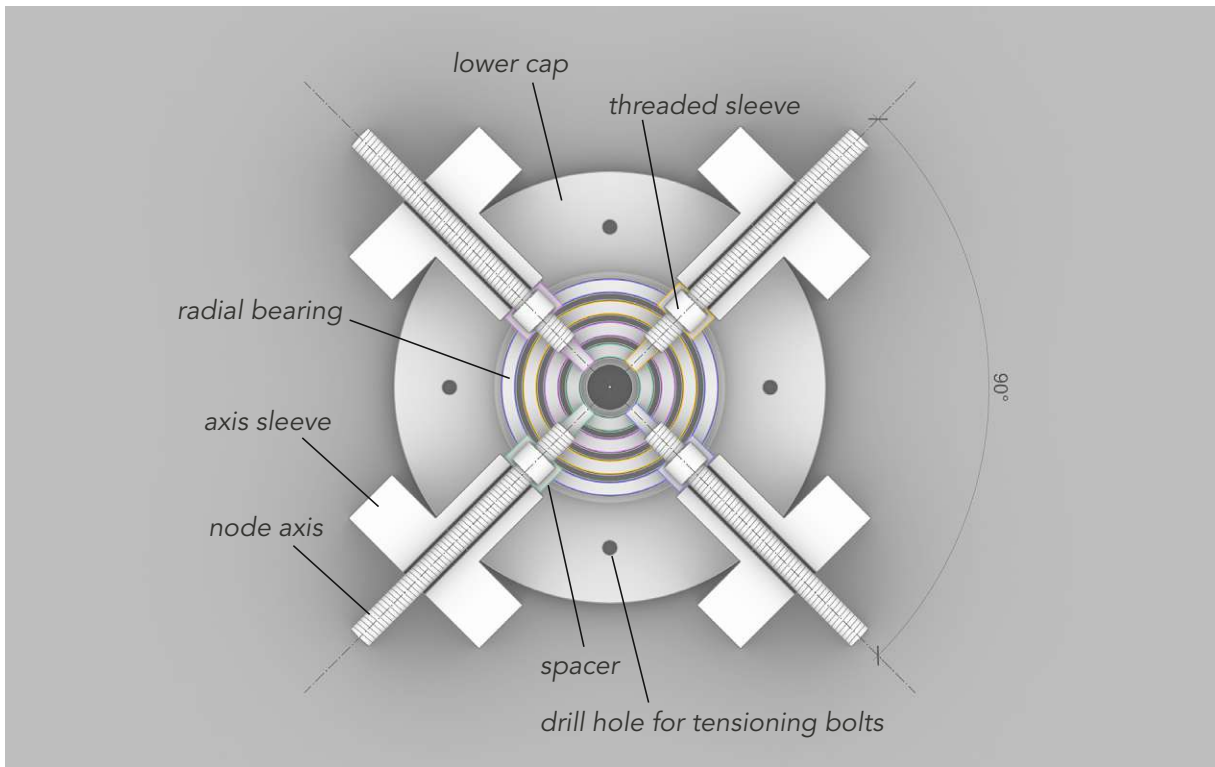


Figure 115: Horizontal section through node connector A, with standard 90° axis orientation.

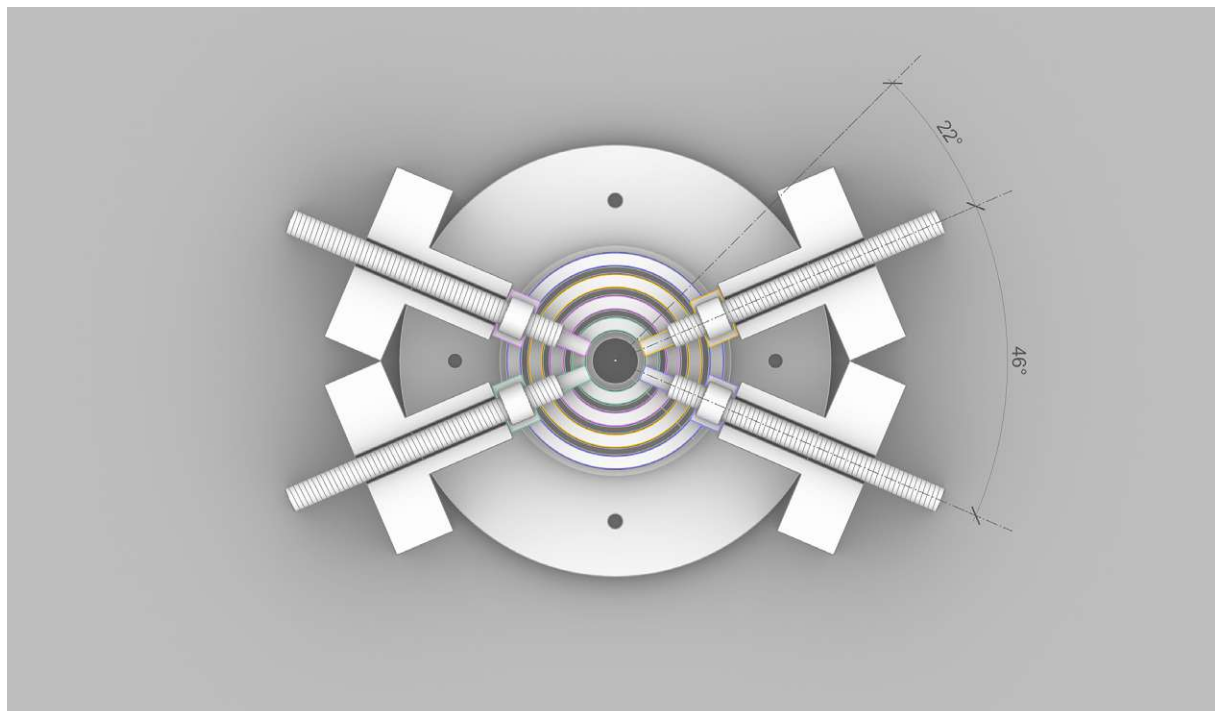


Figure 116: Horizontal section through node connector A, showing maximum rotation range.

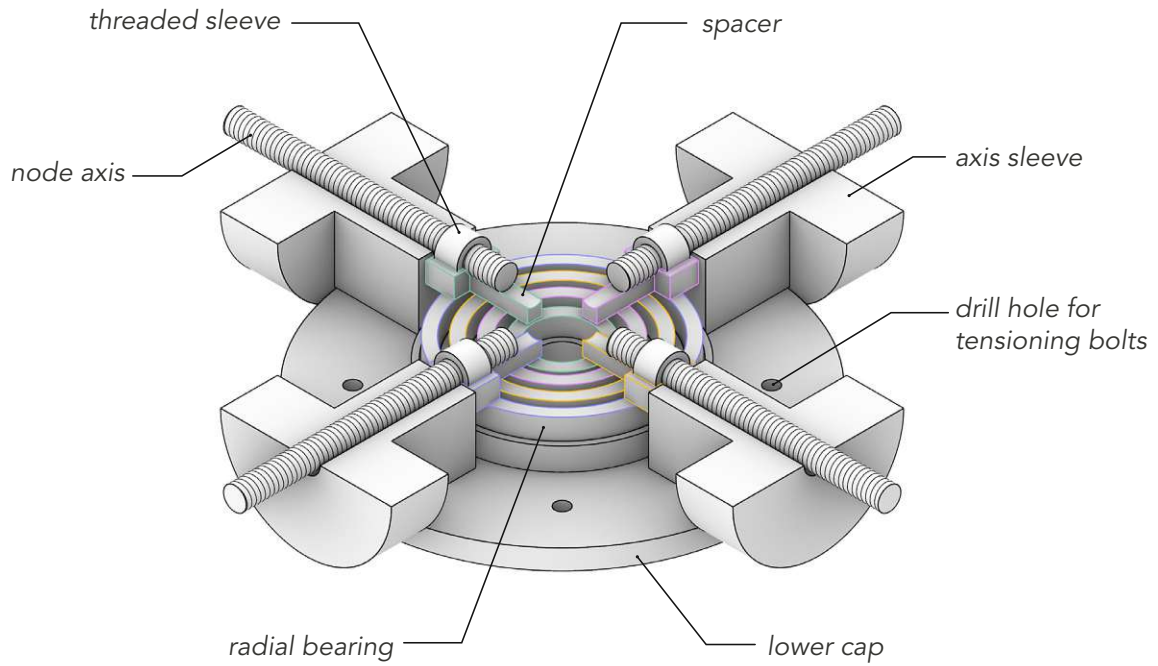


Figure 117: Isometric view of horizontal section through node connector, design proposal A.

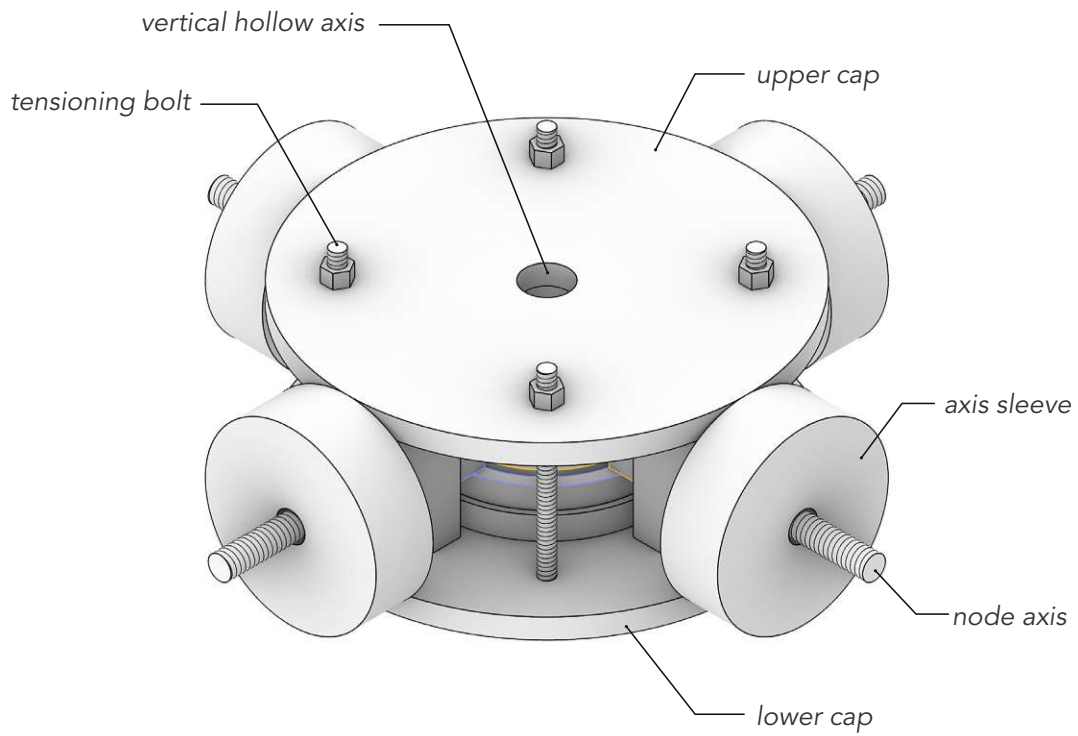


Figure 118: Isometric view of assembled node connector, design proposal A.

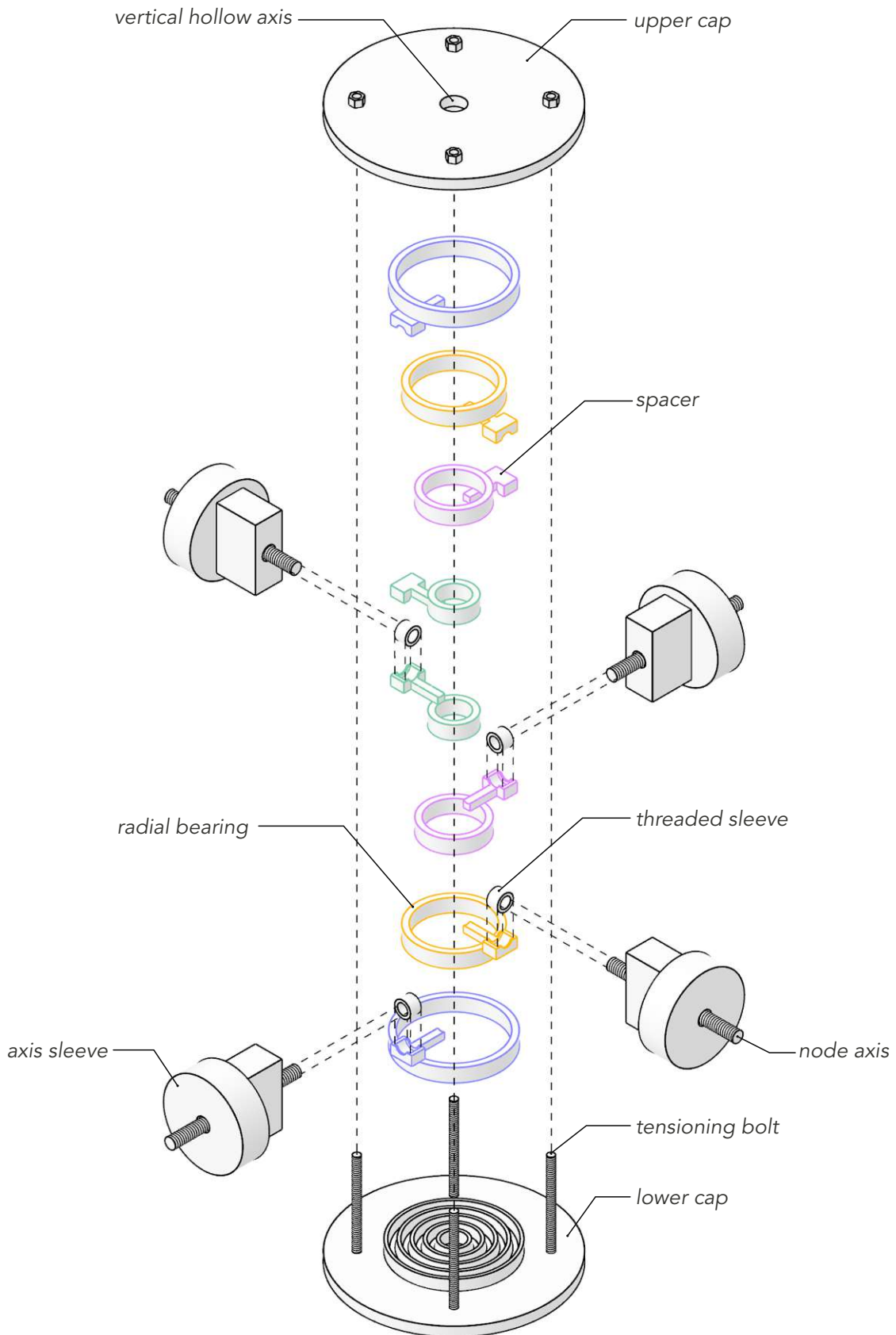


Figure 119: Exploded isometric view of node connector, design proposal A.



Figure 120: Node connector A. Assembly of a 3d printed, prototype.

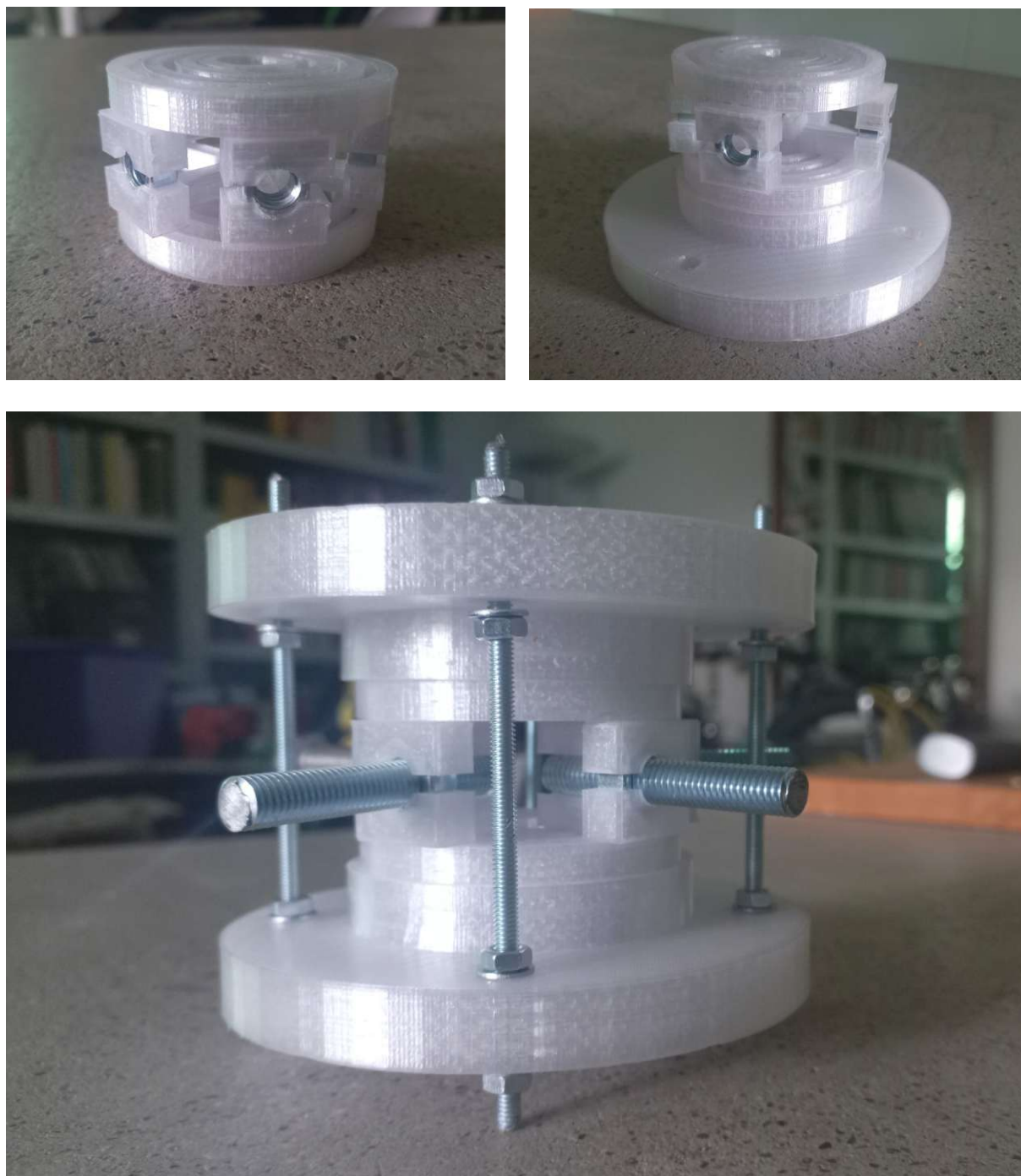


Figure 121: Node connector A, 3d printed prototype, interior parts and fully assembled component.

5.4.1. Vertical bracing members with a linear drive

In a first design approach for the telescopic, vertical bracing members the principle of a linear actuator is considered for an integrated drive system to operate the deployment process.

A mechanical linear actuator uses a simple principle to convert rotary motion, typically from an electric motor, into linear motion. It is commonly used in industrial machinery. Typically, the mode of operation involves a lead screw being rotated while a lead nut, connected to a sliding cylinder moves up along the lead. The sliding cylinder or piston is nested within a stationary shaft.

A sectional detail drawing for implementing such a principle within the vertical bracing members is shown in Figure 122. Depending on the force necessary to initiate the deployment process some of the bracing elements can include the drive system. The cylinder dimension is determined through the cross-section tables in chapter 4. Vertical bracing elements for “Cross-vault 14-11” are circular hollow sections CHS 60x6. For a standard linear actuator this results in telescopic rods, consisting of two pipes nested within each other with an outer diameter of 60 mm and a wall thickness of 3 mm for each.

The interior, sliding cylinder, carrying the lead nut, is connected to an upper node, while the exterior shaft is connected to a lower node. The leadscrew passes through the vertical hollow axis of the bottom node connector where an electric stepper motor inputs a rotary motion. Depending on the rotary direction, the upper node attached to the sliding cylinder moves towards the lower node during the deployment process, or it moves away when contracting the structure for storage. This way the vertical elements have the structurally necessary wall thickness when the structure is fully deployed and the telescopic rod is fully retracted.

This first approach is promising, but cannot sufficiently fulfill the design requirements. When consulting Table 14 (Section 4.2.5), listing simulation values for “Cross-vault 14-11”, it shows that the vertical distance between the upper and lower layer of nodes grows more than double in size when comparing the deployed state to the contracted state of the structure. The distance ranges from 60 cm when deployed, to 155 cm when contracted. This degree of expansion is not attainable by telescopic rods consisting of two nested pipes.

The linear actuator as described above will therefore not suffice. This fact will be addressed in a second design iteration for the system.

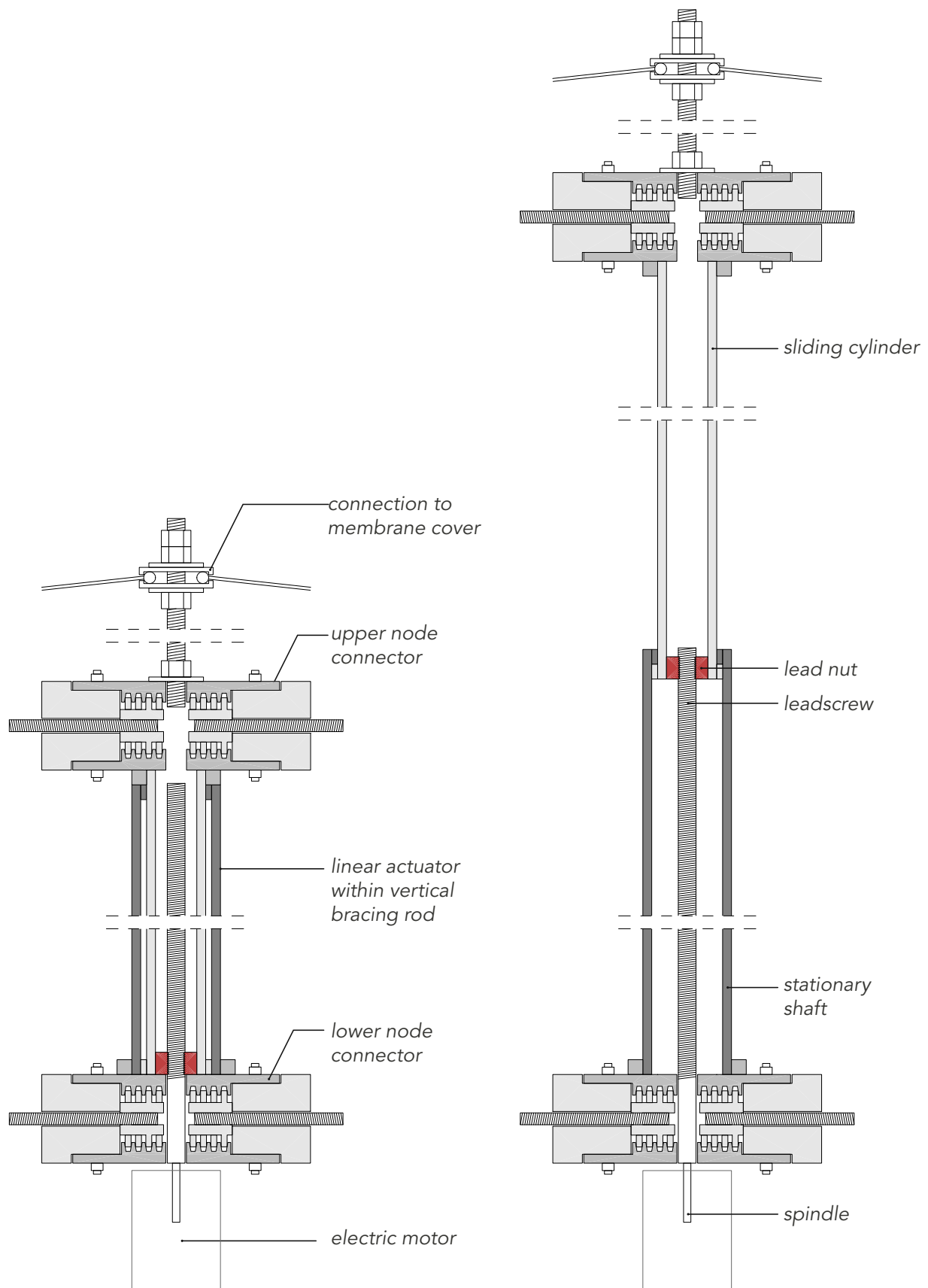


Figure 122: Section drawing through vertical bracing rods containing a linear drive system.

5.5. Node connector - Design B

In the interest of producing a more efficient component for batch fabrication, another design iteration is performed. For the second proposal, the aim is to simplify the node connector by reducing the number of parts while maintaining the functionality of the required features.

With this intention, the four individual radial bearings are replaced by a single guide rail running along the outer perimeter of the upper and lower cap. This guide rail corresponds to notches in the upper and lower surfaces of four sleeves containing the node axes. Along the rail, the notched sleeves can rotate continuously within the required angular range. The tensioning bolts fastening the node connector are running through the interior shaft of the axis sleeves, resulting in a more reliable locking mechanism.

Figures 123 and 124 show a horizontal section through the node connector while Figures 125-127 show isometric views.

For connecting vertical bracing elements, tensile elements and anchoring support points the vertical axis passing through the center of the node is left hollow, providing an interior thread that is useful for connecting to the other components. Detailed drawings of such connection points are presented in the next section.

5.5.1. Vertical bracing members with telescopic actuator

Telescoping linear actuators are specialized linear actuators used where space restrictions exist. Their range of motion can be many times greater than the length of the actuating member. A common form is made of concentric tubes of approximately equal length that extend and retract one inside each other.

In a telescopic cylinder, the largest diameter tube is called a barrel, while the interior tubes are called stages. A two-stage telescopic actuator consisting of three nested cylinders can expand to almost triple of its retracted length. In the case of a telescopic linear actuator, the spindle operated by the electric motor rotates the lead nut while the lead screw performs a linear motion along its axis without spinning. The lead nut operates the two stages by an interior and exterior thread. The interior thread is operating the movement of the leadscrew connected to the first stage, while the exterior thread operates the movement of the second stage.

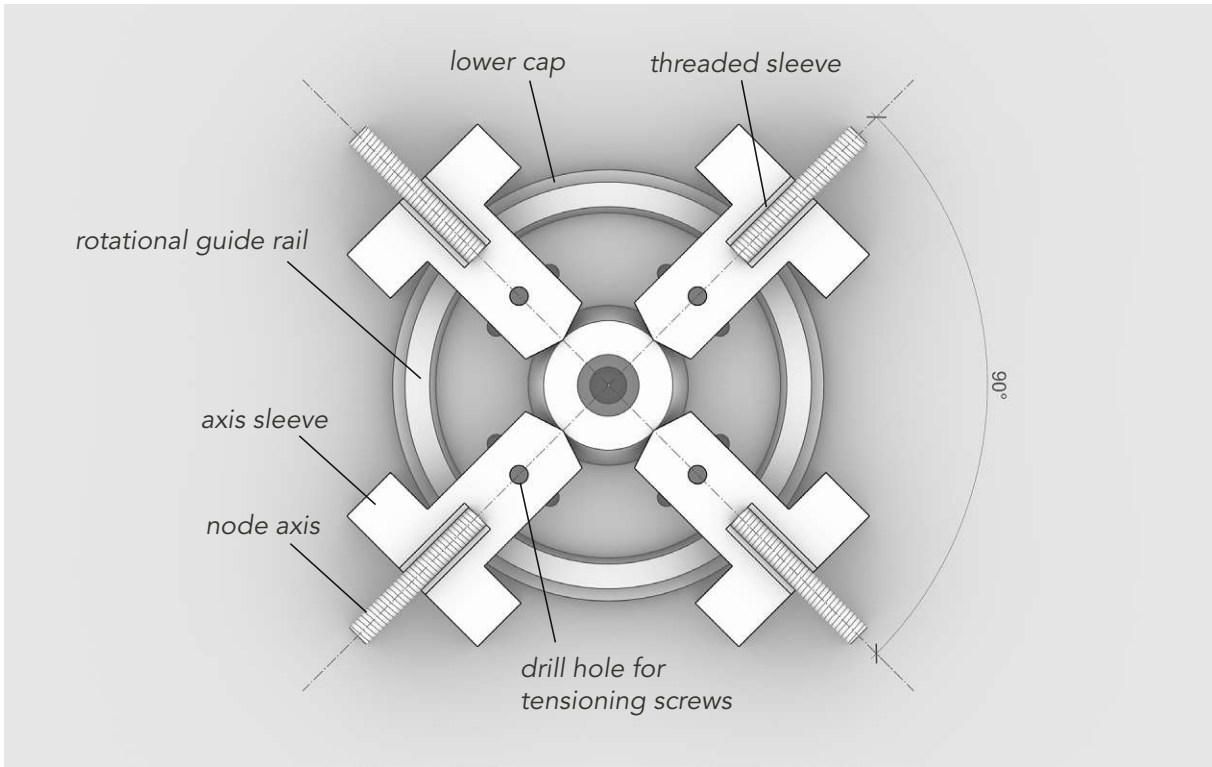


Figure 123: Horizontal section through node connector B, with standard 90° axis orientation.

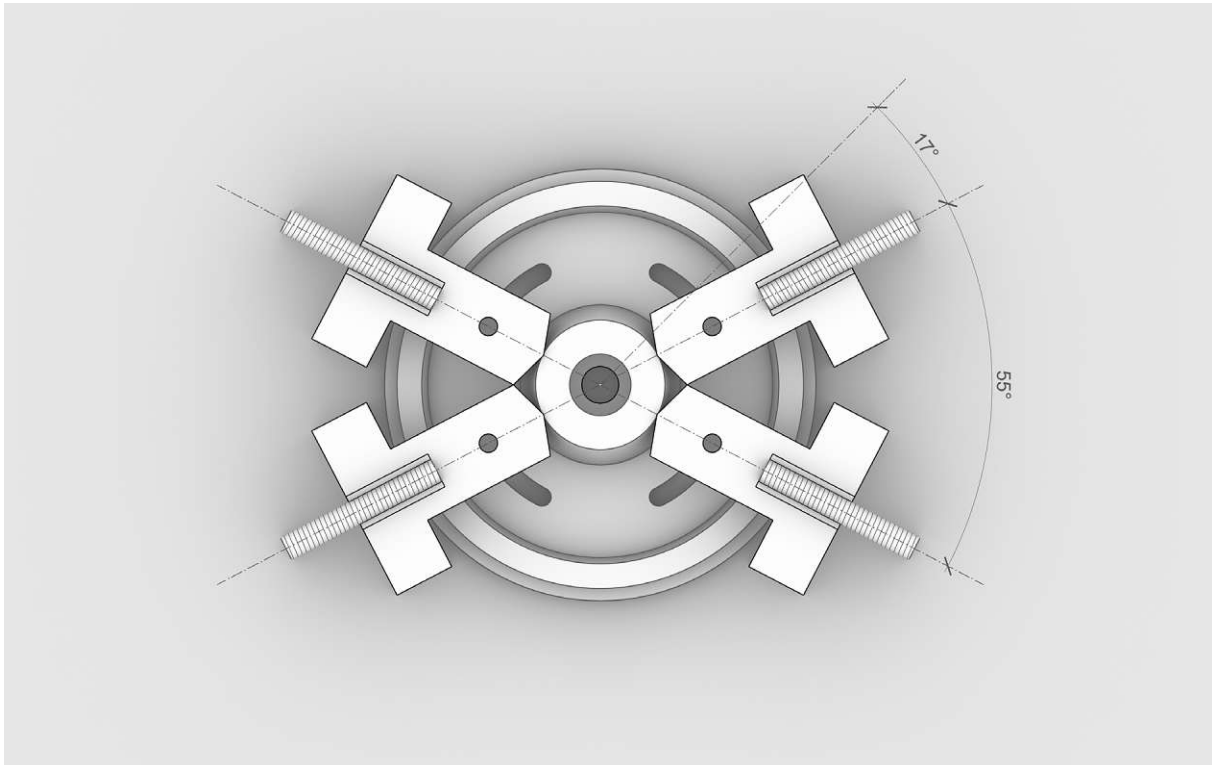


Figure 124: Horizontal section through node connector B, showing maximum rotation range.

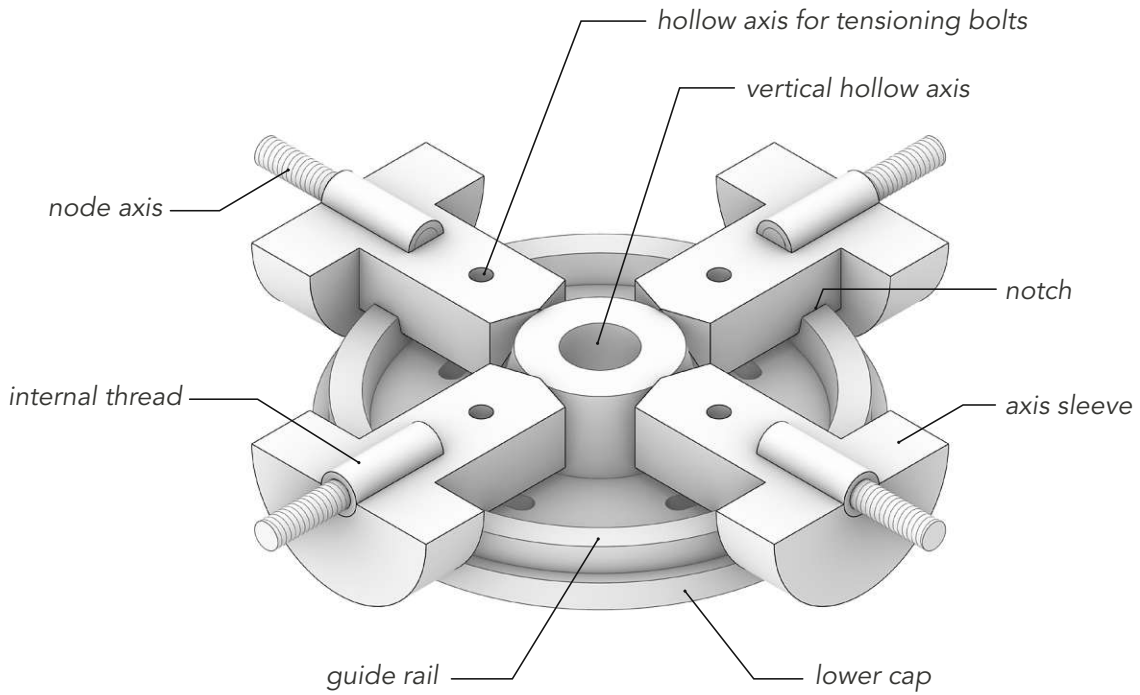


Figure 125: Isometric view of horizontal section through node connector, design proposal B.

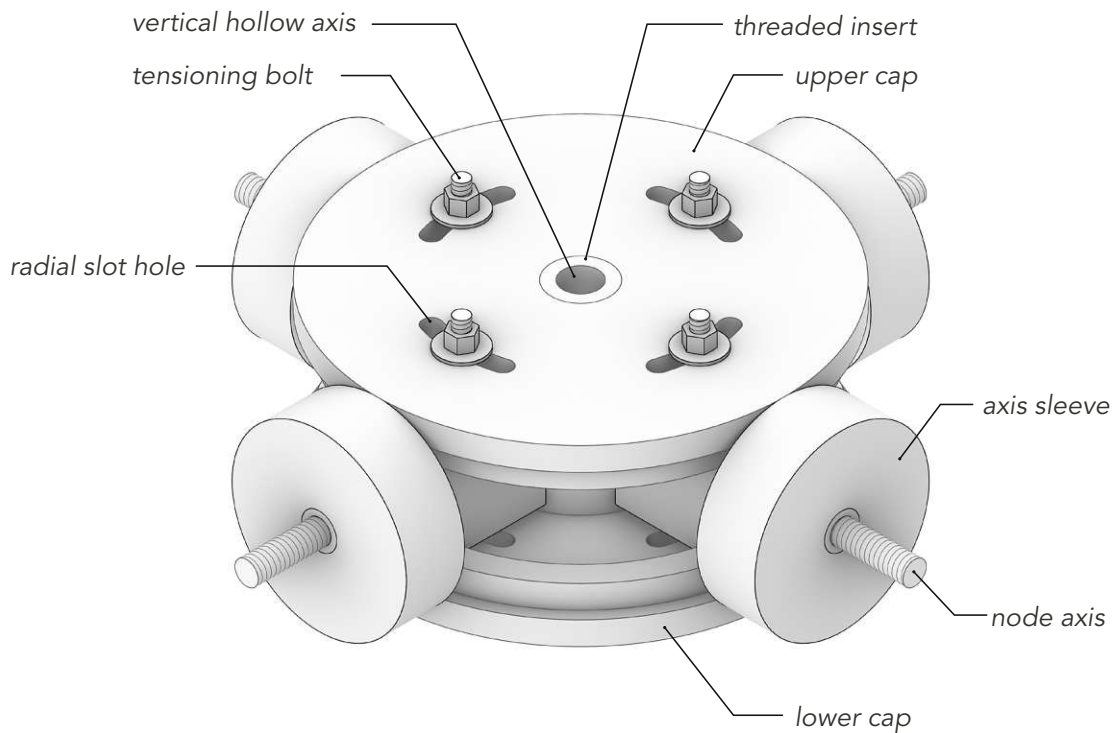


Figure 126: Isometric view of assembled node connector, design proposal B.

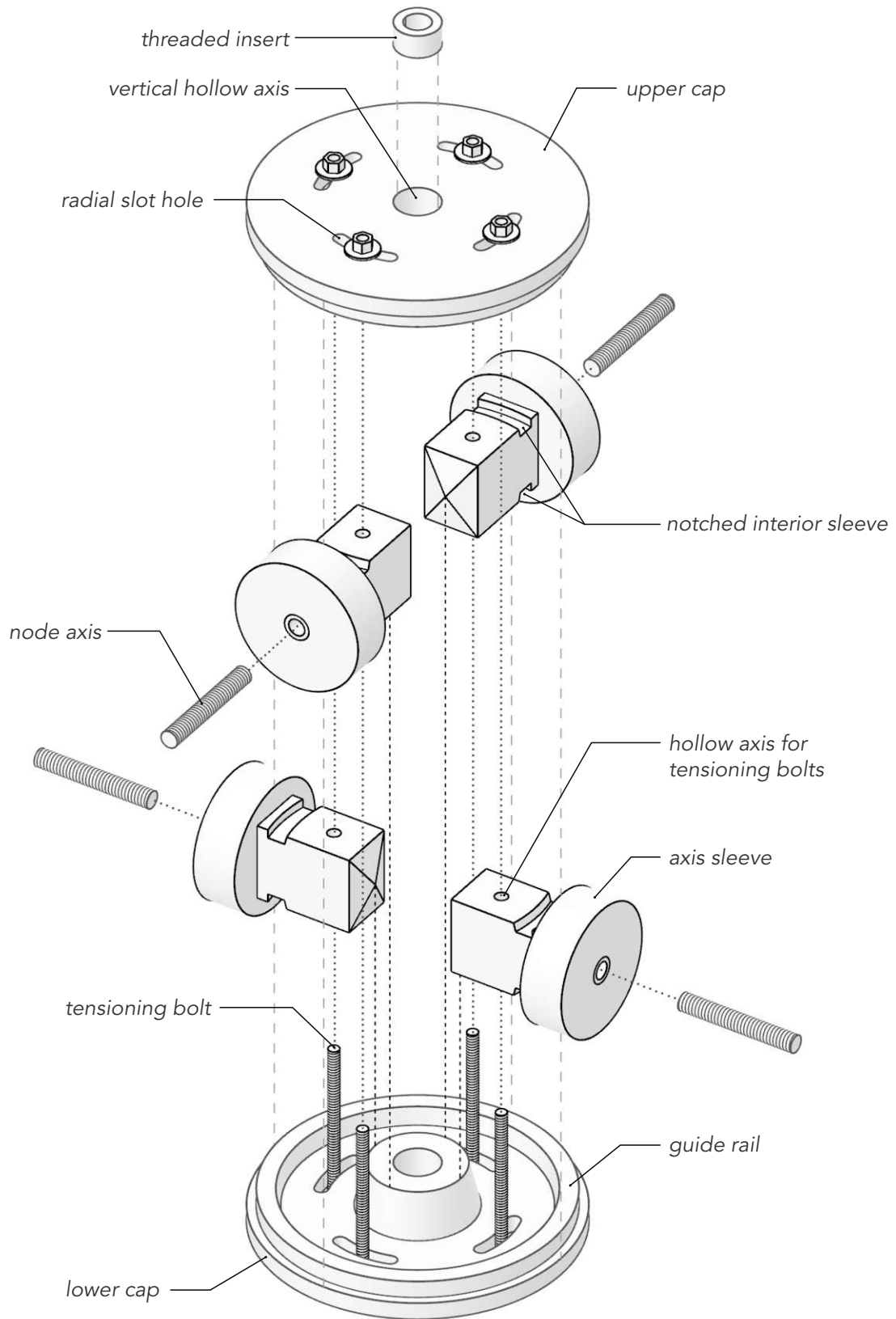
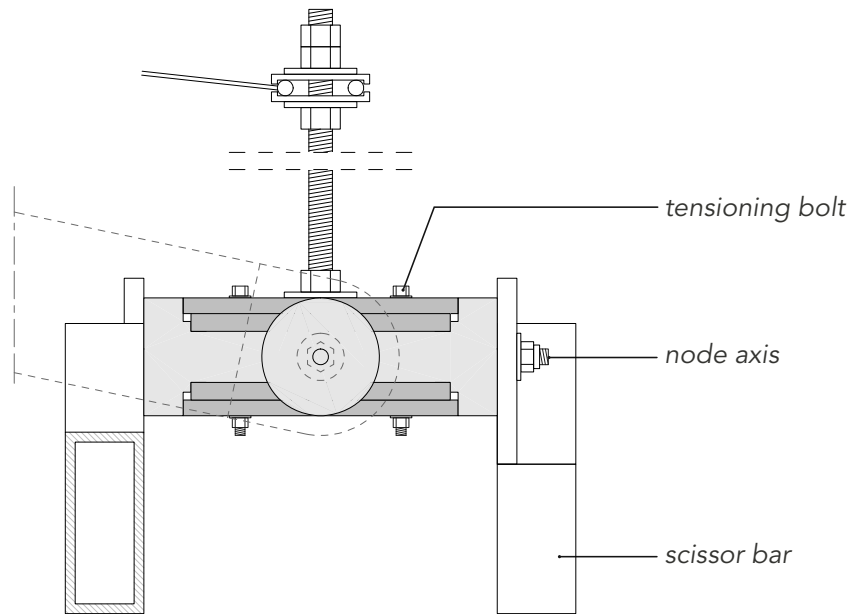


Figure 127: Exploded isometric view of node connector, design proposal B.

Figure 129 shows a section drawing through an upper and lower node of the second design connected by a vertical bracing member containing a two-stage telescopic actuator. Using a threaded insert into the vertical hollow axis of the upper node, the drawing also shows a way to attach to a membrane cover. The same principle applies in Figure 128, where the node's hollow axis is used to anchor the structure at its support points, by way of a threaded rod inserted into a prefabricated concrete foundation block, then secured by a nut and a locknut.

UPPER LAYER NODE



LOWER LAYER NODE

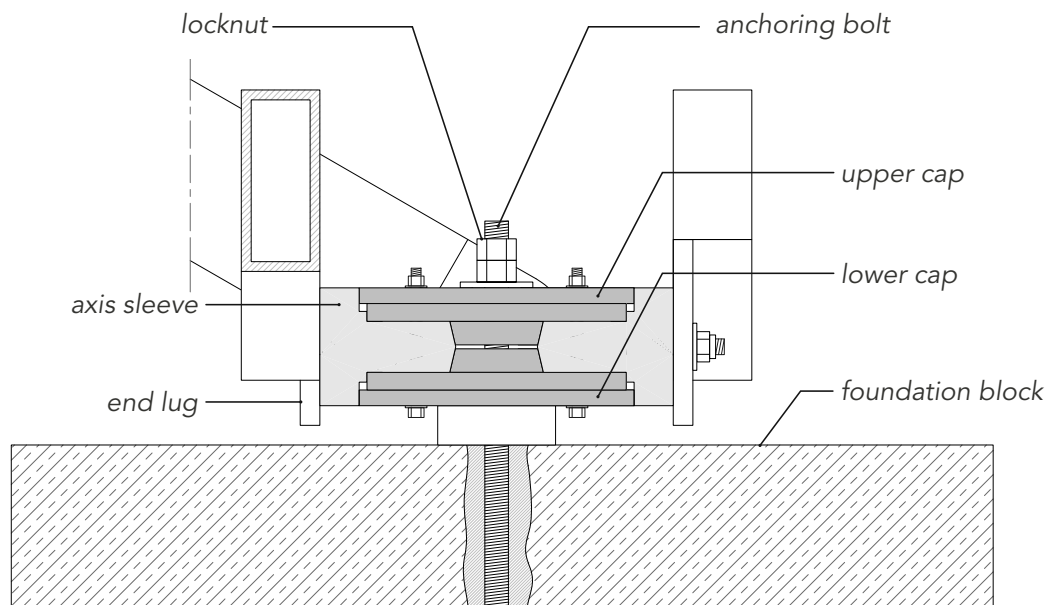


Figure 128: Sectional view. Upper and lower layer node connectors at one of the support points.

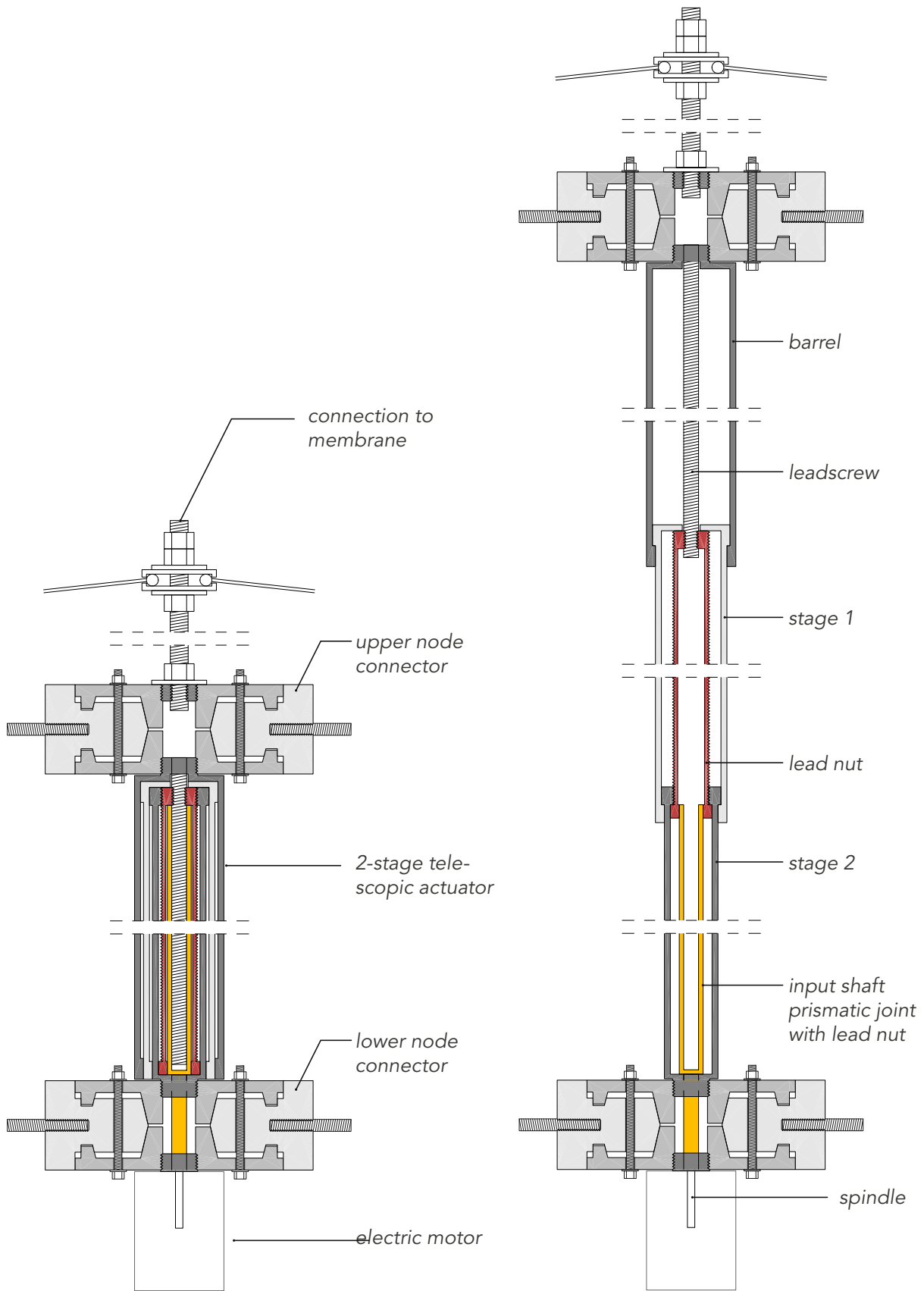


Figure 129: Section drawing through vertical bracing rods containing a telescopic linear actuator.

5.6. Visualization

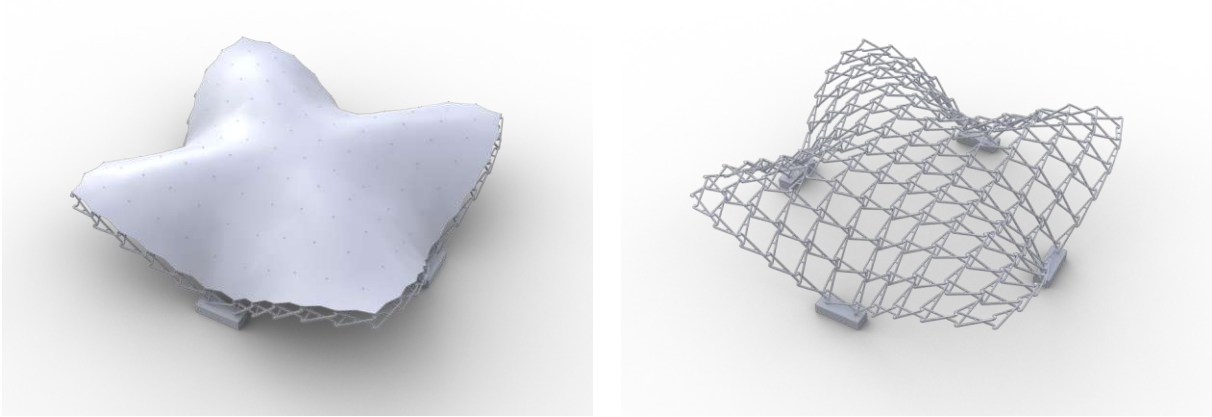


Figure 130: Detailed 3d model "Cross-vault 14-11", with membrane cover (left) and without (right)

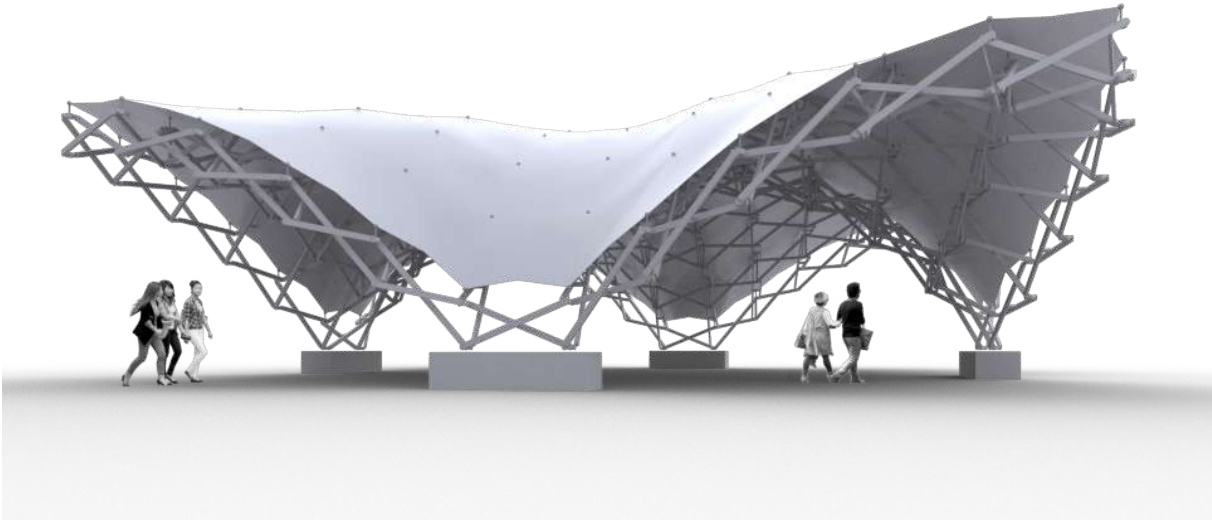


Figure 131: Detailed 3d model "Cross-vault 14-11", perspective view.



Figure 132: Visualization "Cross-vault 14-11".

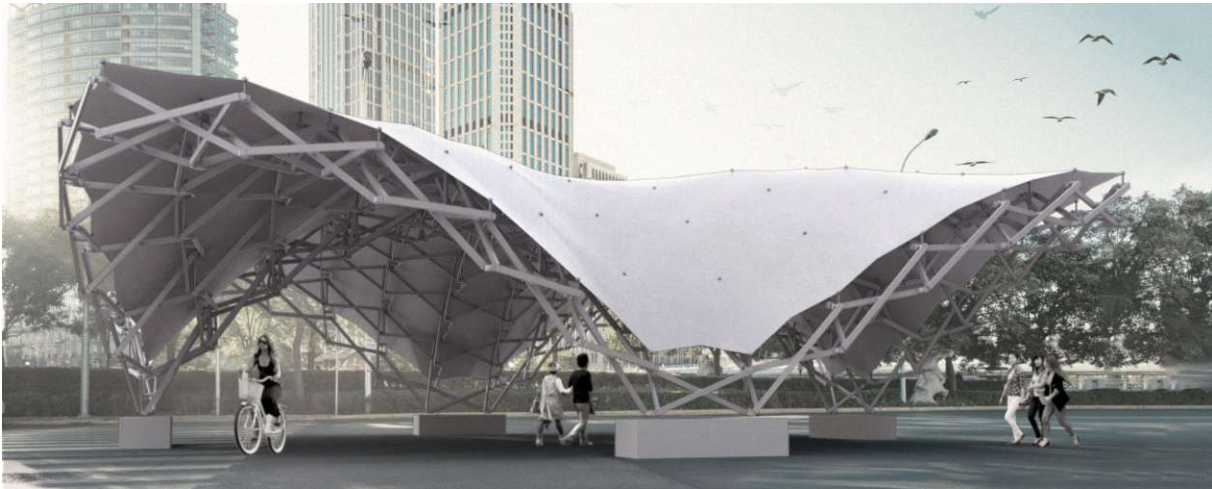


Figure 133: Visualization "Cross-vault 14-11".

6. CONCLUSION

The premise of this master thesis was to provide research and analysis on the topic of deployable scissor structures, in particular double-layer grids consisting of straight bars, and their potential use in the field of mobile, reusable, temporary, and transformable architecture.

Considering the complexity of design, construction, fabrication, and assembly, resulting from the kinematic requirements and related to the geometric properties of such structures, an important factor for this analysis was the utilization of parametric design environments, and computational models for form-finding, physical simulation, and structural analysis.

The first part of this thesis provides a detailed review of different configurations for deployable scissor grids, explains common terminology and classification, and describes geometric constraints and construction methods for deployable scissor grids. Prominent researchers in the field are presented along with examples of their proposed and realized designs.

The next part presents established design methods along with their implementation within Rhino3D and Grasshopper, for the parametric design of several expandable grid configurations and the interactive simulation of the deployment process. As a result of these digital experiments, a novel approach to designing geometrically compatible deployable scissor grids, consisting of translational units is developed. The proposed form-finding tool is based on mesh relaxation using the topology of a cyclic quad and proves to be a suitable strategy for designing deployable grids on surfaces of more versatile shape, than the initially reviewed flat, spherical, or cylindrical configurations.

For the next part, two typologies of large-scale deployable grids are generated using the aforementioned form-finding tool. The two typologies are a cross-vault and a hyperbolic barrel vault. Using these typologies three configurations are modeled in detail to be used as case studies for structural analysis and optimization using the FE method within Karamba3d. The resulting grid configurations, fulfilling structural and kinematic requirements, are then subjected to a simulation of the deployment process using the live-physics engine Kangaroo2, providing information on the deployment factor, volume expansion ratio, and storage size of a given structure.

The final chapter dedicates itself to the development of a strategy for the fabrication, assembly, and installation of a mobile deployable scissor grid at such a scale and configuration. In the interest of eliminating the need for small batch production of custom building components

two design iterations for the proposal of a rationalized node connector with variable axis orientation are presented. In addition to a more cost-efficient fabrication process, the use of a uniform component design for the node connector reduces the risk of error during assembly. A strategy for assembly is presented alongside.

In addition to detailing a solution for the node connector, its connection points to a membrane cover and the structure's anchoring support points are considered. For controlling the deployment process, the integration of a two-stage telescopic actuator within the structure's vertical bracing elements is considered in detail.

In conclusion, the process of designing a well-balanced deployable scissor grid, including efficient structural performance and deployment behavior, at a large scale requires a lot of consideration of the factors of shape, span, height, grid resolution, and topology and distribution of bracing elements and supports. Computational models and programming environments, which are widely used in architecture and engineering today, offer accessible means to handle the complexity of this design process. The resulting deployable grids show a stress-free deployment behavior, a reliable mechanism, and are very lightweight.

Architectural applications can range from temporary building structures for commercial or recreational use, such as sporting events, festivals, or exhibitions, to fixed location structures like temporary roofs, canopies, or transformable building extensions and envelopes. Design and production, however, entail a high investment for material and fabrication, which will have to be justified by a building application demanding frequent deployment over a long lifespan.

7. BIBLIOGRAPHY

Asefi, M. & Kronenburg, R., 2006. An Architectural Evaluation of Transformable Roof Structures. Eindhoven, University Eindhoven, pp. 6-85.

Hoberman Associates, 1993. Iris Dome working scale model. Chuck Hoberman Fonds. Canadian Centre for Architecture, Montréal. [online] <https://www.cca.qc.ca/en/search/details/collection/object/431847> [abgerufen am 27.03.2023]

De Temmerman, N., 2007. Design and Analysis of Deployable Bar Structures for Mobile Architectural Applications. Brussels: Vrije Universiteit Brussel.

Escrig, F., 1985. Expandable space structures. *Space Structures Journal*, 1(2), pp. 79-91.

Escrig, F., 2013. Emilio Pérez Piñero: Inventor of Deployability. In: P. Cruz, Hrsg. *Structures and Architecture*. Seville: CRC Press.

Escrig, F. & Pérez-Valcárel, J., 1993. Geometry of Expandable Space Structures. *International Journal of Space Structures*, 8(1/2), pp. 127-134.

Fenci, G. E. & Currie, N. G., 2017. Deployable structures classification: A review. *International Journal of Space Structures* 32(2), pp. 112-130.

Gantes, C. J., 2001. *Deployable Structures Analysis and Design*. Southampton, UK: WIT Press.

Gengnagel, C. & Burford, N., 2006. *Transformable Structures for Mobile Shelters*. Eindhoven, University Eindhoven, pp. 10-280.

Hanaor, A. & Levy, R., 2001. Evaluation of Deployable Structures for Space Enclosures. *International Journal of Space Structures*, Vol. 16, No. 4, p. 211-229.

Jensen, F. V., 2004. *Concepts for retractable roof structures*. Cambridge: University of Cambridge.

Langbecker, T. & Albermani, F., 2000. Foldable positive and negative curvature structures: Geometric design and structural response. *Journal of the International Association for Shell and Spatial Structures*. 41, pp. 147-161..

Marshall, B. & Eppstein, D., 1999. Quadrilateral Meshing by Circle Packing. *International Journal of Computational Geometry and Applications* 10.

Martín-Gutiérrez, E. & Pérez-Valcárcel, J., 2002. Generation of foldable domes formed by bundle modules with quadrangular base. *Journal of the International Association for Shell and Spatial Structures*, 43(140), pp. 133-141.

Pellegrino, S., 2001. *Deployable Structures*. New York: Springer-Verlag.

Ródenas-López, M., Peña Fernández-Serrano, M. & Jiménez-Vicario, P., 2020. Geometric Evaluation of Deployable Structures Using. *Nexus Network Journal*, p. 247–270.

Roovers, K. & De Temmerman, N., 2014. A classification of singly curved deployable scissor grids. *Brasilia, R. Brasil & R. Pauletti*.

Roovers, K. & De Temmerman, N., 2015. Digital design of deployable scissor grids based on circle packing. *Amsterdam, IASS*.

Roovers, K. & De Temmerman, N., 2017. Deployable scissor grids consisting of translational units. *International Journal of Solids and Structures*, pp. 45-61.

Sanchez, J., Escrig, F. & Pérez-Valcárcel, J., 1996. The adventure of covering a swimming-pool with an X-frame structure. *WIT Transactions on The Built Environment: Mobile and Rapidly Assembled Structures II*, Band 24, pp. 113-122.

Zuk, W. & Clark, R., 1970. *Kinetic Architecture*. New York: Van Nostrand Reinhold Press.

8. FIGURES

Figure 1: Examples of deployable structures (Zuk & Clark, 1970)

Figure 2: Classification of structural systems for deployable structures by their morphological and kinetic characteristics As in Hanaor & Levy (2001).

Figure 3: Most common types of scissor units consisting of straight or angulated bars.

Figure 4: a) Composition of a scissor unit illustrated on a regular plane-translational unit. b) Triangular module, consisting of a linkage of three plane-translational units arranged to form a closed loop.

Figure 5: Linkage of three regular plane-translational units, shown in two stages of deployment.

Figure 6: Linkage of three regular curved-translational units, shown in two stages of deployment.

Figure 7: a) A linkage of polar units forming an arc is shown in two stages of deployment. b) Composition of a regular polar unit.

Figure 8: Illustration of a) single-layer and b) double-layer grid configuration.

Figure 9: Illustration of Escrig's deployability constraint shown on two adjoining irregular scissor units in four stages of deployment.

Figure 10: Angulated unit and geometric compatibility. Illustration of radial deployment.

Figure 11: Iris Dome, working scale model (Hoberman Associates, 1993).

Figure 12: a) and b) Deployment process of multiple planar scissor grids build for a mobile exhibition pavilion. c) Lifting and interconnecting the individual grids to form a structure covering a total area of 8000 square meters. d) Fully deployed and installed roof structure (Escrig, 2013).

Figure 13: Top view and side elevation of an a) two-way spherical grid b) three-way spherical grid and c) lamella dome composed of polar units (Escrig & Pérez-Valcárel, 1993).

Figure 14: Cover for the municipal swimming pool of San Pablo Sports Centre in Seville.

Figure 15: a) Fully contracted structure. b) Deployment process. c) Interior view when fully installed.

Figure 16: a) Anchoring detail. b) Linkage detail. c) Hingepoint detail.

Figure 17: Translational scissor grids with positive and negative gaussian curvature in two deployment stages (Langbecker & Albermani, 2000)

Figure 18: Square and hexagonal circle packing and the resulting 2-way and 3-way grid, as in Roovers & De Temmerman (2015)

Figure 19: Populating three tangent circles by polar units. As in Roovers & De Temmerman (2015)

Figure 20: Generating prismatic scissor modules by mesh face. Vertices and offset vectors are sorted, offset, and connected to form endpoints of the scissor units.

Figure 21: Grasshopper definition for generating prismatic scissor modules by mesh face.

Figure 22: Modelling prismatic scissor modules on quadrangular mesh faces. Vertices are sorted counterclockwise; the orientation of the offset vectors flips.

Figure 23: Modelling scissor linkages along a UV network. Offset vectors are oriented in a uniform direction.

Figure 24: Simulation parameters: Angle between outer layer semi-lengths a_1 and a_2 and inner layer semi-lengths b_1 and b_2 serves as a variable for deployment. Additional constraints are to keep all bars same length and to keep line-segments antiparallel (straight).

Figure 25: Deployment simulation setup; initial angle between semi-lengths is measured in completely deployed state ($c = 0$) and can be varied to a degree where all the bars are aligned and the grid is theoretically reduced to a single line ($c = 1$).

Figure 26: 3v geodesic dome with the corresponding pattern of tangential circles. The mesh is populated with polar scissor units and illustrated in three stages of deployment.

Figure 27: Uniform rhomboid spherical dome with the corresponding pattern of tangential circles. The mesh is populated with identical polar scissor units and illustrated in three stages of deployment.

Figure 28: Grasshopper definition of mesh topology optimization to hold a circle packing where the vertices are at the center points of the tangential circles using Kangaroo2.

Figure 29: Spherical dome with triangulation based on circle packing I. The mesh is populated with polar scissor units and illustrated in three stages of deployment.

Figure 30: Near equilateral triangular mesh topology optimization to hold a dense circle packing using Kangaroo2.

Figure 31: Spherical dome with triangulation based on circle packing II. The base mesh is populated with polar scissor units and illustrated in three stages of deployment.

Figure 32: Cylindrical vault consisting of uniform polar and plane-translational scissor units, resulting in stress-free deployment behavior, illustrated in three states of deployment.

Figure 33: Translational surface with double-curvature, uniform rhomboid subdivision pattern, populated with curved-translational units. Three stages of deployment, completely stress-free.

Figure 34: GH Definition for a mesh relaxation into a cyclic quad.

Figure 35: Mesh relaxation of a flat grid with four anchor points into a cyclic quad mesh. Illustration of resulting cross-vault geometry.

Figure 36: Translational scissor grid based on cyclic quad mesh relaxation in the shape of a cross-vault. Three stages of deployment.

Figure 37: Detailed 3D model including scissor bars with end-lugs, hinges, nodes, and vertical bracing rods.

Figure 38: Form-finding, optimization, and simulation workflow.

Figure 39: Line model of the base grid geometry for "Cross-vault 20-12".

Figure 40: Loads acting on the structural model for "Cross-vault 20-12". LC 0 (left) and LC 1 (right).

Figure 41: BESO optimization on the number of vertical bracing rods for "Cross-vault 20-12". Of 169 rods in the initial model, 92 remain, 77 are not utilized.

Figure 42: Color-coded cross-sections for "Cross-vault 20-12", as referenced in Table 9.

Figure 43: Initial model "Cross-vault 20-12" for LC0. Utilization ranges between -55.1% and 75.3%.

Figure 44: Initial model "Cross-vault 20-12" for LC0. Maximum displacement of 5.67 cm.

Figure 45: Initial model "Cross-vault 20-12" for LC1. Utilization ranges between -69.1% and 71.6%.

Figure 46: Initial model "Cross-vault 20-12" for LC1. Max. displacement of 8.21 cm.

Figure 47: Utilization of "Cross-vault 20-12" for LC 0 after BESO optimization on the number of the vertical bracing members ranges between -56.1% and 68.8%.

Figure 48: Displacement of "Cross-vault 20-12" for LC 0 after BESO optimization on the number of the vertical bracing members. Max. displacement of 9.96 cm.

Figure 49: Utilization of "Cross-vault 20-12" for LC 1 after BESO optimization on the number of the vertical bracing members ranges between -74.4% and 76.5%.

Figure 50: Displacement of "Cross-vault 20-12" for LC 1 after BESO optimization on the number of the vertical bracing members. Max. displacement of 11.9 cm.

Figure 51: Utilization of "Cross-vault 20-12" for LC 0 after cross section optimization targeting the wall thickness of the scissor bars ranges between -70.1% and 72.4%.

Figure 52: Displacement of "Cross-vault 20-12" for LC 0 after cross section optimization targeting the wall thickness of the scissor bars. Max. displacement of 15.5 cm.

Figure 53: Utilization of "Cross-vault 20-12" for LC 1 after cross section optimization targeting the wall thickness of the scissor bars ranges between -79.5% and 81.7%.

Figure 54: Displacement of "Cross-vault 20-12" for LC 1 after cross section optimization targeting the wall thickness of the scissor bars. Max. displacement is 18.3 cm.

Figure 55: Deployment simulation for "Cross-vault 20-12" at two stages of deployment. Fully deployed structure (left) and maximum contraction (right).

Figure 56: Line model of the base grid geometry for Cross-vault 14-11.

Figure 57: Loads acting on the structural model for "Cross-vault 14-11". LC 0 (left) and LC 1 (right).

Figure 58: BESO optimization on the number of vertical bracing rods for "Cross-vault 14-11". Of 144 rods in the initial model (left), 57 remain, 87 are not utilized (right).

Figure 59: Color-coded cross-sections for "Cross-vault 14-11" as referenced in Table 13.

Figure 60: Initial model "Cross-vault 14-11" for LC 0. Utilization ranges between -45.1% and 79.3%.

Figure 61: Initial model "Cross-vault 14-11" for LC 0. Maximum displacement of 3.98 cm.

Figure 62: Initial model "Cross-vault 14-11" for LC 1. Utilization ranges between -56.5% and 60.9%.

Figure 63: Initial model "Cross-vault 14-11" for LC 1. Maximum displacement of 5.09 cm.

Figure 64: Utilization of "Cross vault 14-11" for LC 0 after BESO optimization on the number of the vertical bracing members, ranges between -51.3% and 78.2%.

Figure 65: Displacement of "Cross vault 14-11" for LC 0 after BESO optimization on the number of vertical bracing members. Max. displacement of 7.50 cm.

Figure 66: Utilization of "Cross vault 14-11" for LC 1 after BESO optimization on the number of the vertical bracing members, ranges between -68.3% and 69.4%.

Figure 67: Displacement of "Cross vault 14-11" for LC 1 after BESO optimization on the number of vertical bracing members. Max. displacement of 8.79 cm.

Figure 68: Utilization of "Cross vault 14-11" for LC 0 after cross-section optimization targeting the wall thickness of the scissor bars ranges between -64.4% and 80%.

Figure 69: Displacement of "Cross vault 14-11" for LC 0 after cross-section optimization targeting the wall thickness of the scissor bars. Max. displacement of 10.21 cm.

Figure 70: Utilization of "Cross vault 14-11" for LC 1 after cross-section optimization targeting the wall thickness of the scissor bars ranges between -70.5% and 71.7%.

Figure 71: Displacement of "Cross vault 14-11" for LC 1 after cross-section optimization targeting the wall thickness of the scissor bars. Max. displacement of 12.21 cm.

Figure 72: Deployment simulation for "Cross-vault 14-11" at two stages of deployment. Fully deployed structure (left) and maximum contraction (right).

Figure 73: Line model of the base grid geometry for "Barrel-vault 12-10".

Figure 74: : Loads acting on the structural model for "Barrel-vault 12-10". LC 0 (left), LC 1 (right)

Figure 75: Result of BESO optimization on the number of vertical bracing rods for "Barrel vault 12-10". Of 121 rods in the initial model (left), 47 remain, 74 are not utilized (right).

Figure 76: Color-coded cross sections, as referenced in Tab. 17 for "Barrel-vault 12-10".

Figure 77: Initial model "Barrel-vault 12-10" for LC 0. Utilization ranges between -40.9% and 56.1%.

Figure 78: Initial model "Barrel-vault 12-10" for LC 0. Maximum displacement of 5.24 cm.

Figure 79: Initial model "Barrel-vault 12-10" for LC 1. Utilization ranges between -51.8% and 60.1%.

Figure 80: Initial model "Barrel-vault 12-10" for LC 1. Maximum displacement of 10.33 cm. .

Figure 81: Utilization of "Barrel-vault 12-10" for LC 0 after BESO optimization on the number of the vertical bracing members, ranges between -69.2% and 63.3%.

Figure 82: Displacement of "Barrel-vault 12-10" for LC0 after BESO optimization on the number of vertical bracing members. Max. displacement of 21.54 cm.

Figure 83: Utilization of "Barrel-vault 12-10 " for LC 1 after BESO optimization on the number of the vertical bracing members, ranges between -70.8% and 64.7%.

Figure 84: Displacement of "Barrel-vault 12-10" for LC1 after BESO optimization on the number of vertical bracing members. Max. displacement of 24.18 cm.

Figure 85: Utilization of "Barrel-vault 12-10" for LC 0 after cross-section optimization targeting the wall thickness of the scissor bars ranges between -70.6% and 73.0%.

Figure 86: Displacement of "Barrel-vault 12-10" for LC 0 after cross-section optimization Max. displacement of 29.34 cm.

Figure 87: Utilization of "Barrel-vault 12-10" for LC 1 after cross-section optimization targeting the wall thickness of the scissor bars ranges between -67.5% and 72.3%.

Figure 88: Displacement of "Barrel-vault 12-10" for LC 1 after cross-section optimization targeting the wall thickness of the scissor bars. Max. displacement of 33.27 cm.

Figure 89: Deployment simulation for "Barrel-vault 12-10" at two stages of deployment. Fully deployed structure (left) and maximum contraction (right).

Figure 90: Node detail Prototype B.

Figure 91: Extracted patch for prototype A. Three by three modules located at one of the raised corners of the structure.

Figure 92: Extracted patch for prototype B. Four by four modules located at one of the support points of the structure.

Figure 93: Prototype A, labeling for fabrication and assembly.

Figure 94: Prototype B, detailed model.

Figure 95: Nested and labeled scissor bars for milling.

Figure 96: CNC milling of scissor bars.

Figure 97: Scissor bars for assembly.

Figure 98: 3d printed node-connector.

Figure 99: Disassembled scissor unit.

Figure 100: Assembled scissor unit, closed.

Figure 101: Assembled scissor unit, open.

Figure 102: Prototype A, contracted.

Figure 103: Prototype A, deployed.

Figure 104: Prototype B, contracted.

Figure 105: Prototype B, deployed.

Figure 106: Prototype B, close-up, contracted.

Figure 107: Prototype B, deployed.

Figure 108: Prototype B, close-up, deployed.

Figure 109: Prototype B, deployed.

Figure 110: Telescopic vertical bracing rod. Expanded (left) and contracted (right)

Figure 111: Scissor unit with end-lugs. Disassembled (left) and assembled (right).

Figure 112: Bracing node prototype. Contracted (left) and deployed (right).

Figure 113: Node and hinge joints in the FE model (left) and in the detailed 3d model (right).

Figure 114: Assembly sequence using uniform node connector with variable axes.

Figure 115: Horizontal section through node connector A, with standard 90° axis orientation.

Figure 116: Horizontal section through node connector A, showing maximum rotation range.

Figure 117: Isometric view of horizontal section through node connector, design proposal A.

Figure 118: Isometric view of assembled node connector, design proposal A.

Figure 119: Exploded isometric view of node connector, design proposal A.

Figure 120: Node connector A. Assembly of a 3d printed, prototype.

Figure 121: Node connector A, 3d printed prototype, interior parts and fully assembled component.

Figure 122: Section drawing through vertical bracing rods containing a linear drive system.

Figure 123: Horizontal section through node connector B, with standard 90° axis orientation.

Figure 124: Horizontal section through node connector B, showing maximum rotation range.

Figure 125: Isometric view of horizontal section through node connector, design proposal B.

Figure 126: Isometric view of assembled node connector, design proposal B.

Figure 127: Exploded isometric view of node connector, design proposal B.

Figure 128: Sectional view. Upper and lower layer node connectors at one of the support points.

Figure 129: Section drawing through vertical bracing rods containing a telescopic linear actuator.

Figure 130: Detailed 3d model "Cross-vault 14-11", with membrane cover (left) and without (right)

Figure 131: Detailed 3d model "Cross-vault 14-11", perspective view.

Figure 132: Visualization "Cross-vault 14-11".

Figure 133: Visualization "Cross-vault 14-11".

9. TABLES

Table 1: Evaluation of double-layer scissor grids as in Hanaor&Levy 2001.

Table 2: Model specifications - 3v geodesic dome.

Table 3: Model specifications - uniform rhomboid spherical dome.

Table 4: Model specifications - tangent circles spherical dome I.

Table 5: Model specifications - tangent circles spherical dome II.

Table 6: Model specifications - translational grid with double curvature.

Table 7: Model specifications - translational grid with double curvature.

Table 8: Model specifications - cyclic quad cross-vault.

Table 9: Model specifications for "Cross-vault 20-12".

Table 10: Cross-section table for "Cross-vault 20-12". Initial model and optimization results, affected values are highlighted in bold letters.

Table 11: Weight, utilization and displacement values for "Cross-vault 20-12". Results for the initial and the optimized model and both load cases.

Table 12: Evaluation of the deployment simulation for "Cross-vault 20-12".

Table 13: Model specifications for "Cross-vault 14-11".

Table 14: Cross-section table for "Cross-vault 14-11". Initial model and optimization results, affected values are highlighted in bold letters.

Table 15: Weight, utilization and displacement values for "Cross-vault 14-11". Results for the initial and the optimized model and both load cases.

Table 16: Evaluation of the deployment simulation for "Cross-vault 14-11".

Table 17: Model specifications for "Barrel-vault 12-10".

Table 18: Cross-section table for "Barrel-vault 12-10". Initial model and optimization results, affected values are highlighted in bold letters.

Table 19: Weight, utilization and displacement values for "Barrel-vault 12-10". Results for the initial and the optimized model and both load cases.

Table 20: Evaluation of the deployment simulation for "Barrel-vault 12-10".

Table 21: Comparison of analysis, optimization and simulation results for all three case studies.